Ove Paulsen

Rigid bonded glass ceramic seals for high temperature membrane reactors and solid oxide fuel cells

Thesis for the degree of Philosophiae Doctor

Trondheim, May 2009

Norwegian University of Science and Technology
Faculty of Natural Sciences and Technology
Department of Materials Science and Engineering

NTNU
Norwegian University of
Science and Technology

NTNU
Norwegian University of Science and Technology

Thesis for the degree of Philosophiae Doctor

Faculty of Natural Sciences and Technology
Department of Materials Science and Engineering

ISBN 978-82-471-1548-0 (printed ver.)
ISBN 978-82-471-1549-7 (electronic ver.)
ISSN 1503-8181

Doctoral theses at NTNU, 2009:85

Printed by NTNU-trykk

Preface

First of all I will express my gratitude to my Researh Director Rune Bredesen who gave me this opportunity as a senior scientist to carry out a PhD in the area of glass science and for being a co-supervisor. The Research Council of Norway shall be acknowledged for funding the PhD as part of the project BigCO2. I am also grateful to my supervisor Professor Tor Grande at Department of Materials Science and Engineering - Inorganic chemistry at NTNU, for his patience and excellent guidance through a complex field of science. His comprehensive knowledge in general ceramics, glass, functional ceramics, thermodynamics and his publishing experience have been to great help to sort out the important from the less important. A thank also to my second co-supervisor Professor Mari-Ann Einarsrud for valuable feedback on my PhD thesis.

.

I will also express my gratitude to the engineer staff at the Department of Materials Science and Engineering at NTNU and to my colleagues at SINTEF for their positive attitude and their helpfulness. I will especially thank the following persons for their assistance:

-Eli Beate Jacobsen for performing the DSC- measurements
-Gunn Torill Wikdahl for assistance with laboratory equipment
-Elin Nilsen and Wilhelm Dall for assistance with the XRD -equipment.
-Julian Tolchard for interesting discussions and help to evaluate crystal structures.
-Hilde Lea Lein for assistance with the flux measurements
-Arild Monsøy for making all the polished sections
-Morten Raanes for excellent Electron Microprobe analysis.
-Jannicke Kvello at SINTEF for performing density and particle size measurements.

Finally I will thank my wife Elisabeth and my daughters Marianne and Julie for being patient and understanding for all the evenings, weekends and vacations when I was working and not taking place in the family activities.

Trondheim January 25, 2009

Ove Paulsen

Table of contents

1 Summary

Solid Oxide Fuel cells (SOFC) and dense gas separation membranes based on mixed ionic and electronic conductors have gained increased interest the resent years due the search for new technologies for clean energy generation. These technologies can be utilized to produce electricity from fossil fuel with low CO_2 emission compared to conventional gas or coal based energy plants. One crucial challenge with high temperature membrane reactors and SOFCs is the sealing of the active membranes/electrolytes to prevent leakage of air to fuel side or vice versa. Due to the high operating temperatures of typical 800-1000 °C the selection of reliable sealing materials is limited. The seals have to remain gas tight during the life time of the reactor/SOFC, they need to be chemical compatible with the sealed materials and stable in reducing and oxidizing atmospheres containing water vapour and CO_2, and finally they should be cheap, readily available and easy to process.

The main purpose of the present work was to evaluate rigid bonded glass ceramic seals for dense oxygen ion and proton conducting membranes and electrolytes for SOFCs and high temperature (HT) membrane reactors. First, a review of sealing technologies has been carried out with emphasis on SOFC and ceramic membranes technologies applicable for zero emission power plants. Regarding sealing, the best and cheapest materials at the present time are based on silicate glass and glass ceramics. In the present work aluminate glass without silica is introduced as a new class of seals expanding the material selection for HT membrane sealing technologies. The main reason for studying silica free systems is that silica is known to be unstable in humid atmospheres and/or reducing conditions at elevated temperatures.

Two glass systems have been evaluated. The first was based on aluminate glasses in the system RO-CaO-Al_2O_3 (R=Mg, Ba, Sr) with special focus on the CaO-MgO-Al_2O_3 denoted CAMn where (MgO+CaO) = 63.7 mol % and Al_2O_3 = 37.3 mol %, n reflects the amount of MgO substituted for CaO). The second was a glass from the BaO-La_2O_3-SiO_2 system denoted BLS. Fabrication and characterisation of the glasses are reported with special focus on the thermal properties, glass forming ability and crystallization region. The evaluation showed that the aluminate glass with 8-10 molar % MgO was a candidate for sealing $LaNbO_4$ based SOFC, while the BLS glass was suited for sealing La_2NiO_4 membranes. The two seal concepts were investigated with focus on the reactions between seal and membrane. The secondary phases formed at the reaction interface between seal and the sealed materials in the respective systems, have been identified and the reaction mechanisms have been elucidated (the notation “secondary phases”

will be used for phases that are formed in the reaction between the seal glass and the sealed materials). The results showed that both seal materials had promising sealing capability developing good physical and chemical contact with the membrane materials and good match regarding thermal expansion. With respect to the BLS/La_2NiO_4 system a previously not reported silicate phase ($Ba_2La_2Si_4O_{13}$) was observed. Another phase of special interest was an apatite phase with composition $Ba_xLa_{10-x}Si_6O_{27-x/2}$ where $1 \leq x \leq 2$, which were shown to cause mechanical stress and severe crack formation in the seal due to mismatch in the thermal expansion. The formation of apatite should therefore be controlled and minimised when BLS is used as a seal for La_2NiO_4.

Leakage tests of seal/membrane/support assemblies at elevated temperatures have been performed demonstrating that both seal concepts are promising. Further optimization of the sealing procedure and possibly alternative fabrication processes of the seal would however improve the seal performance in both cases.

Residual stresses in the seal and membrane for the two systems have been modelled, using an approach suitable for planar membrane systems and for the support/seal/membrane assemblies used for leakage test in the present study. The estimations showed good agreement with observed fractures in the seal microstructure and the leakage tests.

Finally, an outline for developing rigid bonded ceramic seals is reported with suggestions for different approaches to improve the seal performance. The present study demonstrates that secondary crystalline phases formed during the sealing procedure may have thermal expansion coefficients significantly different from the original materials resulting in a fractured interface. In order to minimize the extent of these “unwanted” phases it is discussed that the seal may also be fabricated from fine crystalline materials rather than glasses. By starting with a ceramic seal material the whole glass making procedure can be avoided resulting in a more simple process and a better seal.

2 Introduction

The increasing demands world wide for clean energy supply without greenhouse gas emissions have set focus on fuel cell technologies and oxygen transport membrane reactors (OTMR). Fuel cells are electrochemical devices that can convert chemical energy from different fuels (hydrogen, methane, propane, CO etc.), directly into electrical energy. Fuel cells are attractive due to high efficiency, low emissions, zero noise and their modular and distributed nature. There are many types of fuel cells that have been developed such as alkaline fuel cells (AFC), phosphoric acid fuel cells (PAFC), polymer electrolyte fuel cells (PEM), molten carbonate fuel cells (MCFC) and Solid oxide fuel cells (SOFC) [1-8]. In this work the focus is set on the SOFCs since these are the most promising for converting fossil fuel to electricity in an environmental friendly way [3].

High temperature membrane reactors can be used to separate oxygen or hydrogen from gas mixtures. These membranes are usually mixed ionic and electronic conductors (MIEC). Oxygen transport membranes (OTM) can be used to separate oxygen directly from air for use in combustion of fossil fuels (gas, oil, coal etc) in so called "oxyfuel" combustion [9]. In a similar manner hydrogen transport membranes (HTM) can be used to separate hydrogen directly from natural gas by use of e.g. steam reforming. Hydrogen is a clean energy carrier that can be used in PEM fuel cells or other fuel cells for direct electrical energy generation or used in combustion with air to make heat and steam for further processing to electricity and direct heating. Common for the membrane reactors based on MIECs is that they are operating at high temperatures – typically 800-1000 ˚C, while SOFC operates in the ranges 500-800 ˚C for low and intermittent temperature fuel cells (IT-SOFCs), and 800-1000 ˚C for high temperature solid oxide fuel cells (HT-SOFCs.) [3, 4, 5, 6, 7, 13]

2.1 SOFC and solid oxide gas membrane reactors

A Solid Oxide Fuel Cell (SOFC) consists of a dense metal oxide ceramic ion conducting electrolyte placed between a porous anode or "fuel electrode" and a porous cathode or air electrode. Together, these three components are often denoted as the membrane electrode assembly (MEA) [2]. The electrolyte should be a good ionic conductor and have no electronic conductivity, while the electrodes should be good electronic conductors and possibly also being ionic conductors. Depending on if the electrolyte is being a pure oxygen ion conductor or a proton conductor, two types of SOFC can be considered. For the oxygen ion conducting electrolyte the fuel (in this case H_2) is brought into the anode compartment and the oxidant (air) into the cathode compartment as shown in Figure 2.1. The membrane prevents direct contact between oxygen and hydrogen. At the cathode

oxygen gas is electrochemically reduced to O^{2-}, which migrates through the membrane to the anode. At the anode, hydrogen is oxidized in the reaction with oxygen to produce water and heat: $H_2 + O^{2-} = H_2O + 2e$. In the process two electrons are released to the outer circuit giving electrical power. If the fuel gas had been methane the overall reaction at the anode would be: $CH_4 + 4O^{2-} = CO_2 + 2H_2O + 8e^-$ and at the cathode: $2O_2 + 8e^- = 4O^{2-}$, resulting in the total reaction; $CH_4 + 2O_2 = CO_2 + 2H_2O$.

For a pure proton conducting solid oxide electrolyte, often denoted PCFC (proton conducting fuel cell) the process is analogue to the SOFC as shown in Figure 2.2. Here hydrogen gas is being oxidized at the anode releasing 2 electrons to the outer circuit. Hydrogen ions migrate through the membrane to the cathode where they react with oxygen producing water.

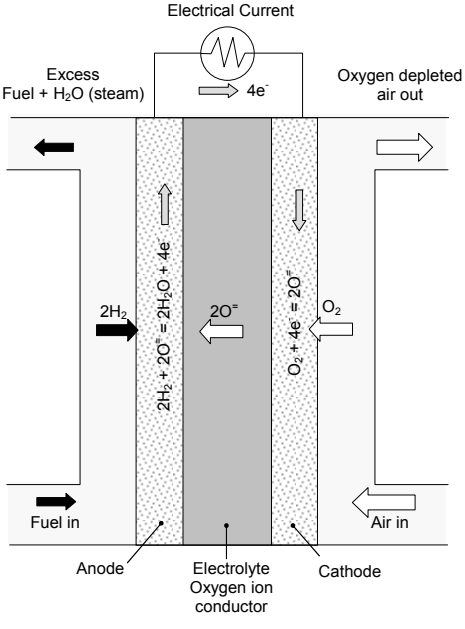

Figure 2.1
SOFC based on oxygen ion conducting electrolyte and hydrogen fuel

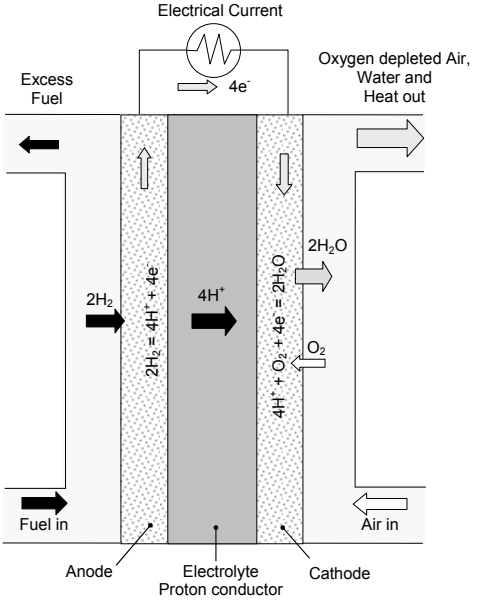

Figure 2.2
PCFC based on solid oxide proton conducting electrolyte and hydrogen fuel

MIEC in form of OTM and HTM can be utilized in numerous ways [9, 14, 15] in power plants and other applications. One example of a complex application where both OTM and HTM reactors are combined in the same unit is shown in Figure 2.3 [14]. In the upper part an OTM is used to remove the oxygen from air flowing trough the central cannel. The oxygen is transported through the OTM where it is used for partial oxidation of

methane flowing in the outer chamber ($CH_4 + O_2 = CO + H_2O + H_2$). In this first stage the methane is transformed into; CO (g), H_2O (g) and H_2 (g). The nitrogen that is left after the oxygen has been removed from the air acts as a sweep gas in the next stage where the HTM removes hydrogen from the flue gas mixture in the outer chamber and transports it to the nitrogen flow. The $N_2 + H_2$ gas mixture can be used as fuel either in a fuel cell or gas turbine. The gas leaving the outer chamber is wet CO_2 that can be dried and compressed for sequestration.

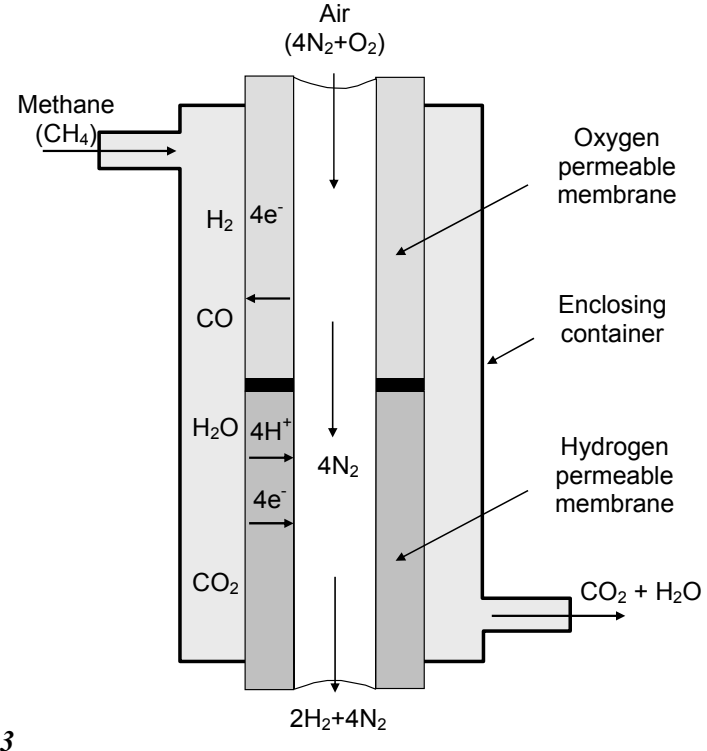

Figure 2.3
Combination of OTM- and HTM-reactors based on mixed ionic/electronic conductors, for production of N_2+H_2 fuel gas mixture from methane and air. The N_2+H_2 mixture flowing in the inner channel can be used in fuel cells or gas turbines. The methane flowing in the outer chamber is transformed to wet CO_2 which can be dried and compressed for sequestration [14]

Another technology that utilizes OTMs is the AZEP (Advanced Zero Emission Process) concept introduced by Hydro [9]. In AZEP a mixed oxygen ion/electron conducting membrane is integrated in a power plant with CO_2 capture using natural gas as fuel. A flow sheet of this process is shown in Figure 2.4. The combustion should be stoichiometric, giving only CO_2 and H_2O as the combustion products. Heat from the combustion is used to heat the pressurized air. Reference [9] gives an excellent overview on the state of the art of the possibilities for use of ceramic membranes in energy production based on fossil fuels with CO_2-capture.

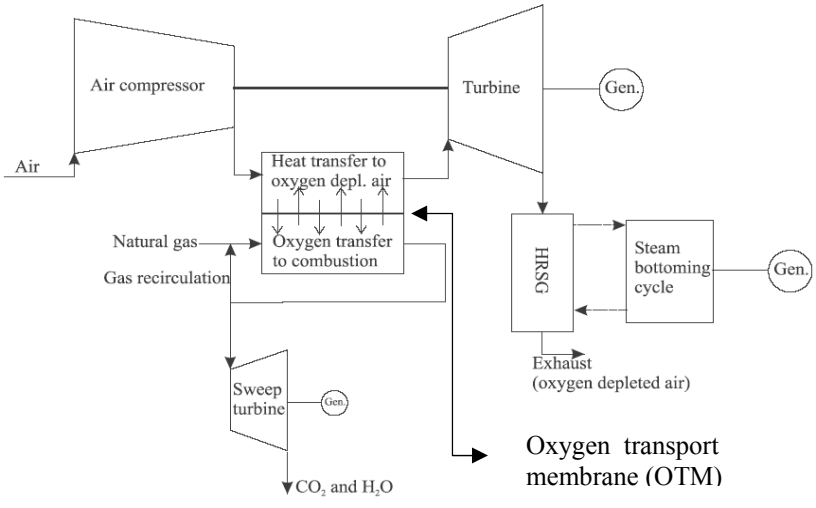

Figure 2.4 *Simplified sketch of the AZEP concept [9]. HRSG: Heat recovery steam generator*

2.2 Materials for SOFC /PCFC and membrane reactors

The high operating temperature of ceramic fuel cells at around 800-1000 ˚C combined with the multi-component nature and expected life time of at least 5 years severely restricts the choice of materials for cell components. All components need to be chemically stable on their own but at the same time also be chemically compatible with the components they are in close contact with. The demands for chemical stability depend on the application. SOFC electrolytes have to be stable both under reducing and oxidizing conditions, anodes must be stable in reducing environment and cathodes in oxidizing environment. In other applications the conditions might be oxidizing or reducing on both sides of the membrane. Moreover, all parts of the fuel cell should have comparable thermal expansion coefficients from room temperature up to the maximum operating temperature, and have reasonable mechanical strength.

High oxygen ion conductivity is found in several classes of structural phases such as; fluorites (AB_2) and related types e.g. pyrochlores ($A_2B_2O_7$), perovskites (ABO_3) and related types (e.g. Ruddlesden-Popper phases $AO(ABO_3)_n$ and Brownmillerite structure $A_2B_2O_5$) and Aurivillius type materials e.g. $Bi_2O_2(A_{n-1}B_nO_x)$ [9].

Perovskites with large metal ions and more open oxygen lattices may have high proton mobility. Acceptor doping can be used to increase the proton concentration and conductivity [9]. Mixed conductors (ionic and electronic)

with high conductivity can be made as composites of highly ionic- and electronic conductive materials. Few single phase materials with simultaneously high electronic and protonic conductivity exist.

2.2.1 Membranes

There are several different membrane materials available for HT-gas separation such as Pd-membranes for hydrogen separation, microporous silica membranes, zeolittes etc. [9]. In the present work the focus will be on dense oxide membranes with mixed ionic and electronic conductivity (MIEC) for oxygen and hydrogen separation. These types of membranes have 100 % selectivity for the specific gases O_2 or H_2 and need no external circuits for electron transport. Accordingly there is no need for electrodes, but usually there is need for a catalyst on one or both sides of the membrane to enhance the reduction/oxidation reactions. Most technological applications of such membranes require current densities approaching 1 $A \cdot cm^{-2}$ corresponding to a flux of 3.8 cm^3 O_2 $cm^{-2}min^{-1}$ at normal conditions [16]. Such high fluxes can only be achieved at high temperatures, typically 800-1000˚C. The driving force for the gas transport is partial pressure gradients across the membrane. If the main gas transport is determined by the bulk (thick membranes) the gas flux (J) is described by the Wagner relation as shown in eq. 2.1 for oxygen flux Jo_2.

$$Jo_2 = \frac{RT\sigma_e\sigma_i}{16F^2(\sigma_e+\sigma_i)L}\ln\left(\frac{p_{O2h}}{p_{O2l}}\right) \qquad 2.1$$

Here R is the gas constant, σ_e and σ_i the electronic and ionic conductivity respectively, F the Faradays constant, L the membrane thickness, P_h the oxygen pressure on the high pressure side and P_l the oxygen pressure on the low pressure side [17, 18]. For proton conducting membranes the flux is given as:

$$J_{H2} = \frac{RT\sigma_e\sigma_i}{4F^2(\sigma_e+\sigma_i)L}\ln\left(\frac{p_{H2h}}{p_{H2l}}\right) \qquad 2.2$$

By plotting oxygen flux (eq. 2.1) against 1/L at constant pressure ratio and temperature the result is a straight line with slope A given as:

$$A = \frac{RT\sigma_e\sigma_i}{16F^2(\sigma_e+\sigma_i)}\ln\left(\frac{p_{O2h}}{p_{O2l}}\right) \qquad 2.3$$

For perovskites, the electronic conductivity is in most cases much higher than the ionic conductivity. In this case the slope expression can be reduced to:

$$A = \frac{RT}{16F^2} \ln\left(\frac{p_{O2h}}{p_{O2l}}\right)\sigma_i \qquad 2.4$$

From this equation the ionic conductivity σ_i can be easily determined. It can be seen from eq. 2.1 that the flux is proportional to the temperature and to the logarithm of the pressure ratio across the membrane, and inverse proportional to the membrane thickness. In order to obtain high flux the membrane should be thin (5-20 μm), and the temperature high. For pressurized systems the high pressure is typically 20-30 bars. Thin membranes in pressurized systems have too low intrinsic mechanical strength and have to be supported by a thicker and porous substrate. The porous support is usually made of the same material as the membrane in order to avoid thermal expansion mismatch.

It is beyond the scope of the present work to give a detailed review of all potential candidates for HT-MIECs, which are given in [9, 19, 20]. However some of the most promising materials will be briefly mentioned.

Among mixed oxygen-ion/electron conductors a series of mixed perovskites with the general composition; $La_{1-x}Sr_xCo_{1-y}Fe_yO_{3-\delta}$ (LSCF) are known for having high oxygen ion and electronic conductivity. Especially the compound $La_{0.6}Sr_{0.4}Fe_{0.2}Co_{0.8}O_{3-\delta}$ (LSCF-6482) has an ionic conductivity of 15 Scm^{-1} and electronic conductivity of 600 Scm^{-1} at 800 °C [21]. The thermal expansion coefficient (TEC) is high for these compounds and dependent on the Co content. The compound LSCF-6482 (rombohedral structure) has the highest TEC; $20.7 \cdot 10^{-6} °C^{-1}$ (20-900 ˚C) [22, 23]. These compounds also possess chemical expansion (chemical expansion is dimensional changes caused by changes in oxygen content in the crystal structure. The material expands with decreasing oxygen content.). Chemical expansion may cause bending of the membrane when the partial pressure of oxygen is different on the two sides.

Another interesting membrane material is La_2NiO_4, which has the Ruddlesden-Popper structure [24, 25, 26]. La_2NiO_4 has a high oxygen transport capacity, a thermal expansion coefficient of $12.4 \cdot 10^{-6} °C^{-1}$ (20-1000 °C) [present work] and contrary to the LSCF-materials it shows almost no chemical expansion. This renders La_2NiO_4 as a good candidate as OTM in e.g. the AZEP-concept. Unfortunately La_2NiO_4 decomposes to La_2O_3 and Ni in reducing atmosphere [27]. La_2NiO_4 is therefore best suited as an oxygen transport membrane in systems with oxidising atmosphere on both

sides of the membrane. An alternative material that is more stable is the perovskite series $CaTi_{1-x}Fe_xCO_{3-\delta}$. The compositions with x=0.1-0.2 have relatively high electronic and ionic conductivity and a linear thermal expansion with $TEC_{(25\text{-}1000^\circ C)}$ of $13.0 \cdot 10^{-6}$ $^\circ C^{-1}$ [present work, Appendix 1]. The material is stable in both oxidising and reducing atmosphere as well as in CO_2 [28, 29].

Numerous cerate and zirconate perovskite oxides (e.g. $SrCeO_3$, $BaCeO_3$, $CaZrO_3$ or $SrZrO_3$) have been reported to have reasonable proton conductivity at high temperatures when doped with a trivalent rare earth ion. Their general formula is $AB_{1-x}M_xO_{3-\delta}$ where M is typically; Nd, Gd, Y, Yb and La [30]. $BaCeO_3$ and $SrCeO_3$ are proton conductors in atmospheres containing H_2 or water vapour. The electronic conductivity may typically be relatively low, but can be increased by doping with aliovalent ions on the B-site. $SrCe_{0.95}Tb_{0.05}O_{3-\delta}$ has been reported to have proton conductivity of 0.005 Scm^{-1} at 800 $^\circ C$ and 0.018 Scm^{-1} at 1000 $^\circ C$ [30]. The flux needs however to be increased by a factor 10 in order to be applied in commercial systems. One disadvantage with the cerates is their low chemical stability in CO_2 containing atmospheres due to formation of carbonates. On the other hand, zirconates are more stable in CO_2 containing atmospheres however they have low proton conductivity and require high sintering temperatures. A possible solution is to prepare mixed solutions of $BaCeO_3$ and $BaZrO_3$. Even better is to introduce a pentavalent ion in the structure as in $Ba_3CaNb_2O_9$, but the unstability of Ba oxides in CO_2 and H_2 is a drawback for practical operations.

One promising candidate as dense mixed proton/electron conductor is a cermet with Y-substituted $BaCeO_3$ as the proton conducting phase [9, 31]. It should be noted that the mixed conductors do not need electrodes. This means that the membrane reactors are less complex than solid oxide fuel cells. So far no mixed proton/electron conducting membrane with sufficient proton conductivity for commercial use has been identified [14].

2.2.2 Electrolytes

From a material point of view the electrolyte is one of the most demanding components in a SOFC or membrane reactor. The electrolyte has to be stable in both oxidising (P_{O2}>0.2 bar at the anode) and reducing conditions ($P_{O2}<10^{-19}$ bar at the cathode) [8]. The oldest and still most used electrolyte for oxygen ion conduction is ZrO_2 stabilized with 8 mol % Y_2O_3 (YSZ). The operating temperature is typically 800-1000 $^\circ C$. Ceria with 10-20 mol % Gd, (CGO) offers excellent promise as a potential electrolyte for lower temperature SOFC (500-600 $^\circ C$). However, unfortunately in reducing atmosphere, such as at the anode, ceria becomes an electronic conductor,

which significantly reduces the efficiency of the SOFC. Extended research is going on to solve this problem [2, 4].

Recently proton conductors based on $LaNbO_4$ doped with Ca, Ba or Sr have been reported. The state-of-the-art proton conductors e.g. $BaZrO_3$ and $SrCeO_3$ have far better proton conductivity than $LaNbO_4$, but are not stable in CO_2-containing atmospheres and render them useless in contact with a proton source like CH_4 [8].

2.2.3 Anode materials

Since the atmosphere is reducing at the anode side, metallic anodes can be used. The most common anode material for SOFCs is nickel/YSZ cermet with 40-50 % nickel evenly distributed in a porous YSZ matrix. Other anode materials are perovskites (ABO_3) of the type $LaCrO_3$ doped with Ca, Sr, or Ti, e.g. $Sr_{0.6}Ti_{0.2}Nb_{0.8}O_3$ and $SrTiO_3$ doped with niobium or lanthanum e.g. $Sr_{0.6}Ti_{0.2}Nb_{0.8}O_3$ and $La_{0.4}Sr_{0.6}TiO_3$ [3, 4, 12]

2.2.4 Cathode materials

The cathode material has to be stable in oxidizing atmosphere and possess high electronic conductivity. Noble metals could be used but are excluded due to high cost. Ceramics with the perovskite structure possessing high electronic conductivity have so far been the number one choice for cathodes. The most used cathode material is lanthanum manganite doped with strontium $La_{1-x}Sr_xMnO_3$ (LSM). Also other ceramic electrolytes have been investigated such as; lanthanum cobaltite, $LaCoO_3$ (LC), LC doped with Sr and Fe e.g. $La_{1-x}Sr_xCo_{1-y}Fe_yO_3$ (LSCF), lanthanum calcium cobaltite ferrite (LCCF), samarium strontium cobaltite (SSC) and others [2, 3, 4, 14]. The cathode is often made of two layers, one consisting of a porous mix of the electrode and the electrolyte (e.g. LSM/YSZ) and the other pure electrode material (e.g. LSM). This two-layer cathode gives a better match of the thermal expansion coefficients between electrolyte and cathode and better chemical compatibility without reducing the performance of the cathode.

2.2.5 Interconnects

So far only single cells have been described. To obtain functional fuel cell units the single cells have to be assembled in stacks in order to give enough power for commercial use. This can only be accomplished by interconnects between each cell.

The main purpose of the interconnects, is to provide electrical contact between the anode of one individual cell and the cathode of the neighbouring one in the stack. The interconnect must therefore be a 100 % electronic conductor with high electronic conductivity and the thermal expansion must be comparable to the membrane electrode assemblies. The interconnects also have to separate the fuel side of one cell from the oxidant side of the next. This implies that interconnects have to be stable under both oxidizing and strongly reducing conditions. The most common interconnects for zirconia based SOFC are the perovskite $LaCrO_3$ doped with divalent cations, e.g. $La_{1-x}M_xCrO_3$ (M= Mg, Ca, Sr) [4,8,33]. Unfortunately most of these compounds show chemical expansion at $P_{O2}<10^{-10}$ bar, which might cause warping and mechanical stress in the SOFC assembly. Interconnects based on steel alloys containing chromium have also been developed for use in SOFCs [10, 11], such as Crofer22APU (Thyssen Krupp VDM, Germany) and $Cr5Fe1Y_2O_3$ (Plansee, Reutte, Austria [15]). One problem with chromium containing materials is formation of volatile CrO_2 (g) and CrO_3 (g) in dry atmosphere. In humid atmosphere $CrO_2(OH)_2$ (g) is the dominating volatile chromium compound. The volatile chromium species cause severe reduction of the electrochemical performance of the cell in relative short time and reduce the protective Cr_2O_3 scale at the interconnect surface [34, 153, 154].

2.2.6 Cell design

There are two main designs of membrane gas separation units and fuel cells; the planar (pSOFC) and the tubular (tSOFC) designs. In the planar design the electrolyte with anode and cathode is typically square shaped with dimensions 100x100 mm^2 to 300x300 mm^2. To obtain high efficiency the membrane assemblies are stacked with metallic or ceramic interconnects between as shown in Figure 2.6. The interconnects have channels for fuel

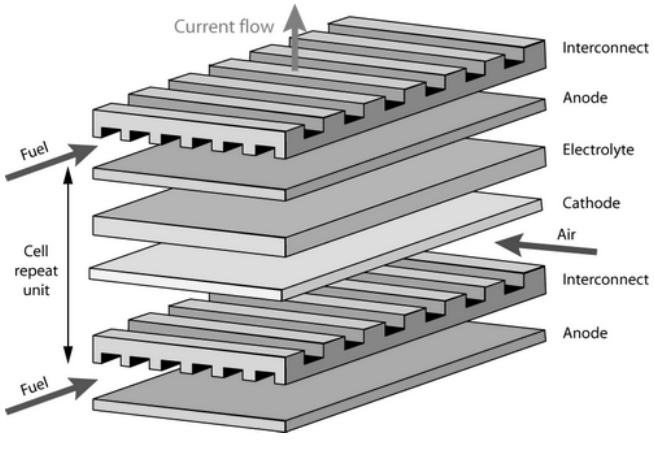

Figure 2.6 *Planar SOFC stack design [33]*

gas and air usually in cross flow enabling manifolds for air on two opposite sides and for fuel on the two other sides of the stack. The most common tubular design introduced by Siemens [18] is shown in Figure 2.7. The air flows through the centre and the fuel flows outside the tube. The anode (air electrode) and cathode (fuel electrode) are linked by the interconnect. When cells are stacked they are connected along the interconnect. The most energy efficient design (measured in kW/m^3) is the planar design, but it is more complex and still has a lot of challenges when it comes to commercial use of high temperature SOFC. One of these challenges is the seal that is needed to prevent direct gas exchange between the anode and the cathode compartments of the cells.

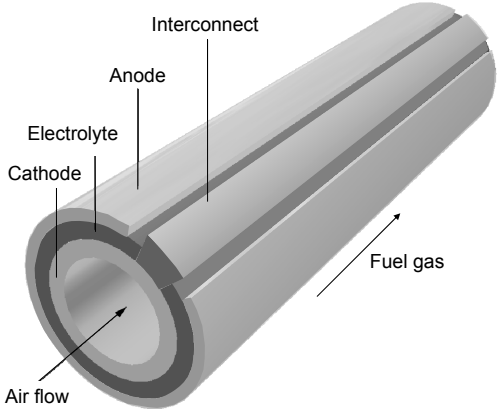

Figure 2.7
Siemens Westinghouse, tubular fuel cell [35]

2.2.7 Sealing

The complexity of sealing of a pSOFC is demonstrated in the typical stack assembly shown schematically in Figure 2.8 [19]. The seal has to match the electrolyte, cathode and interconnect materials with respect to thermal expansion. Depending on the design the seal might have to join ceramic to ceramic, ceramic to metal or metal to metal. For air and fuel supply, the SOFC stacks need manifolds with corresponding sealing as shown in Figure 2.9 [36]. These examples demonstrate the extreme demands that are put on the seals for pSOFCs. Several seal concepts for SOFCs have been developed during the last 20 years but few have been tested for long time (> 2 years) under realistic conditions. Glass and glass ceramic seals have proven to be effective in sealing stacks for short- and moderate-term operation, but questions remain concerning the long-term durability and thermal cycling performance of these seals [37]. Finding solutions for the seal challenges are crucial for large scale use of SOFC technology and high temperature membrane reactors.

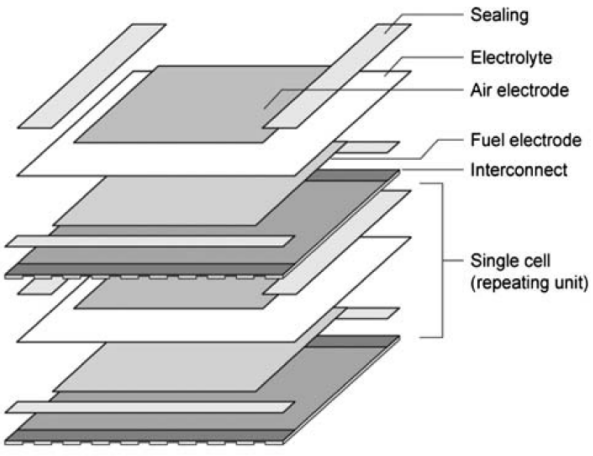

Figure 2.8
Schematic of edge sealing of pSOFC stack [36]

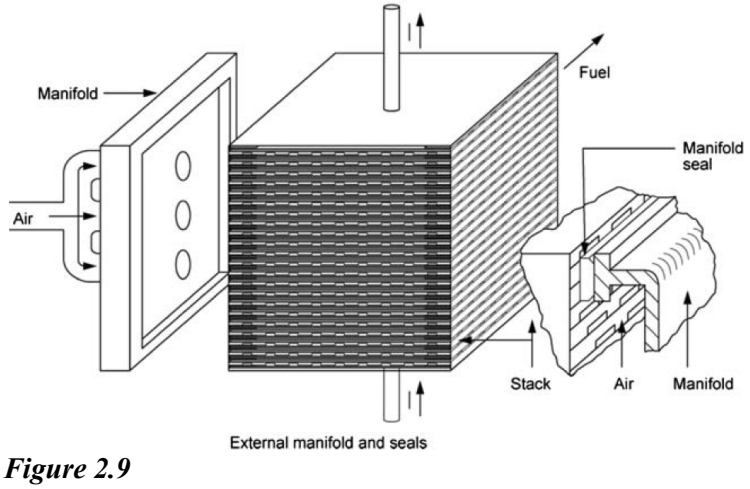

Figure 2.9
Schematic of one possible design for sealing the air supply manifold to a pSOFC stack. A corresponding manifold is needed for the fuel supply [36]

Published glass or glass-ceramic seals for SOFC and other high temperature membrane systems are so far based on different silicate systems [43-80] and a few phosphate glass systems [38, 39]. The main focus has been on making seals with thermal expansion close to the expansion of the interconnects and membrane electrolyte assembly. However recent research has shown that silica may be detrimental to both electrolyte and electrodes over time due to formation of secondary silicate phases, resulting in possible reduced performance of the system [40, 41]. It is well known that silica is not stable in strongly reducing atmosphere due to formation of SiO (g) according to

the reactions: $SiO_2 + CO(g) = SiO(g) + CO_2(g)$ or $SiO_2(s) + H_2(g)=SiO(g) + H_2O(g)$. Due to this, silicate based seals will degrade the anode over time. How fast the degradation will be is not fully known and other glass ceramic systems should be considered.

In humid atmospheres at high temperatures and high pressures, SiO_2 is not stable even under oxidizing conditions. In this case SiO_2 reacts with water to form the gaseous silicate phases $Si(OH)_4$ (g) or $SiO(OH)_2$ (g) [14, 41-44]. Studies of $SrFeO_3$-based electrolytes (oxygen ion conductors) at 1000˚C and 30 bar pressure in humid hydrogen atmosphere [41, 45] showed formation of Sr_2SiO_4 due to reaction with silicon hydroxide transported in the gas phase. The resulting Sr-depletion of the electrolyte led to reduced performance. This can be an important issue for gas separations membrane reactors exposed to high pressure.

It is not sufficient that the seal and membrane are chemical and dimensionally stable in their own and have matching thermal expansion coefficients at the operational conditions. The secondary phases should also have matching thermal expansion and not degrade the membrane or electrodes during operation. Mismatch in thermal expansion between the seal and the sealed materials might cause residual stresses passing the mechanical strength of the interfaces resulting in crack formation and subsequent seal leakage.

2.3 Aim of the present work

The present work addresses possible glass ceramic seals for membrane reactors operating at 800-1000˚C using La_2NiO_4 or $LaNbO_4$ as membrane or electrolyte. One purpose was to evaluate sealing materials without silica with special focus on the alkaline-earth-aluminates in the system CaO-MgO-Al_2O_3 (CAM).

Another aim was to evaluate a silicate glass in the system BaO-La_2O_3-SiO_2 (BLS) [50] for use as seal for membrane reactors with La_2NiO_4. This was included since this kind of membrane reactors are potential candidates for future energy production based on clean fossil fuel combustion. The main tasks can be summarized as follows:

a) Evaluate the glass forming ability of the aluminate glasses versus content of MgO
b) Evaluate the thermophysical properties of the glass compositions
c) Identify the phases in crystallised glasses
d) Evaluate reactions between membrane and seal materials focusing on secondary phases formed in the reactions

e) Evaluate the chemical stability of glasses at elevated temperatures in dry and humid atmospheres containing CO_2
f) Evaluate seal performance with respect to leakage at elevated temperatures

Due to the complexity of the systems most of the work was focused on tasks a-d.

3 Sealing technology

3.1 Seal Concepts

Both high temperature SOFC and high temperature gas separation membrane systems need reliable seals in order to operate. The demand on commercial systems is continuous operation for at least 40 000 h (5 years). The main purpose of the seal is to hermetically separate the fuel side from the air side in order to prevent that fuel gets direct access to the air side. For a SOFC the seal also needs to be an electrical insulator to prevent short circuiting of the stack. Any short circuiting of electrical current or gas leakage between the air side and fuel side will lead to reduced performance of the system. There are three basic seal designs:

1. Rigid bonded seals
    a. Room temperature analogue: Epoxy glue
    b. Materials: Glass, glass ceramic, braze

2. Compliant, bonded seals
    c. Room temperature analogue: Rubber glue
    d. Materials: Metal

3. Compressive seals
    e. Room temperature analogue: Rubber O-ring, gaskets
    f. Materials: Mica based, vermiculite, other ceramic fiber (Al_2O_3, aluminium silicate, silicate)

General for these designs is that the sealing materials must be chemically stable both in highly reducing as well as in oxidizing atmosphere and be chemically compatible with the joining materials such as electrodes, membranes, interconnects and frame material (often heat resistant alloys). The demands differ for the different seal concepts. The seals needed in a typical pSOFC stack where air and fuel supplies are in a cross flow configuration [36] are shown in Figure 3.1. The single cells are all ceramic materials, the interconnect can be either a ceramic or a metallic material, and the housing is based on metal parts with ceramic spacers. In this design there are 4 seal positions:

S1: Cell to metal frame (ceramic to metal seal)
S2: Metal frame to interconnect (metal to metal or metal to ceramic seal)
S3: Ceramic spacer to metal frame and ceramic spacer to interconnect.
S4: Stack to base manifold plate (metal to metal seal)

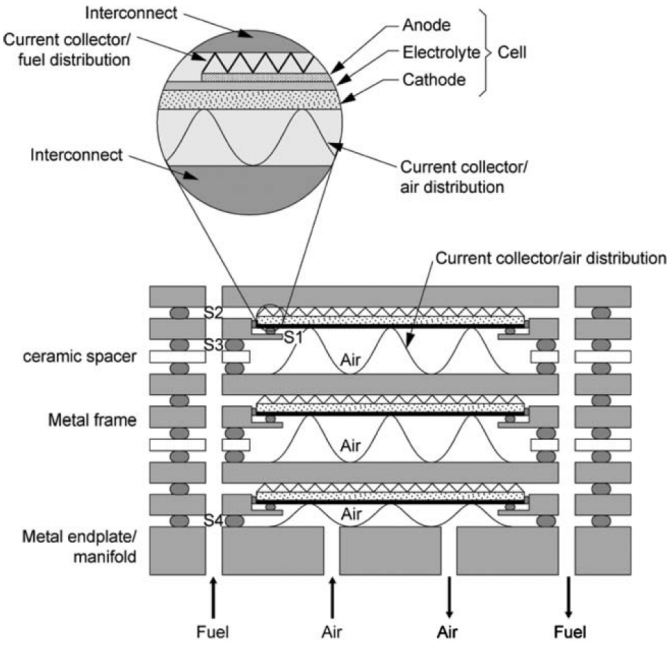

Figure 3.1 *Possible seals for SOFCs [36]*

Another design developed at Jülich, Germany [51] is shown in Figure 3.2. In this case, the interconnecting plates and the cell frames (each housing one electrolyte assembly), are made of the alloy, which is specially developed for YSZ-electrolytes. The seal is placed between the interconnect and cell frame at the anode side and between the cell-frame/electrolyte and

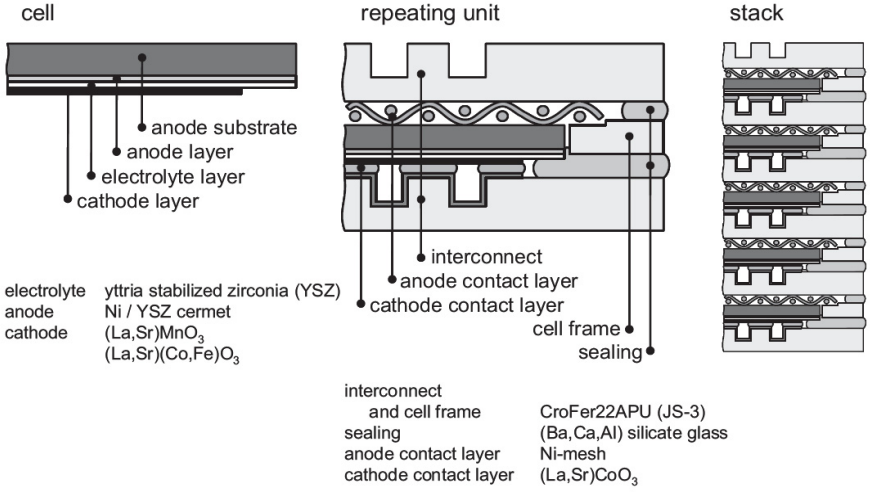

Figure 3.2
Planar SOFC stack developed at Forschungszentrum Jülich Germany [51], showing in detail how the stack is built

interconnect at the cathode side. The seal material thus has to be chemical compatible with the interconnect, cell frame and the membrane/cathode assembly. The complexity of the sealing concepts demonstrated above indicates that the use of different seal compositions in the same SOFC stack can not be excluded.

3.2 Rigid bonded seals

For high temperature purposes seals based on glass or glass-ceramics are the most promising concept due to high chemical stability at high temperature. The glasses in question are cheap, readily available and can be supplied as a paste or paint of powders mixed with a liquid binder. The glass powders can also be tape cast in thin sheets, which can be cut into special shapes to fit the parts to be sealed. The sealing function is achieved by heating the membrane assembly with the "green" seals to a temperature high enough for the seal to sinter completely. A special heating cycle may be needed in order to get the glass to crystallise. The maximum temperature for the sealing cycle should be lower than for all the previous fabrication steps of the cell components and higher than the operational temperature. The seal must wet the components during sealing, but not react in a way that reduces the performance of the seal or the sealed components.

Glass ceramic seals are rigid and brittle and are strongly bonded to the joined parts. To prevent cracking it is vital that the thermal expansion of the seal matches the joined parts to within a few % from room temperature and up to the operating temperature. The ideal seal would be a glass ceramic with a few % glassy phase that is able to deform plastically (highly viscous at operation temperature for the system). Unfortunately all glasses will tend to crystallise when held at high temperature for long time and will in most cases become completely crystalline long before the expected lifetime for the system has run out. One complicating factor is that the crystalline material may consist of several phases. It is therefore of great importance that these phases all have similar thermal expansion. If not, microcracks are likely to arise resulting in reduced seal performance.

3.3 Thermal expansion of SOFC materials

Since thermal expansion is one of the most important parameters to control when developing rigid seals it is necessary to know the range of thermal expansion that has to be considered. Tietz [52] has made an excellent review of thermal expansion of SOFC materials and some of the data from this review are listed in table 3.1-3.3.

Table 3.1
Thermal expansion coefficient of a selected electrolyte- and membrane materials

Short name	Composition	TEC x10^{-6} °C^{-1} (30-1000 °C)	Ref.
8YSZ	$Zr_{0.85}Y_{0.15}O_{1.93}$	10.9	[52]
10YSZ	$Zr_{0.82}Y_{0.18}O_{1.91}$	11	[52]
A	Al_2O_3 (polycrystalline)	8.4	[53]
CGO	$Ce_{0.8}Gd_{0.2}O_{1.9}$	12.7	[52]
CSO	$Ce_{0.9}Sr_{0.1}O_{1.9}$	13.1	[52]
LSGM	$La_xSr_{1-x}Ga_yMg_{1-y}O_{3-\delta}$ (x, y = 0.8-0.9)	10.8-11.4	[52]
LSGMC	$La_{0.9}Sr_{0.1}Ga_{0.75}Mg_{0.2}Co_{0.05}O_{3-\delta}$	13	[52]
LN	La_2NiO_4	12.4	Present work
LNb	$LaNbO_4$	9.6*	Present work
CTF	$CaTi_{0.90}Fe_{0.1}O_{3-\delta}$	12.5	Present work

* Mean value between 30- and 1000°C. $LaNbO_4$ has a phase transition at ~ 530°C, see Figure 5.3

Table 3.2
Thermal expansion coefficient of a selection of SOFC cathode materials

Short name	Composition	TEC x10^{-6} °C^{-1} (30-1000 °C)	Ref.
LSM	$La_xSr_{1-x}MnO_{3-\delta}$ (x = 0.65-0.8)	11.1-12.3	[52]
LCMC	$La_{0.65}Sr_{0.3}Mn_{0.8}Co_{0.2}O_{3-\delta}$	11.7	[52]
PSM	$Pr_{0.8}Sr_{0.2}MnO_{3-\delta}$	10.1	[52]
NSM	$Nd_{0.65}Sr_{0.3}MnO_{3-\delta}$	9.7	[52]
GSM	$Ga_{0.65}Sr_{0.3}MnO_{3-\delta}$	9.9	[52]
GSMC	$Ga_{0.8}Sr_{0.2}Mn_{0.8}Co_{0.2}O_{3-\delta}$	10.2	[52]
LSC	$La_{0.7}Sr_{0.3}CoO_{3-\delta}$	19.2	[52]

Table 3.3
Thermal expansion coefficient of a selection of interconnect materials.

Short name	Composition	TEC x10^{-6} °C^{-1} (30-1000 °C)	Ref
LSC	$La_{0.9}Sr_{0.1}CrO_3$	10.7	[52]
LCCT	$La_{0.7}Ca_{0.3}Cr_{0.5}Ti_{0.5}O_3$	10.1	[52]
LSCT	$La_{0.7}Sr_{0.3}Cr_{0.8}Ti_{0.2}O_3$	10.7	[52]
$CrFe5Y_2O_3$	Fe-Cr alloy	11.3-12.0	[52]
X10CrAl18	Ferritic steel	13.9	[52]
Crofer 22APU	Fe-Cr-alloy	12.7	[54]
253MA	Fe-Cr-Ni alloy	19.5	[55]

TECs for electrolytes and membranes for SOFCs and membrane reactors are in the order of 9-14x10^{-6} $^{\circ}C^{-1}$ (see Tables 3.1-3.3). Thermal expansion of common cathode materials is in the range 9.7-19.2·10^{-6} $^{\circ}C^{-1}$ as shown in Table 3.2. The corresponding thermal expansion coefficients for metallic and ceramic interconnects are in the range 10-19.5·10^{-6} $^{\circ}C^{-1}$ as shown in Table 3.3. This shows that the TEC of glass ceramic seals in most cases, will have to be in the range 9-14·10^{-6} $^{\circ}C^{-1}$ for SOFC purposes.

Before the different seal glass systems proposed for SOFC sealing are reviewed, glass and glass-ceramic properties will be shortly described.

3.4 Glass and glass ceramics

Inorganic glasses consist of one or several *network formers* added one or several *network modifiers* and often also some *intermediates* [56]. Glasses are amorphous solids, but can also be partly or totally crystallised (also denoted *inverted*) to give a glass ceramic. Oxide glasses can be described as a continuous network of atoms linked together by oxygen atoms. Common network formers are; SiO_2, B_2O_3, P_2O_5, GeO_2, TeO_2, SeO_2, As_2O_3, SbO_2 and V_2O_5. Except for SiO_2, ZrO_2, B_2O_3 and P_2O_5 these oxides are reduced by hydrogen at 750 ˚C and can not be used as a SOFC seal [73].

B_2O_3 additions to silicate glass generally decrease the viscosity and the tendency for crystallization, which are favourable properties. Addition of more than 12 mol % B_2O_3 increases the thermal expansion [74]. One disadvantage with the B_2O_3 addition is that boron oxide forms volatile compounds with water vapour at elevated temperatures resulting in seal degradation [73]. The use of B_2O_3 in silicate glasses thus has to be a compromise between the favourable and less favourable properties of B_2O_3. The majority of suggested silicate seal glasses for SOFCs contain B_2O_3 [59-96].

Common network modifiers are alkali and alkaline earth oxides and some other oxides such as ZnO, PbO, Y_2O_3, TiO_2 and La_2O_3. The modifiers affect the chain structure so that physical properties such as viscosity, thermal expansion, density, refractive index, chemical durability, etc. can be tailored. The alkali oxides are common in glasses for use at ambient temperatures, but for glasses that are to be used at high temperatures these oxides are avoided due to their high reactivity and high ionic mobility. The most common modifiers in glasses for high temperature applications are the alkaline earth oxides.

Intermediate oxide candidates are Al_2O_3, Cr_2O_3, TiO_2, ZnO, ZrO_2, HfO_2, Ta_2O_5 and rare earth oxides. Al_2O_3 and ZrO_2 are stable oxides even in strongly reducing atmospheres. TiO_2 is often added as a nucleating agent for the purpose of achieving homogeneous nucleation in the glass. TiO_2 may be reduced in H_2 at 800 ˚C and ZnO is reduced in dry H_2 even at 300 ˚C, but shows no reduction in wet H_2 even at much higher temperatures. Carbon containing fuel gases (e.g. CH_4, CH_3OH) reduce ZnO under both wet and dry conditions. ZnO has similar effect as boron oxide regarding the viscosity and thermal expansion.

Alumina is an important constituent in many glasses. Al_2O_3 increases the viscosity of molten glasses and promotes development of microcrystalline growth, which is an attractive property for glass-ceramic seals. Alumina also increases the chemical durability, hardness and other mechanical properties [58]. On the basis of chemical and physical properties the following 11 oxides are potential components for SOFC seal: SiO_2, B_2O_3, Al_2O_3, BaO, SrO, CaO, MgO, Y_2O_3, ZnO, La_2O_3 and Ta_2O_3 [57].

3.4.1 Glass transition temperature

When a glass melt is cooled from a high temperature, T, to room temperature, T_R, the specific volume of the system will change as shown in Figure 3.3. Depending on the glass system and rate of cooling, the melt can either crystallise (System 1) or solidify to a glass (System 2). As soon as the temperature falls below the crystallization temperature, T_x, the volume of system 1 contracts from A to B and forms a crystalline material. On the other hand System 2, as an undercooled liquid, continues to shrink further to point C; and if the cooling is sufficiently slow even further to point D. Here the curve flattens out towards F. By fast cooling the glass continues to shrink linearly directly from C to E. In both cases it will always remain above the line B-G of the crystalline system.

The temperature T_g where the glass cooling curve flattens out, is called the *glass transition* or *glass transformation temperature*. Actually T_g represents the onset and $T_{g'}$ the end of the glass transition range since T_g is not a unique material property but depends on the cooling rate. Below $T_{g'}$ the glass is considered as a solid material where mechanical stresses can build up. The transition from the viscous state to the elastic state occurs within the viscosity range; $10^{13.5}$ – 10^{12} Pa·s. In this range, which also is denoted the *annealing range*, mechanical stresses that may have developed during cooling below T_g can be eliminated. At 10^{12} Pa·s, 15 minutes are sufficient to accomplish this. At $10^{13.5}$ Pa·s, the elimination of stress may take several hours [97]. The temperature range between T_g and T_x is defined as the *glass stability region* or *glass forming ability*. This temperature range is dependent on the heating rate and accordingly it represents no precise

definition. During heating of a glass, the dilatometric softening point, T_d, or deformation point is reached above T_g as shown in Figure 3.4. At this temperature the force from the dilatometer pushrod will deform the glass. The viscosity at T_d is $10^{10.3}$ Pa·s which is much higher than the viscosity at the softening point T_s ($10^{6.6}$ Pa·s) where the glass deforms under its own

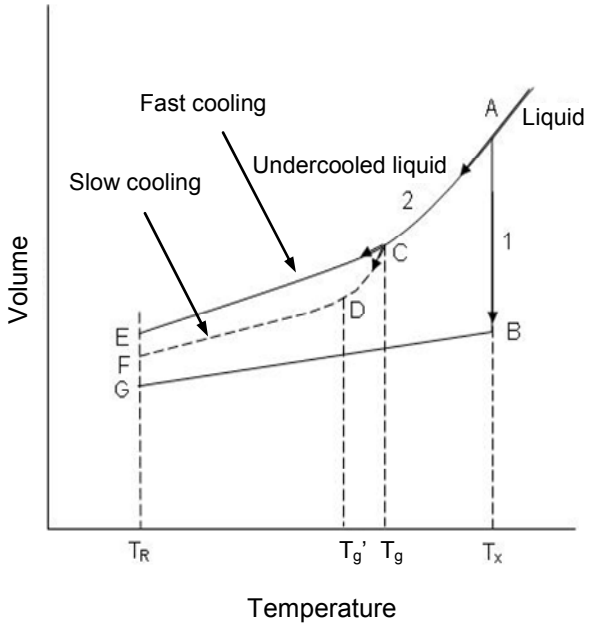

Figure 3.3
Volume changes versus temperature for a glass system (1) and a crystalline system (2). Path CE - fast cooling, CF- slow cooling. Glass transition temperature T_g depends on cooling rate

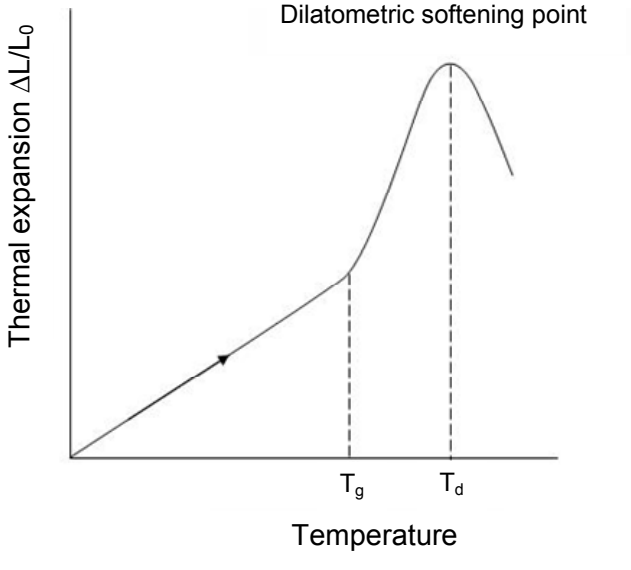

Figure 3.4 *Typical thermal expansion curve of a glassy material*

weight. The glass can be easily shaped at a viscosity about 10^3 Pa·s (working point). To make a homogeneous glass, the glass must be heated to a temperature where the viscosity is below 10 Pa·s [98].

3.5 Temperature dependence of viscosity

Viscosity of a glass decreases with increasing temperature according to a logarithmic law. Arrhenius described the viscosity by equation 3.1. More common is equation 3.2 of Vogel-Fulcher-Tamman (VFT) that is usually expressed in the logarithmic form shown in eq. 3.3.

$$\eta = \eta_0 e^{\Delta H_\eta / RT} \qquad 3.1$$

$$\eta = \eta_0 e^{B/(T-T_0)} \qquad 3.2$$

$$\log \eta = A + \frac{B}{T - T_0} \qquad 3.3$$

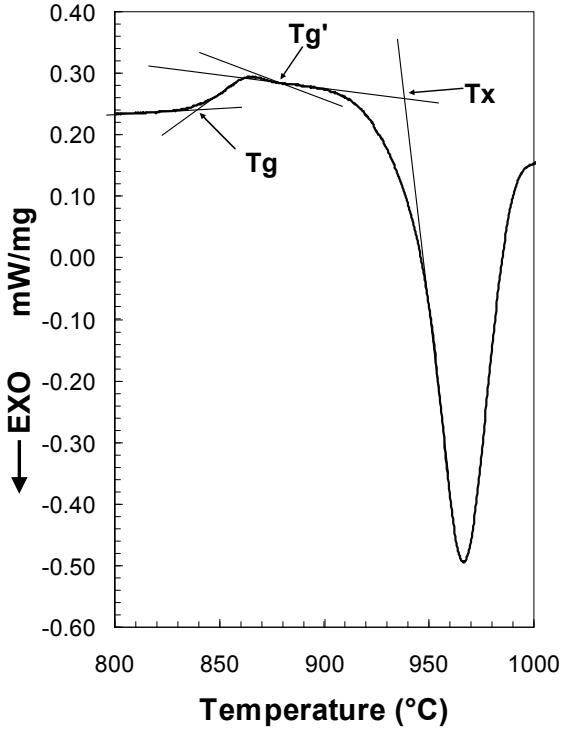

Figure 3.5
DSC pattern of one of the glasses studied in the present work, showing how the glass transition range, T_g-T_g', and the onset temperature of crystallization, T_x, can be determined. Heating rate 10°C/min

The non-linear behaviour of the viscosity in an Arrhenius plot has been used to classify glasses as *strong* and *fragile*. Strong glasses show linear behaviour as expressed by eq. 3.1, while fragile glasses demonstrate no-linear behaviour as described by the VFT-equation, eq. 3.2 [47].

Moynihan et al. [99] have shown that it is possible to calculate the viscosity of a glass as a function of temperature from DSC measurements in the glass transition region. By measuring the temperatures at the start and completion of the glass transition, respectively T_g and $T_{g'}$ as shown in Figure 3.5. Moynihan developed an empirical formula (eq. 3.4 and 3.5) that can be used to calculate the viscosity over a wide temperature range. One example is given in Figure 3.6 showing how the viscosity for the aluminate glass CAM10 (see chapter 4.2) decreases as the temperature increases. Important viscosity ranges for glass making are also shown in the Figure.

$$\log\left(\eta / Pa{\cdot}s\right) = -5 + \frac{14.2}{C\left(T - T_g'\right) + 1} \qquad 3.4$$

$$C = \frac{0.147}{T_g'^2\left(\frac{1}{T_g} - \frac{1}{T_g'}\right)} \qquad 3.5$$

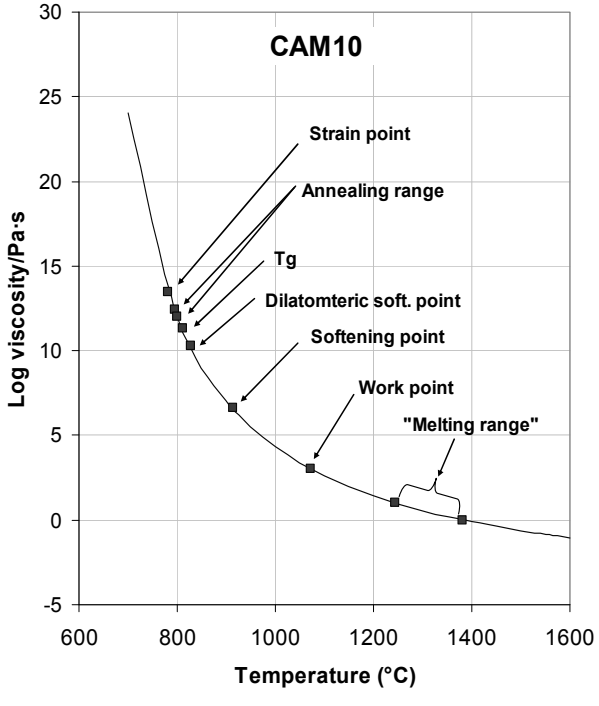

Figure 3.6
Calculated viscosity of the aluminate glass CAM10 as a function of temperature (see chapter 5) by use of equations 3.4 and 3.5. Important temperatures for glass making are shown in the Figure

The viscosity of glass seals should be $\geq 10^9$ Pa·s at the operational temperature [79].

3.5.1 Crystallization

Given enough time at the right temperature all glasses can devitrify and become crystalline. The onset temperature for crystallization, T_x, depends on the glass system but it is always higher than T_g. In order for a glass to crystallise nuclei of critical size r* are needed. The free energy change, ΔG_r, when a region of radius r of a new phase is formed in a glass is given by [56]:

$$\Delta G_r = 4\pi r^2 \gamma + \frac{4}{3}\pi r^3 \Delta G_v \qquad 3.6$$

Here γ is the interface energy and ΔG_v the free-energy change per unit volume for the phase transition. For the new phase to grow, the size of the nuclei has to pass a critical radius *r**. This radius can be calculated by minimizing ΔG_r with respect to r ($\partial \Delta G_r / \partial r = 0$) giving the critical radius r* as:

$$r^* = \frac{-2\gamma}{\Delta G_v} \qquad 3.7$$

Nuclei with r>r* are stable and will grow while nuclei with r<r* is unstable and dissolve. The rate of nucleation is dependent on temperature as shown in Figure 3.7 [101].

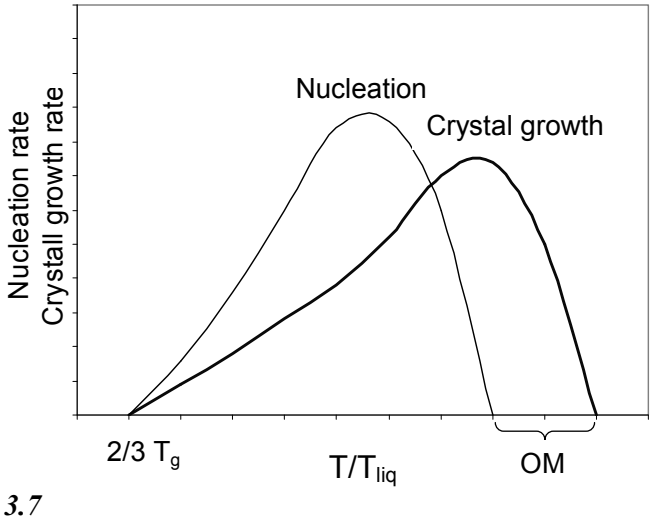

Figure 3.7
Illustration of nucleation rate and crystal growth. T_{liq} is the temperature where crystals dissolve. In the Ostwald-Miers range (OM) there is no nuclei growth [101]

The maximum nucleation rate appears at a viscosity of 10^{10}-10^{11} Pa·s [56], which is close to the dilatometric softening point. By further heating the nucleation rate decreases to zero at a given temperature. The rate of crystal growth (also shown in Figure 3.7), have a maximum at a higher temperature than the nucleation rate. By further heating the crystal growth rate decreases and finally becomes negative at T_{liq}, where the crystals start to dissolve. In the Ostwald-Miers range (OM in figure 3.7) no nuclei are formed. This implies that if a glass melt is cooled from above T_{liq} there will be no crystallization before the temperature has passed the OM-range. The rate of crystallization can be expressed by equation 3.8 [100] where R is the growth rate, C a constant depending on the glass system and T is the temperature.

$$R = \frac{C(T_{liq} - T)}{\eta} \qquad 3.8$$

To form a glass ceramic from a glass, the heating cycle shown in Figure 3.8 is used. Normally a glass powder (frit) that already has been processed at high temperature is the starting material. The frit is heated to a high temperature in order to get rid of gas bubbles (fining). Then the temperature is lowered to the proper temperature for the material to be formed to the final shape. When the forming step is finished, the temperature is lowered to the optimum temperature for nucleation and held there for 10-15 min. When nucleation is finished the temperature is raised to the value for crystal growth. The crystallization temperature and the holding time depend on the intended crystal structure. To obtain a glass-ceramic with high strength the crystals should be numerous and small (<1 μm).

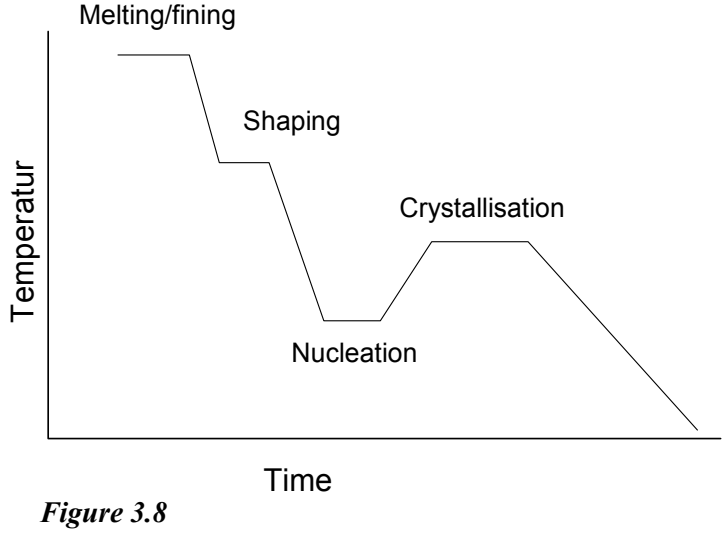

Figure 3.8
Typical heat treatment for crystallization of glass

To achieve a large number of small crystals, the crystallization temperature should be "low". After crystallization the glass is cooled to room temperature. If the glass is reheated to temperatures corresponding to the crystallization temperature the crystals will continue to grow. A glass that is to be used as a high temperature seal must therefore be fully crystalline before it can be regarded as volumetrically stable. This has to be considered when determining the sealing temperature cycle. It is an advantage to have only one crystalline phase, but in reality ceramic seals usually contain several crystalline phases. To avoid microcracking the thermal expansion of the different phases should be similar to within a few %. The ideal seal would be a ceramic material with a few % glassy phase operating at a temperature in the *glass stability region,* just above $T_{g,}$ to avoid complete crystallization [4]. However in this temperature range there is a high nucleating activity. If the temperature is held constant in this range for long time (some days or weeks) the glass will become completely crystalline.

3.6 Seal glasses for SOFC and high temperature membrane reactors

During the last 20 years several seal glass compositions for SOFCs have been proposed and evaluated [56, 57, 59-95]. The main focus has been on tailoring the TEC, $T_{g,,}$ T_s and T_x to the specific design and temperature of operation in order to find glass-ceramic seals that are stable and chemically compatible for long time of operation. The majority of the proposed seal glasses for SOFCs can be divided in two groups; One B_2O_3-containg and one without B_2O_3. Boron-silicate glasses can be used for low to intermittent temperature systems, while those without boron oxide are best suited for high temperature systems.

3.6.1 Boron-silicates

Most of the proposed seal glasses in this group consist of the oxides; B_2O_3, SiO_2, Al_2O_3, BaO, CaO and SrO [59-75, 86, 87, 89]. Boron silicates have excellent seal performance due to high wetting ability and low viscosity during sealing. Glasses in this group might have high chemical stability in both dry and humid H_2 atmosphere [43, 51] at 800 ˚C. These compositions also show good seal performance during thermal cycling between RT and 800 ˚C.

The effect of the different components on the glass properties depends on the overall composition of the glass. Normally B_2O_3 lowers the softening point and T_g, but if the Ba_2O_3/SiO_2 ratio is held constant B_2O_3 additions have little effect on the two temperatures. This was demonstrated by Sohn et al. [63] for the glass (20-40)BaO-10Al_2O_3-5La_2O_3-(12.5-21.7)B_2O_3-(29.2-43.3)SiO_2 where the ratio B_2O_3/SiO_2 was held constant at 0.5. T_g and T_s for

all compositions were in the range 668-671 °C and 735-745 ˚C, respectively. In the system B_2O_3-Al_2O_3-SiO_2-La_2O_3-SrO, Ley et al. [43] were able to make glasses with T_g in the range 560-780˚C.

The thermal expansion can also be tailored within wide ranges for these glasses but the effect of the different oxides differs for the different glass systems. Jinhua et al. [67] evaluated a series of glasses with composition (mol %) 33.3SiO_2-16.7B_2O_3-10Al_2O_3-5La_2O_3-35(CaO+BaO) where CaO was gradually substituted with BaO in the range 0-35 mol %. For this range the TEC varied from $7.6 \cdot 10^{-6}$ °C^{-1} to $13.0 \cdot 10^{-6}$ °C^{-1}. The glass with 35 %CaO had the lowest TEC while the highest was observed for the glass with 35 % BaO as demonstrated in Figure 3.9. This shows that CaO lowers the thermal expansion while BaO increases it. La_2O_3 additions will also have a positive effect on increasing the TEC [63, 75]. SiO_2 and Al_2O_3 have normally a negative impact on the TEC. In a series of boron silicate glasses with constant B_2O_3/SiO_2 ratio of 0.5 the effect of MgO, SrO, Al_2O_3, La_2O_3 and Y_2O_3 on the TEC was investigated [75]. The results showed that Y_2O_3 and SrO increased the TEC, MgO and Al_2O_3 lowered the TEC, while La_2O_3 had little influence.

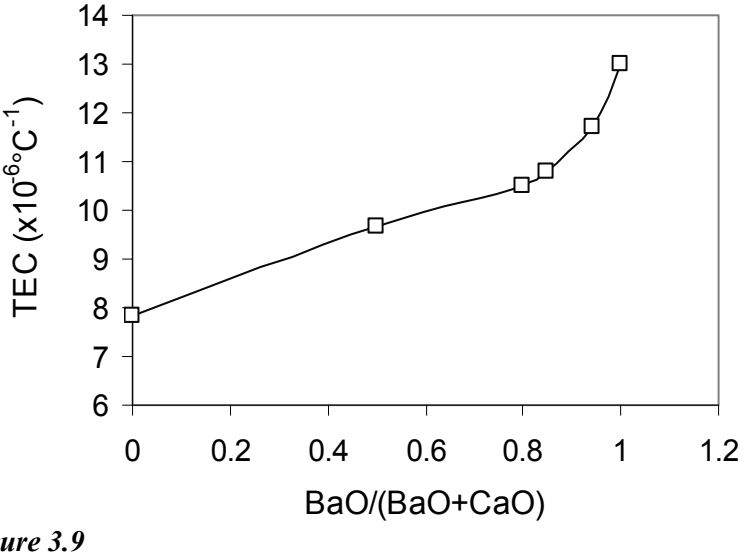

Figure 3.9
Effect of BaO substitution for CaO on thermal expansion of boron-aluminium-lanthanum silicate glass containing 35 mol % (CaO+BaO) [67]

3.6.2 Alumino-silicates

The following alumino-silicate seal glasses; MO-Al_2O_3-SiO_2, (M=Ca, Ba, Mg, Sr and Zn) are reported [76, 78, 79, 80, 85]. By adding up to 75 vol. % MgO filler to a sodium-aluminium-silicate glass (NAS), the TEC increased

linearly from 11.5 to $13.7 \cdot 10^{-6}$ °C^{-1} [78]. 32 vol. % MgO seemed to be the maximum due to reduced mechanical properties for higher MgO contents. The glass/MgO composite seal worked well above 850˚C as seal material for the interconnect alloy Crofer22APU. The sintering and thermo-physical properties of glasses in the system $30BaO\text{-}5Al_2O_3\text{-}50SiO_2\text{-}15RO$ (mol %) where R=Ca, Mg, Ba and Zn have been investigated [79]. T_g varied between 692 and 719˚C with the addition of Zn, Ba, Mg and Ca, respectively. ZnO-addition had the largest effect on lowering T_g compared to the other. The pure barium-aluminium-silicate glass (BAS-glass) with 45 % BaO had a TEC of $13.2 \cdot 10^{-6}$ °C^{-1} while for the other 3 additives the same TEC of $9.7 \pm 0.1 \cdot 10^{-6}$ °C^{-1} was observed. In BAS-glasses thermal expansion can be modified within wide limits by changing the BaO-content as shown in Figure 3.10 [65]. The glass compositions were in the range (mol %) $(33.7\text{-}45)BaO\text{-}(5\text{-}10.5)Al_2O_3\text{-}(50\text{-}57.5)SiO_2$. As Figure 3.10 shows; by changing the BaO/SiO_2 ratio from 0.6 to 0.94, the TEC changes from 7.6- to $14.6 \cdot 10^{-6}$ °C^{-1}. For the same glass system, the glass transformation temperature and the softening temperature could be effectively tailored by varying the alumina content as shown in Figure 3.11.

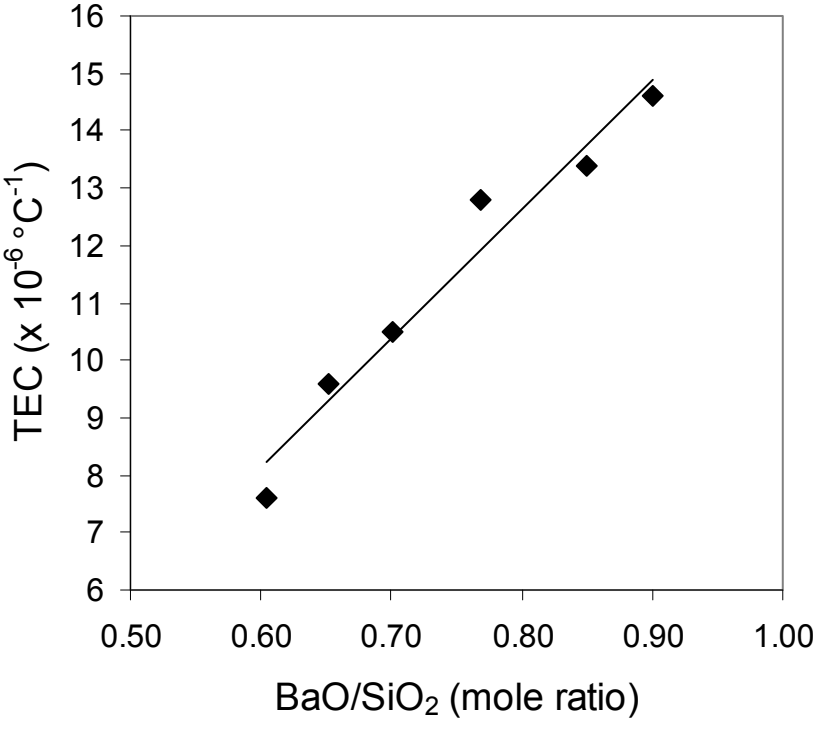

Figure 3.10
Effect of BaO/SiO_2 ratio on the thermal expansion coefficient in a BAS glass with composition $(33.7\text{-}45)BaO\text{-}(5\text{-}10.5)Al_2O_3\text{-}(50\text{-}57.5)SiO_2$ [65]

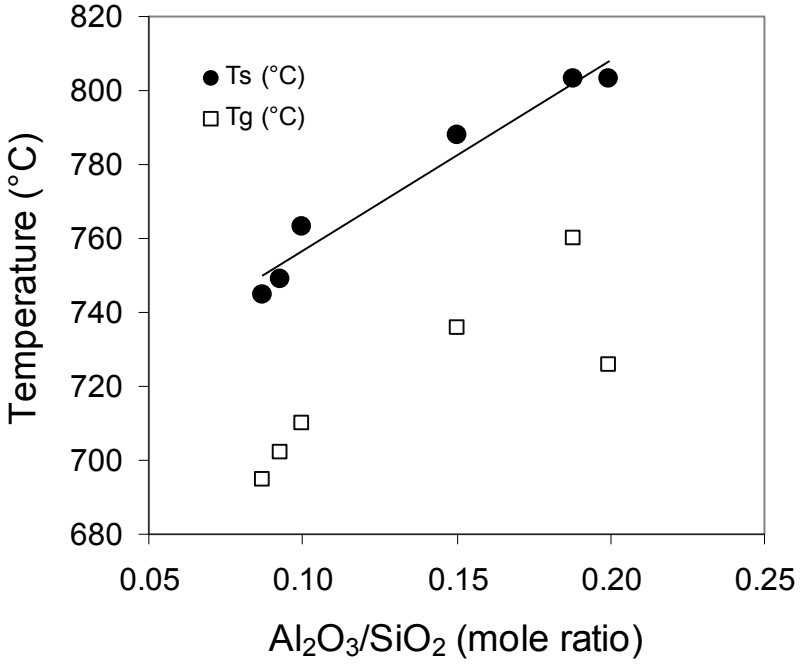

Figure 3.11
Glass transition temperature T_g and softening temperature T_s as function of the alumina/silica ratio of the BAS glass (33.7-45)BaO-(5-10.5)Al_2O_3-(50-57.5)SiO_2 [65]

3.6.3 Silicates without alumina

Glass forming ability, optimization of seal glass properties and electrical properties of glasses in the system RO-BaO-SiO_2 where R=Mg and Zn, have been investigated by several groups [82, 84 and 102]. A wide range of compositions were tested but only a few fulfilled the demands for thermal expansion for SOFC seal applications. Two glasses with the composition (mol %); 27BaO-18MgO-15B_2O_3-40SiO_2 and 27BaO-10MgO-8ZnO-15B_2O_3-40SiO_2 were identified as potential seal glasses for steel alloy interconnect. Both glasses were added B_2O_3 to improve wetting and reduce the tendency for crystallization during sealing.

3.6.4 Other systems

Phosphosilicates as SOFC seal glass have been studied by Larsen et al. [38, 39]. They concluded that the most stable glasses had too low TEC (5-6·10^{-6} $^{\circ}C^{-1}$) for SOFC applications. Seal glasses in the system BaO-La_2O_3-SiO_2 can be made with a TEC tailored for sealing gas membrane reactors with La_2NiO_4 membrane. A series of glass compositions in this system, patented by Budd [50], was designed to give thermal expansion coefficients in the range 12-14·10^{-6} $^{\circ}C^{-1}$ as shown in Figure 3.12. The composition of the

glasses was in the range: (16.7-37.8)BaO-(5-14.3)La_2O_3-(54-70)SiO_2. The thermal expansion coefficient increased with increasing content of BaO.

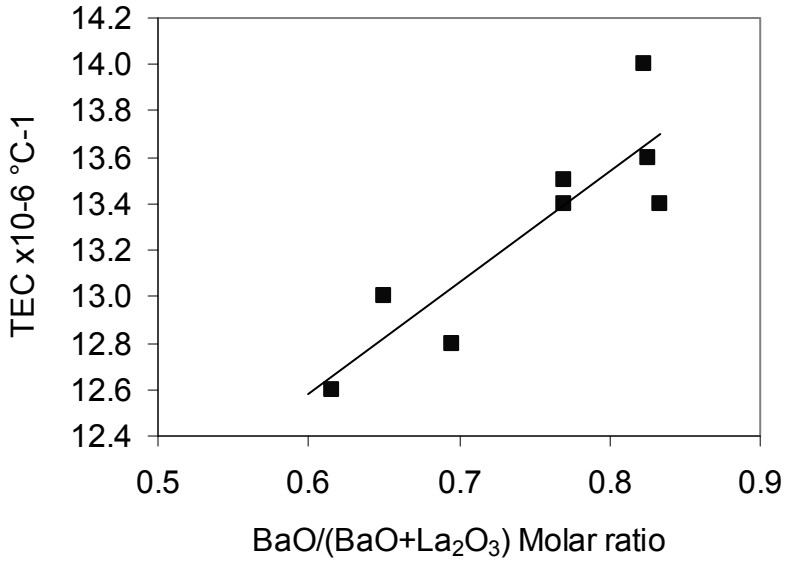

Figure 3.12
TEC as a function of BaO content of a BLS glass with composition (16.7-37.8)BaO-(5-14.3)La_2O_3-(54-70)SiO_2 [50]

3.6.5 Reactions between the seal and the joining materials

Secondary phases that arise due to reaction or interdiffusion between the seal and the joining materials can be detrimental not only to the seal, but also to membranes, electrolytes, electrodes and interconnects. The number and composition of the secondary phases are determined by the composition of the joining materials and of the temperature and atmosphere they are exposed to. It is beyond the scope of this work to make a full review of all systems that have been evaluated but it is of crucial importance to understand the interfacial reactions in order to be able to make stable and reliable power systems based on SOFCs and HT membrane reactors. Generally secondary phases with low or high thermal expansion compared to the pure seal and the joining components must be avoided, i.e. phases with TEC below 8-9·10^{-6} °C^{-1} and above 14-15·10^{-6} °C^{-1}

To demonstrate the complexity of many seal/membrane systems the work of Lahl et al. [103] will be shortly reviewed. Lahl et al. studied the reactions between a series of boron-aluminium-silicate glasses with MgO, CaO and BaO as modifiers as shown in Table 3.4. The glasses were tested as seal against 8-YSZ electrolyte, Ni anode, and the interconnect candidates oxide

dispersion strengthened (ODS) $Cr5FeY_2O_3$ and Fel8CrAl. Both diffusion couples and powder mixtures were made. The materials were exposed to oxidizing conditions (air) and reducing conditions (humidified H_2) at 1000 ˚C for up to 1000 h.

Table 3.4
Glass compositions (mol %) for evaluating reactions between seal glass, electrolyte and metallic interconnects [103]

Label	BaO	CaO	MgO	SiO_2	Al_2O_3	B_2O_3	TiO_2
BAS	45			45	5	5	
CAS		45		45	5	5	
MAS			45	45	5	5	
MAS10			40	45	10	5	
MAST10			38	45	10	5	2
MAST5			43	45	5	5	2
MAST12			35.6	43.1	12.8	3.6	4.9

Each glass contained 4 or 5 components, and the interconnect alloys contained at least 3 components giving a total of at least 8 components that can react with each other. According to the reduced phase rule[1], 8 components can result in 9 phases. Lahl et al. reported totally 10 new phases in the reaction between CAS glass and the 4 SOFC materials: as given in Table 3.5. In addition comes phases that can form in the crystallised glass.

Table 3.5
Secondary phases formed during reaction between CAS glass and 4 selected SOFC materials at the anode side [103]

Ni		YSZ		ODS ($Cr5FeY_2O_3$)		Fe18CrAl
Air	Red	Air	Red	Air	Red	Air
$CaSiO_3$	$CaSiO_3$	$CaSiO_3$	$CaSiO_3$	$CaSiO_3$	$CaSiO_3$	$CaSiO_3$
NiO	Ni	$CaAl_2Si_2O_8$	Ca_2SiO_4	Cr_2O_3	Cr_2O_3	$(Fe_{0.6}Cr_{0.4})_2O_3$
		$Ca_3ZrSi_2O_9$	m-ZrO_2	$Ca_3Cr_2Si_3O_{12}$	$Ca_3Cr_2Si_3O_{12}$	$Ca_3Cr_2Si_3O_{12}$

The BAS glass resulted in a similar number of secondary phases. The seal glasses containing BaO and CaO turned out to be useless due to severe reaction with the joining materials. The phase m-ZrO_2 formed in the

[1] The general phase rule is given as: P+F=C+2 where P is the number of phases, F the degrees of freedom (temperature, pressure) and C the number of components. For ceramic systems the vapour pressure is very low for large variations in temperature, for such systems the pressure variable can be neglected. In this case the *condenced* phase rule can be applied: P+F=C+1.

reaction between CAS and 8YSZ, which exhibits high specific volume compared to stabilized zirconia and is detrimental in this application. Another detrimental phase is cordierite ($Mg_2Al_4Si_5O_{18}$) formed in several interaction studies of MgO based glasses (MAS) with other components of SOFCs in agreement with the phase diagram of the MgO-Al_2O_3-SiO_2 system ([132] Figure 712). Cordierite has a low TEC ($2 \cdot 10^{-6}$ ˚C^{-1}) compared to that of other components of the fuel cell. The existence of this phase caused extended crack formation. However, by adding TiO_2 to the MAS base glass, formation of cordierite was hindered.

Cristobalite also occurs in many cases of interaction between sealant and steel alloy interconnects. Cristobalite undergoes a structural transformation below 200 ˚C connected with a large volume change. This volume change will cause microcrack formation during cooling from the sealing cycle.

Formation of $BaCrO_4$ is likely to occur when using glasses containing BaO as seal against chromium containing materials, i.e. the high temperature ferrochromium alloys. These alloys form a Cr_2O_3 protective scale during preoxidation before sealing. During the sealing process $BaCrO_4$ is formed. Two possible reactions can be imagined [70] as shown in eq. 3.9 and 3.10. The first is reaction between BaO and Cr_2O_3 scale (3.9). In humid atmosphere chromium oxyhydroxide $CrO_2(OH)_2$ (g) can be present and result in formation of $BaCrO_4$ and water vapour (eq. 3.10).

$$2Cr_2O_3(s) + 4BaO(s) + 3O_2(g) = 4BaCrO_4(s) \qquad 3.9$$

$$CrO_2(OH)_2 + BaO = BaCrO_4(s) + H_2O(g) \qquad 3.10$$

The gas can result in bubble formation in the seal. $BaCrO_4$ has a high thermal expansion ($16.5\text{-}33.8 \cdot 10^{-6}$ ˚C^{-1}) [69] that can result in delamination and microcracking. These are two reasons why BaO-containing glass/ceramics should be avoided as seal for chromium containing components. An alternative seal is a Na_2O-CaO-Al_2O_3-SiO_2 glass that showed good seal performance after 200 h at 800 ˚C in H_2-3 % H_2O atmosphere joining Crofer22APU and YSZ [104]. Reactions between seal and other SOFC components are also reported in several other reports [70, 80, 105-108].

3.7 Bonded compliant seals

Bonded compliant seals [109-111] are usually based on different kinds of Cu-Ag brazes added some active compound to give a strong binding to the joining components. At normal operation of the system brazes will to some extent be able to compensate for mismatch in thermal expansion due to their

ductile nature. The demand on thermal expansion matching is therefore lower for compliant bonded seals than for rigid bonded seals. On the other hand, since metal brazes are electrical conductors they are out of question as seals for SOFCs. Glass could also be a candidate if it was possible to avoid crystallization of the glass. Taken into account the long operation times demanded for commercial SOFC systems a glass seal will hardly remain compliant long enough.

3.8 Compressive seals

The high temperature compressive seal is like a gasket representing a simple and flexible seal concept. It makes the assembly of stacks as well as repair of malfunctioning cells easy, but requires an external pressure to keep the connections gas tight. This external pressure can only be achieved by a kind of load frame. To maintain high to moderate constant loads in oxidizing environment over the entire period of stack operation is a challenge. Material oxidation and load relaxation due to creep as well as added mass, volume, complexity and cost are all issues of concern with this seal design. Small-scale coupon testing indicates that non-oxidizing noble metals such as gold and silver [112] may be viable, but the question is how durable these gasket materials are in long term operation. In addition the noble metals are out of question anyway due to high cost. Additional concepts include using stamped metal gaskets of oxidation resistant alloys such as stainless steel and nickel-based superalloys. The gaskets are fabricated with deformable c-shape, corrugated or hollow tube cross sections. One example of corrugated metal gasket is shown in Figure 3.13 [113]. In this case the gasket is made of an austenitic alloy where either one side or both sides of the gasket can be filled with ceramic powder (clay, mica, etc.). However, an obvious disadvantage is that metals are electrically conductive and therefore are subject to potential problems with internal shorting [37].

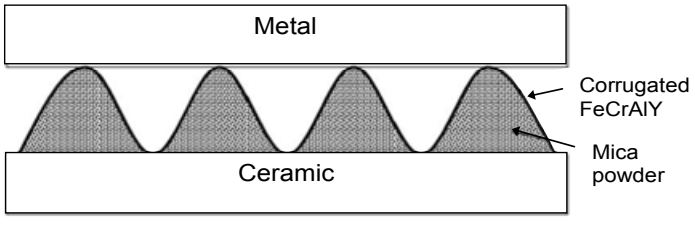

Figure 3.13
Compressive seal consisted of corrugated metal alloy sheet filled with ceramic fiber or powder [113]

The most promising compressive seals so far reported is based on either muscovite ,($KAl_2(AlSi_3O_{10})(F,OH)_2$, or phlogopite, $KMg_3(AlSi_3O_{10})(OH)_2$, mica [113]. These are flexible sheet minerals that can be formed into gaskets of any shape. The phlogopite micas have shown remarkably good durability at high temperatures despite decomposition due to release of water at temperatures below the operating temperature of the system. The principle is shown in Figure 3.14 a-c demonstrating 3 development steps of this concept. In the first concept (a) the seal was made of pure mica pressed between the ceramic and the metal interconnect, but this did not provide a hermetic seal for long time. Gas leaked both between the gasket and the joining components and between the individual mica sheets. The next seal (b) was a hybrid where glass or Ag was put on top and bottom of the mica seal. This resulted in an improved seal performance but still there was leakage between the individual mica sheets. By infiltrating the mica sheets with glass or metal to prevent leakage between the mica sheets (c) excellent seals have been made. The hybrid seals have shown good sealing performance both in long time testing (800 h) and in thermal cycling (20 – 800 °C) [96, 114-123]. The problem is that these seals are no longer purely compressive, but rather compliant bonded or rigid bonded seals.

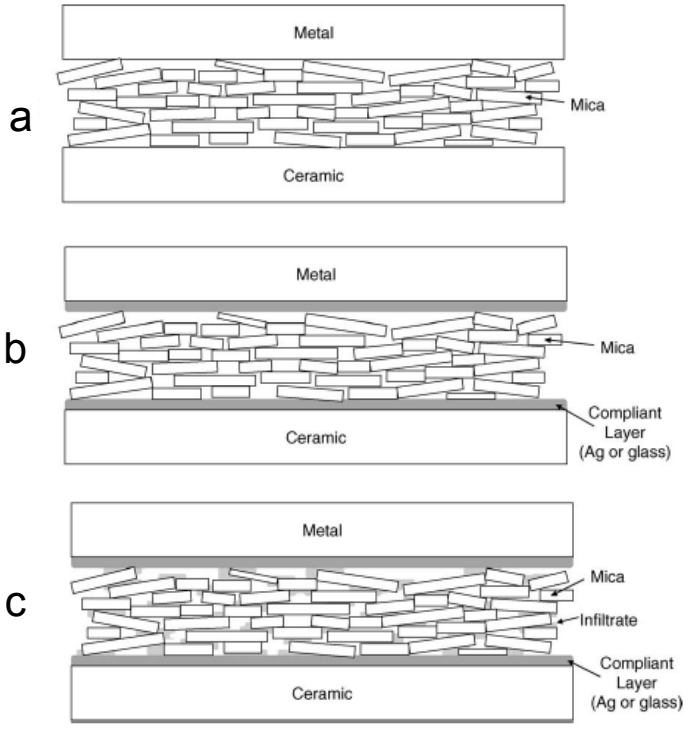

Figure 3.14
Three different development steps of compressive mica based seals. a) pure mica, b) Mica embedded between glass or metal sheets and c) mica infiltrated with glass or metal embedded between glass or metal sheets [96, 114-123]

4 Properties of aluminate glasses in the system CaO-Al_2O_3-R; R= MgO, BaO, SrO, La_2O_3.

4.1 Introduction

Two series of aluminate glasses have been evaluated with respect to applications as glass ceramic seals for HT-membrane reactors and SOFC. The first series was established from a CaO-Al_2O_3 (CA) base glass where CaO was gradually substituted by MgO making up the CAMn series with MgO content in the range 0-27.2 molar %. The second series denoted CAXm was less systematic with respect to composition and consisted of glasses in the systems CaO-Al_2O_3-X, where X=BaO, SrO and La_2O_3. The letters n and m are integers denoting the different compositions. The purpose was to evaluate silicate free seal glasses since there have been questions regarding the long term stability of silicates under SOFCs and high temperature membrane reactors operating conditions.

4.1.1 CaO-MgO-Al_2O_3 glasses

Glasses based on CaO-Al_2O_3 have been known since Shepard et al. published the phase diagram of this system in 1909 [48]. Seven years later Rankin and Merwin published the phase diagram of the system MgO-CaO-Al_2O_3 [133]. This system is still of great interest in the field of refractories, nuclear waste storage, new synthetic slags for secondary steel refining, etc. and late contributions to reveal further phase relations are found in [124 and 125]. Regarding the glasses of these systems they gained little interest until it was discovered that aluminate glasses transmitted electromagnetic radiation in near infrared (5-6 μm) [126]. This lead to the application of aluminate glasses in the guidance system of heat seeking missiles [127]. Another important application is in sealing of sodium lamps as aluminate glasses show excellent resistance against sodium vapour compared to silicate glasses [128]. The glass forming ability and glass stability of calcium aluminate glasses and glasses where Na, Sr and Ba were substituted for Ca, were investigated by Uhlmann et al. [129]. There is a narrow region of glass formation around 65 mol % CaO and 35 mol % Al_2O_3, but only for high cooling rates/small batches. Uhlmann et al. found that batches of 7 g of the base composition ($64CaO{\cdot}36Al_2O_3$) resulted in glass, while a batch of 20 g became completely crystalline. By substituting 6 mol % Na_2O, SrO or BaO for CaO, glass could be formed from batches of 100 g. Shelby [130] mapped the glass forming region of the calcium aluminosilicate system and showed that small additions of silica (<5 mol %) increased the glass forming ability substantially.

Calcium aluminate glasses tend to contain hydroxyl groups. This can be seen as a large absorption band at approximately 3500 cm^{-1} in IR transmission spectra. Shelby et al. [131] showed that the hydroxyl content

could be reduced by a factor of 2 by addition of 5 mol % CaF_2 substituted for CaO. Other methods to avoid humidity are vacuum melting or melting in a dry atmosphere.

4.2 Experimental

4.2.1 Preparation of glasses

All glasses were made of the pure powdered raw materials shown in Table 4.1. The alkaline earth oxides were based on carbonates, while alumina was based on aluminium hydroxide. These raw materials loose weight during firing due to decomposition to the oxide and CO_2 or H_2O (or both depending on the raw material composition). Before the individual batch compositions were made the weight loss was measured on each raw material by heating well above the decomposition temperature in order to find the solid oxide content shown in Table 4.1.

Table 4.1 *Raw materials used for glass preparation*

Chemical	Supplier	Purity	Solid oxide content wt%
$MgCO_3$	Baker	P.a.	42.4
$CaCO_3$	Merck	P.a.	56.0
$BaCO_3$	Merck	P.a.	77.9
$SrCO_3$	BDH lab. suppl. UK	P.a.	70.2
$Al_2(OH)_6$	PROLABO	Rectapur	65.4
SiO_2	North Cape Minerals		>99.5
La_2O_3	Merck	LAB	>99.0

Six compositions in the CAMn-series and four compositions in the CAXm-series were prepared. The oxide composition of the glasses in the CAMn series is given in Table 4.2. The content of MgO is ranging from 0 to 27.2 mol %. The composition CA without MgO is denoted “base glass”. The compositions from the CAMn series are plotted in the phase diagram CaO-MgO-Al_2O_3 [124, 132] shown in Figure 4.1.The alumina content (mol %) is almost the same for all compositions lying in the range (37.3-38.7 mol %). The composition of the CAXm series is given in Table 4.3. The raw materials for each composition were mixed in polyethylene bottles together with 5 alumina grinding balls (ø 20 mm) by shaking for 1-2 minutes. All compositions were melted in platinum crucibles (100 ml) at 1550 °C for five to six hours (except CAM20 and CAM30, which were melted at 1650 °C).

Table 4.2 *Composition of glasses in the CAMn-series*

Glass identity	Weight %			Mol %		
	CaO	Al_2O_3	MgO	CaO	Al_2O_3	MgO
CA (base glass)	48.1	51.9	0.0	62.7	37.3	0.0
CAM5	45.0	52.6	2.4	58.2	37.4	4.4
CAM10	41.7	53.4	5.0	52.7	37.7	8.9
CAM15	38.3	54.1	7.6	47.7	37.9	13.4
CAM20	34.8	55.0	10.2	42.7	38.1	18.0
CAM30	27.5	56.7	15.8	32.7	38.7	27.2
CAM1	38.6	52.6	8.8	47.1	36.3	15.4

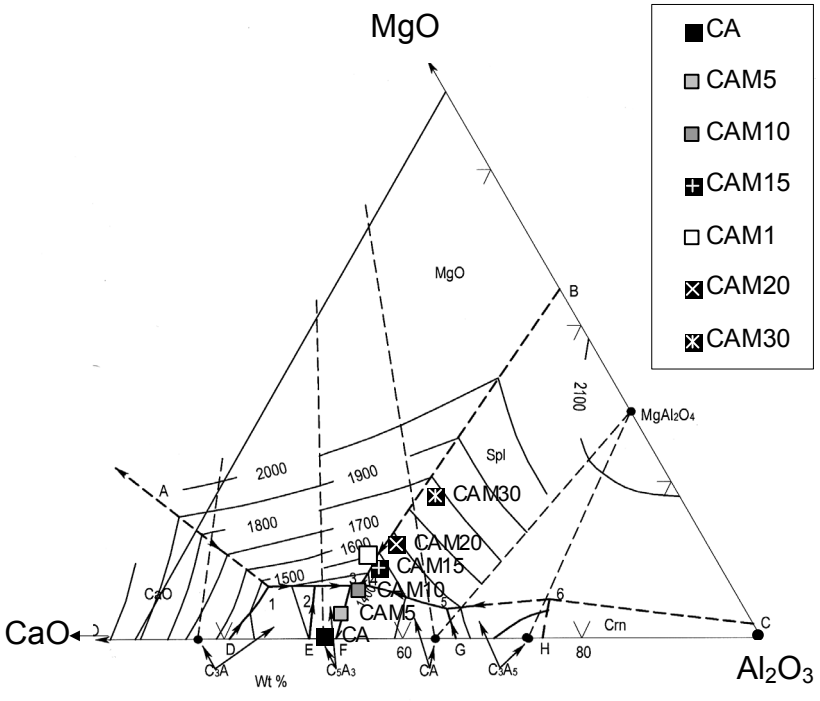

Figure 4.1
Phase diagram CaO-MgO-Al_2O_3 [133] showing the compositions of the glasses in the CAMn series

Table 4.3 *Oxide composition of glasses in the CAXm-series*

Glass identity	Weight %					Mol %				
	CaO	Al_2O_3	BaO	SrO	La_2O_3	CaO	Al_2O_3	BaO	SrO	La_2O_3
CAB1	38.0	52.0	10.0			54.1	40.7	5.2		
CAS1	38.0	52.0		10.0		52.7	39.8		7.5	
CAL5	41.2	48.4			10.4	57.7	37.3			2.5
CAL10	35.2	45.4			19.4	52.7	37.3			5.0

The batch size in each run was in the range 70-108 g resulting in 40-70 g of final product. The heating to maximum temperature was carried out in 4 steps with the following heating rates: 20-400 °C ; 200 °C/h, 400-1000 °C ; 100 °C/h, 1000-1300 °C; 200 °C/h and 1300-maximum temperature (1550- or 1650 °C); 50 °C/h. After the soak period the glasses were quenched by pouring the melt onto a 10 mm thick copper plate. To prevent cracking during cooling some of the samples were transferred to a hot furnace. The residual stress was removed by annealing at 800 °C for 1h followed by cooling at a rate of 30 °C/h to room temperature. The glass yield was calculated by comparing the weight of glass product with the theoretical yield calculated from the batch weight.

4.2.2 DSC-analysis

Thermal analysis was made on each glass composition in the temperature range 20-1350 °C using a NETZSCH STA 449 Jupiter differential scanning calorimeter (DSC). The glass was crushed to particle size 45-150 μm before the measurement and the heating and the cooling rates were 10 °C /min. The sample weighed from 33 to 50 mg and both the sample and reference crucibles were made of alumina.

4.2.3 Crystallization and powder X-ray diffraction

A piece (1-3 g) of each glass composition except for CA and CAM30 was crystallised in air at 1050 °C for 72 hours in a tube furnace and placed on an alumina sample holder. The heating rate was 200 °C/h. Cooling was performed by moving the alumina sample holder to the cold end of the furnace and turning off the power. After 15 minutes the samples were removed from the furnace. Qualitative powder X-ray diffraction (XRD) analysis was performed on samples milled to particle size < 45 μm by using a Siemens D5005 diffractometer with CuKα radiation and secondary monochromator.

XRD of CA was made on a sample that had been heated to 1000 °C twice in the dilatometer (see chapter 4.2.4). XRD of sample CAM30 was made on the glass as quenched. Samples with n>5 needed longer time or higher temperature to achieve a stable crystalline phase composition. Sample CAM10 was therefore refired twice at 1300 ˚C for 20 h. CAL5 and CAL10 were not evaluated with respect to crystalline phases.

4.2.4 Dilatometry

Thermal expansion of selected compositions was performed both on annealed glass samples and on pressed tablets of glass powder (< 45 μm). Typical sample length was 10-15 mm and sample diameter 5-10 mm. The

measurements were performed in air using a Netzsch dilatometer type 402E. The heating and cooling rates were 2 °C /min and holding time at maximum temperature of 5 min.

4.2.5 Density

The density was measured by the Archimedes method (ISO 5017) using distilled water as immersion liquid. The samples were glass fractures (3-13 g) as quenched and crystallised samples.

4.2.6 Durability in water

Weathering of the glasses in water was investigated by keeping glass pieces (1.2-1.4 g) in distilled water in glass bottles for several months at room temperature. The amount of water was ca. 42 g pr. gram sample. All samples were dried at 110 °C and weighed before the test, and two times during the test. The glass pieces were visually observed daily. Ph of a suspension of distilled water and glass powder of the composition CA with particle size <80 μm was measured after 30 minutes. After 24 h the suspension was dried and the powder was analysed by XRD.

.

4.3 Results

4.3.1 Visual observations

To test the mixing procedure of the raw materials the measured weight of glass products was compared to the calculated yield. The results showed yields above 99 % and confirmed that the mixing of the constituents was satisfactory and that the nominal composition was close to the real composition. During quenching, the glass melt formed to button shaped bodies 40-50 mm in diameter and ~ 10 mm thickness in the centre. The base glass CA was almost completely crystalline except for a ~ 1 mm layer in intimate contact with the copper plate. This layer was a fully translucent glass slightly yellow in colour. The rest crystallised to a brownish glass ceramic material (see Figure 4.2 a1 and a2). The compositions of CAM5, CAM10 and CAM15 and CAM1 resulted in homogeneous, translucent and yellow glasses as shown in Figure 4.2 for CAM10 and CAM15. CAM20 was partly crystallised while CAM30 was not possible to get out of the crucible due to apparently high viscosity and was not characterized any further. Occasionally small spots in the glass became crystalline usually caused by the last droplets of glass melt from the platinum crucible.

For the CAXm-series the compositions CAB1 and CAS1 became transparent yellow glasses after quenching. No visible sign of crystallization was observed. CAL5 behaved like the base glass CA. Most of the material was crystalline except for a ~1 mm layer that first came in contact with the

Cu plate. CAL10 was difficult to get out of the crucible. Only a small volume from the top of the melt came out and this partly crystallised during quenching. The rest became an opaque crystalline material with a green-grey colour. Most of the samples cracked during the quenching on the Cu plate demonstrating that all samples had considerable residual stresses after quenching.

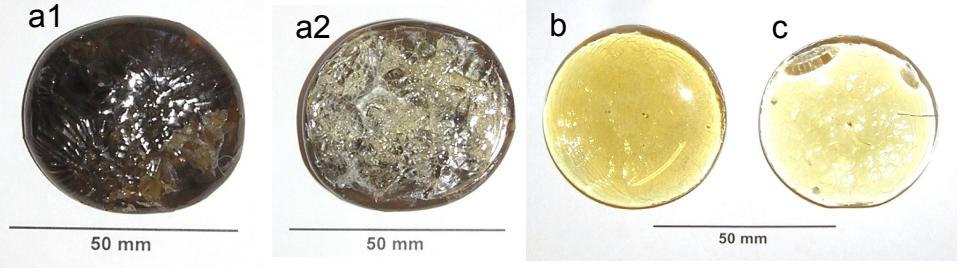

Figure 4.2
Glass compositions CA, CAM10 and CAM15 after quenching from 1550 °C by pouring the melt on a copper plate. The picture shows; Glass CA top face up (a1), CA bottom face up (a2), CAM10 top face up (b), CAM15 top face up (c)

4.3.2 Glass transition and glass stability

The DSC curves for the CA-CAM20 glasses in the CAMn series are shown in Figure 4.3. From the DSC pattern the glass transition temperature T_g, the completion of glass transition region $T_{g'}$ and onset temperature for crystallization T_x can be derived as described in chapter 3.5. All glass compositions crystallise in the region 915-968 °C showing distinct exothermic events due to crystallization. It is also possible to clearly distinguish the glass transition region showing both T_g and T_g'. Table 4.4 summarizes the temperatures for T_g, T_g', $\Delta T_g = T_g'-T_g$, T_x and T_x-T_g (glass stability) for all the glasses. The uncertainty in the temperature measurements is estimated to ±3˚C. T_g, T_x and T_x-T_g for the CAMn-series are shown graphically in Figure 4.4. There is a linear decrease in T_g of -2.5 °C for each mol % of MgO substituted for CaO. The crystallization temperature T_x, decreases slowly with increasing content of MgO from 940 °C for CA to 915 °C for CAM20 (17.8 mol % MgO). The glass stability (also denoted glass forming ability) T_x-T_g (Figure 4.4), is increasing up to 13.5 mol % MgO where it passes through a maximum at 133 °C.

Table 4.4

Glass transition temperatures T_g and $T_{g'}$, onset temperature for crystallization and glass stability region (T_g-T_x) for evaluated glasses. The estimated uncertainty is ± 3 °C

Glass identity	T_g (°C)	$T_{g'}$ (°C)	ΔT_g (°C)	T_x (°C)	$T_x - T_g$ (Stability) (°C)
CA	841	877	36	940	99
CAM5	824	865	41	939	115
CAM10	807	848	41	934	127
CAM15	803	845	42	936	133
CAM20	794	835	41	915	121
CAB1	857	894	37	968	111
CAS1	858	899	41	959	101
CAL5	833	880	47	952	118

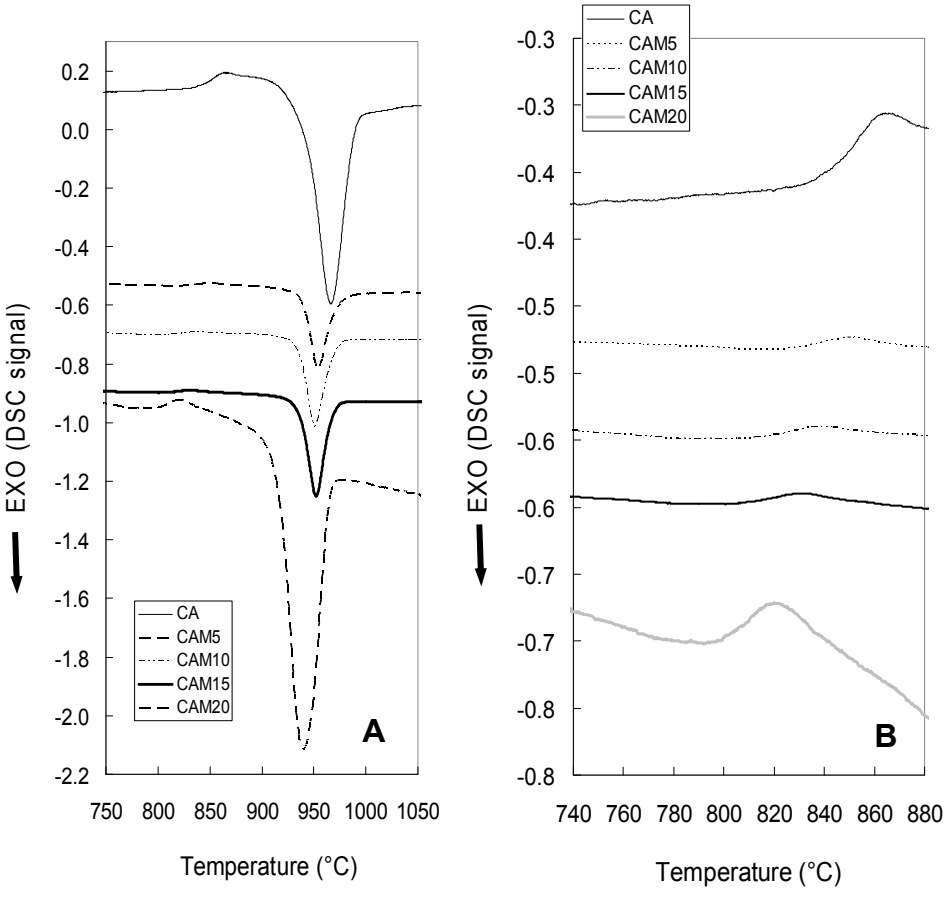

Figure 4.3

DSC-curves of glasses in the CAMn-series, showing the temperature region where glass transition and crystallization occurred (A). An enlarged part of the glass transition region is shown in Figure 4.3 B

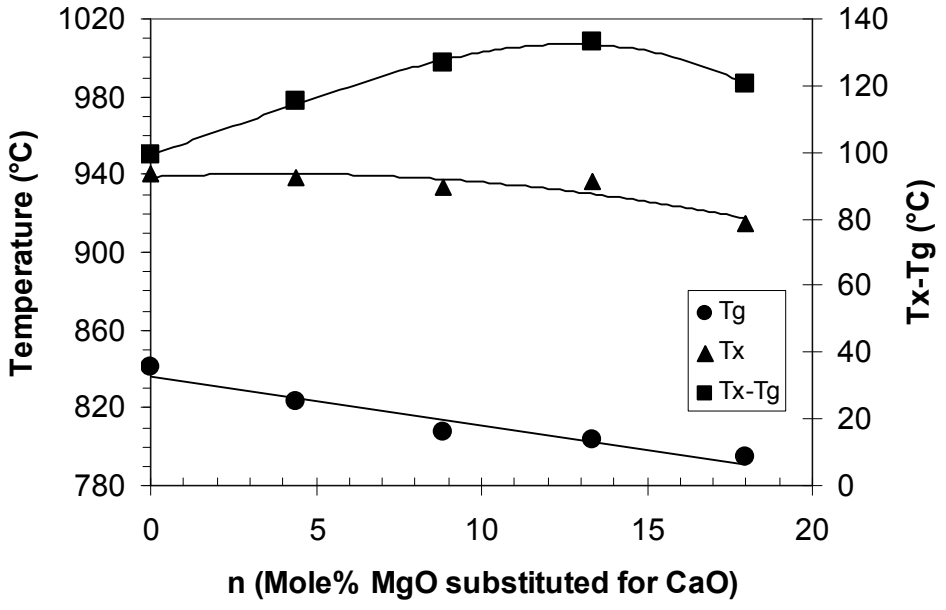

Figure 4.4
Glass transition temperature T_g, onset temperature for crystallization T_x and glass stability region T_x-T_g derived from DSC-measurements on glasses in the CAMn-series

Based on the measured data for T_g and T_g', the temperatures for given viscosities (isokons) and the viscosity versus temperature can be estimated by using eq. 3.5. Calculated temperatures for dilatometric softening point T_d (log(η)=10.3 Pa·s), softening point T_s (logη=6.6 Pa·s) and working point T_w (log(η)=3 Pa·s) for some of the CAMn and CAXm glasses are summarized in Table 4.5. Also shown is the viscosity expressed as log η (η is given in Pa·s) for the glasses at 1300 °C and 1550 °C.

Table 4.5
Calculated temperatures for T_d, T_s and T_w and viscosities at 1300 ˚C and 1550 ˚C for glasses in the CAMn and CAXm series

Glass identity	Dilatometric softening point T_d (°C)	Softening point T_s (°C)	Working point T_w (°C)	log(η/Pa·s) 1300 °C	log(η/Pa·s) 1550 °C
CA	859	935	1077	0.372	-1.07
CAM5	844	937	1111	0.985	-0.51
CAM10	828	914	1073	0.556	-0.84
CAM15	824	912	1075	0.609	-0.79
CAM20	814	899	1055	0.389	-0.96
CAB1	876	953	1097	0.564	-0.95
CAS1	878	963	1121	0.911	-0.67

The results demonstrate that all glasses are nonviscous at high temperatures. The "fragility" of the glasses can be evaluated from the fragility plot shown in Figure 4.5, where log(η) is plotted as function of the dimensionless temperature T_g/T (K/K). Viscosity measured by Urbain [134] for a composition close to the base glass CA is also shown in Figure 4.5. The results show that all glasses are to be considered fragile. From the Figure it can be seen that the base glass CA is the most fragile while the lanthanum substituted glass CAL5 is the least fragile. For the CAMn series the least fragile glass is CAM5 and the most fragile is CAM20. However CAM10 is found to be more fragile than CAM15.

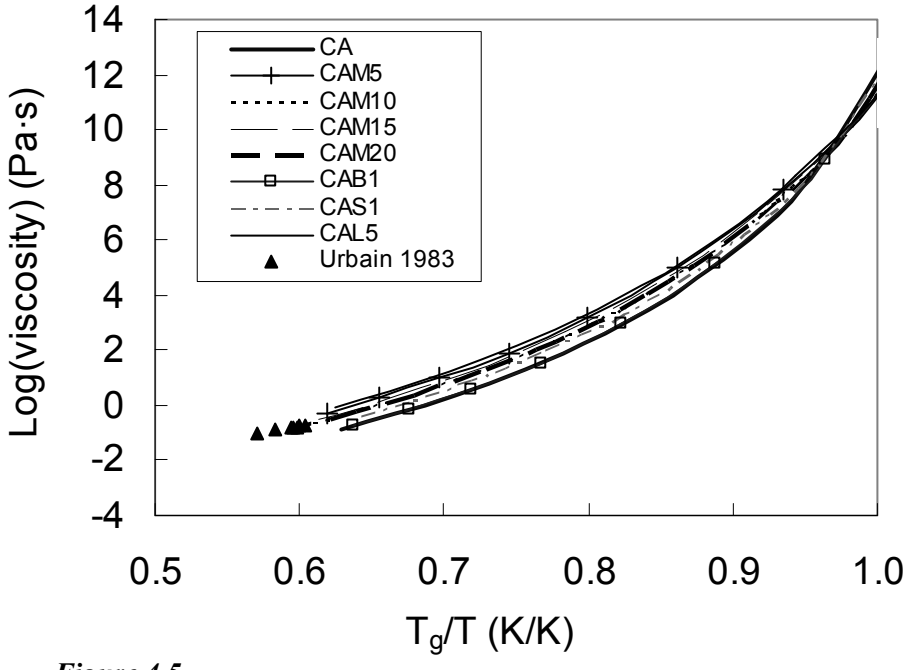

Figure 4.5
Fragility plot of selected glasses from CAMn and CAXm series. Data from Urbain for a calcium aluminate glass is also shown for comparison [134]

4.3.3 Thermal expansion

Besides TEC also T_g and the dilatometric softening point, T_d, can be retrieved from the dilatometric measurements. The thermal expansion around the softening temperature for selected compositions is shown in Figure 4.6. All samples have a linear expansion up to the glass transition temperature.

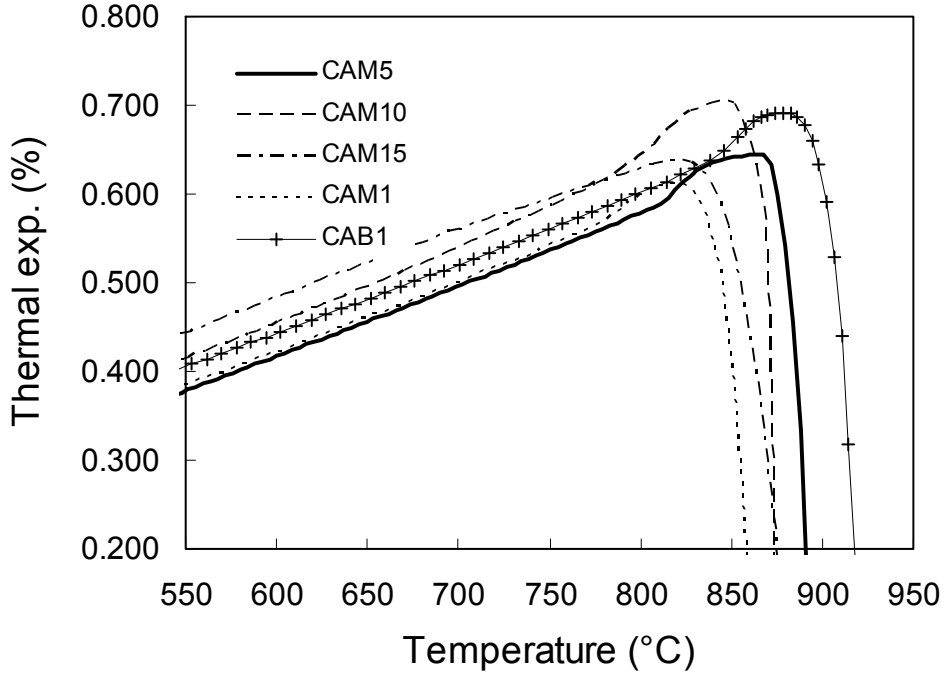

Figure 4.6
Thermal expansion curves to temperatures above the dilatometric softening point for glasses in the CAMn-series.

For all samples except CAM15, T_g can be determined with reasonable accuracy (±5 °C). The dilatometric softening temperature, T_d, was determined at the point of maximum thermal expansion and TECs were calculated in the temperature range 20-700 °C during heating. The results are given in Table 4.6 and in Figure 4.7. Both T_g and T_d follow the same trend as the corresponding data from the DSC measurements.

Table 4.6
T_g, T_d and TEC from dilatometric measurements, and difference between T_g *measured by DSC and T_g measured by dilatometry.*

Sample identity	T_g (Dil.) (°C)	T_d (Dil.) (°C)	T_{gDSC}-T_{gDIL} (°C)	TEC 20-700 °C ($x10^{-6}$ °C^{-1})
CA	847	859	-6	5.8
CAM5	811	867	13	7.5
CAM10	791	847	16	7.9
CAM15	777	824	26	8.1
CAM1	780	820		7.2
CAB1	840	876	17	7.4

T_d measured by the dilatometer decreases by 4.8 ˚C for each mole MgO substituted for CaO. The TEC shows a maximum at 10-12 mol % MgO of ~ $8.0 \cdot 10^{-6}$ $^{\circ}C^{-1}$. The sample CAB1 indicates that BaO has a similar effect on the TEC as MgO. The T_g decreases with increasing MgO/CaO-ratio, and generally T_g measured by DSC is higher than the T_g measured by the dilatometric method. The TEC increases with increasing amounts of MgO substituted for CaO up to a maximum at around 12-13 mol % MgO.

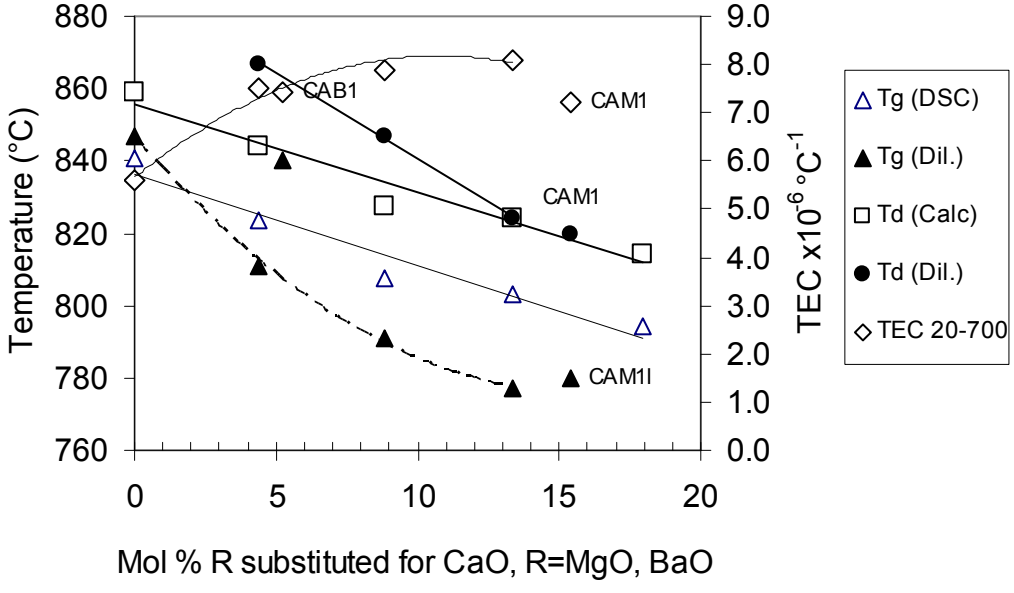

Figure 4.7
Glass transition temperature T_g(Dil.) and dilatometric softening point, T_d(Dil.) derived from the dilatometer measurements compared with the corresponding T_g(DSC) measured by DSC, and T_d (Calc) estimated by equation 3.5. Also shown (right axis) is the thermal expansion coefficient (TEC) for the glasses in the range 20-700 °C

4.3.4 Crystallised materials

The crystalline phases identified for the samples in the CAMn-series and the compositions CAB1 and CAS1 after crystallization, are given in Table 4.7. The identified phases are marked with x, the + sign indicates which phases that are expected from the phase diagram in Figure 4.1. In most cases the identified phases are in accordance with the phase diagram.

Table 4.7
Crystalline phases identified (x) in glasses in the CAMn-series + CAB1 and CAS1 after 72 h at 1050 °C

Sample ID	Crystalline phases (B=BaO, C = CaO, M = MgO, A = Al_2O_3)							
	CA	C_3A	C_5A_3	$C_{12}A_7$	C_3MA_2	BA	M	MA
CA*				X+				
CAM5	X+		X	X+	+			
CAM10**	X+			X+	X+			
CAM15	X+				X+		X+	
CAM20	X+				X+		X+	
CAM30***			X		X		X	X+
CAB1	X+	+		X?		X+		
CAS1	X+	X+		X+				

* 2 x 1000 °C/5 min, **2x 1300 °C/20 h, *** XRD as quenched from 1650 °C, + Expected phase from phase diagrams [135]

4.3.5 Density

The density of the glasses is given in Table 4.8. The second column shows the density for the samples as quenched (glassy material) while the third column shows the density for the inverted glasses after crystallization for 72 h at 1050 °C.

The density for glassy samples of the CAMn-series for n=5 to 15 was 2.91±0.01 g/cm^3. For CA the density was measured to 2.66 g/cm^3. For the glasses in the CAX-series (X=BaO, SrO and La_2O_3) the density was measured to be in the range from 3.02 to 3.07 g/cm^3. After crystallization the density of CA increased, while the density for CAM5, CAM10, CAB1 and CAL5 decreased. The density for CAM15 and CAS1 was unaltered.

Table 4.8
Density measured by immersion method of glassy and crystalline samples (1050 °C/72 h)

Sample ID.	Density of glass (g/cm^3)	Density inverted glass (g/cm^3)
CA	2.66	2.69
CAM5	2.92	2.71
CAM10	2.91	2.81
CAM15	2.91	2.92
CAB1	3.07	2.99
CAS1	3.02	3.02
CAL5	3.02	2.92

4.3.5.1 Durability in water

Reaction with water was noticed after short time. Especially the CA-composition, which was partly crystalline, reacted fast. After a couple of days the other compositions also showed signs of reaction. The glasses became covered by a white dusty layer, which over time also covered the walls and the bottom of the bottles. The visible changes caused by the reaction with water are illustrated in Figure 4.8. Gas bubbles on the surface after 15 minutes soaking indicated that CA reacted fast with water. After 3 days bubbles could also be seen on CAM5 and CAM10. CA and CAM5 were covered by a white layer. pH of the water with fine grained powder of the CA composition showed that the pH stabilised at ~ 10.6 after 30 minutes and the powder turned into hard aggregates. pH of the distilled water was 7.0. XRD analysis of the CA sample after 24 hour exposure to water demonstrated formation of the hydrate phase; $Ca_3Al_2(OH)_{12}$ (Katoite) and the hydrated carbonate $Ca_4Al_2CO_9 \cdot 11H_2O$.

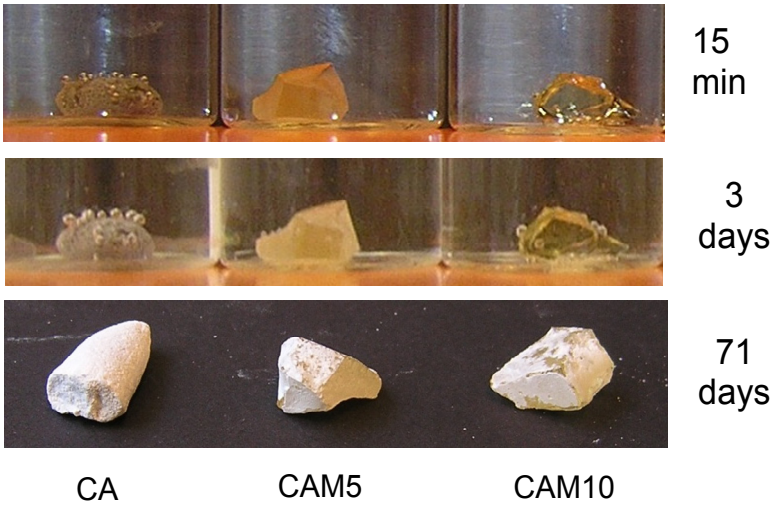

Figure 4.8
Visual impression of the reaction between distilled water and the glasses CA, CAM5 and CAM10 after 15 minutes and 3 days. Pictures of dried glass samples after 71 days show that all samples are covered by a white powder

4.4 Discussion

4.4.1 Glass stability

The glass forming ability of the CA composition was observed to be poor. When the melt was poured onto the copper plate only the part that first came into contact with the plate became glass, while the rest resulted in a brownish crystalline material. This demonstrates that the critical cooling

rate is relatively high, and that only the melt that came in direct contact with the copper plate was cooled fast enough to become glass. Smaller batches (<10 g) are expected to be glass forming. This observation is supported by the work of Uhlmann et al. [129].

Substitution of CaO by another alkaline earth oxide (MgO, BaO, SrO) increased the glass forming ability as expressed by the difference T_x-T_g between the crystallization temperature and glass transition temperature (see Table 4.4). The glass forming ability for the CAMn-series passes a maximum at approximately 12-13 mol % MgO (Figure 4.4) demonstrating that the optimum composition for glass making is somewhere in the range 10-15 mol % MgO. In order to locate the exact maximum further experiments have to be performed. It is also interesting to notice that the TEC (Figure 4.7) shows the same trend as the glass forming ability. The T_g for the CAMn series decreases almost linearly with increasing amounts of MgO, from 841 °C for 0 mol % MgO to 794 °C for 20 mol % MgO. The slope is ~ -2.8 °C for each mole MgO substituted. The CAB1 and CAS1 compositions have relatively high transformation temperatures of 857-858 °C while CAL5 has an intermediate T_g of 834 °C.

The calculated softening points (Table 4.5) are decreasing with increasing content of MgO. The T_s was 937 °C for MgO content of 4.4 mol % and 899 °C for 18 mol % MgO. The estimated working point temperatures show the same trend. The estimated viscosity at 1300 °C and 1550 °C demonstrate that all glasses are non-viscous at these temperatures. This is in accordance with the experience when the glass melt was quenched. The melts appeared non-viscous.

4.4.2 Viscosity

The calculated viscosities for the CAMn series and the CAB1 glass were compared to viscosity data published by Urbain [134] (Figure 4.5). Urbain does not give any information of the glass transition temperature, a T_g of 825 °C measured by Uhlmann et al. [129] for a similar glass composition as reported by Urbain was therefore used, in order to fit Urbains data into the fragility diagram. As can be seen, Urbains data fit well to the estimated viscosity from the calorimetric data.

4.4.3 Dilatometric measurements

The TEC between 20 ˚C and 700 ˚C for the CAMn-series is generally low but increases as more MgO is substituted for CaO. At 10-12 mol % MgO the TEC reaches a maximum of ~ $8.1 \cdot 10^{-6}$ $^{\circ}C^{-1}$. Thus the TEC may be adjusted to some degree by the amount of MgO added but the effect is limited. Thermal expansion of CA was measured on a piece of the quenched

glass that was partly crystalline. The dilatometer pattern showed a distinct glass transition but no softening point due to further crystallization and fast increase in viscosity.

T_g determined by DSC was systematically 12-26 °C higher than the T_g obtained from dilatometry (Table 4.6). This difference can be explained by the heating rate, which was 10 °C/min for the DSC and 2 °C for the dilatometer. Generally T_g increases when the heating rate increases [47]. The only composition that deviates from this trend is CA where T_g from the dilatometer is higher than T_g measured by DSC. The fact that the dilatometer sample was mostly crystalline and not glass can explain this since crystalline particles growing in a glass matrix will increase the viscosity and change the glass composition. The sample used for the DSC measurements was from the pure glassy phase that formed in contact with the copper plate when the glass melt was quenched.

4.4.4 Crystallised glass

The crystalline phases identified in the devitrified glasses of the CAMn-series were mainly in accordance with the phase diagram (Figure 4.9). For the sample CAM5 either the phase $C_{12}A_7$ or the more alumina rich phase C_5A_3 would be expected, however both phases were identified. There are

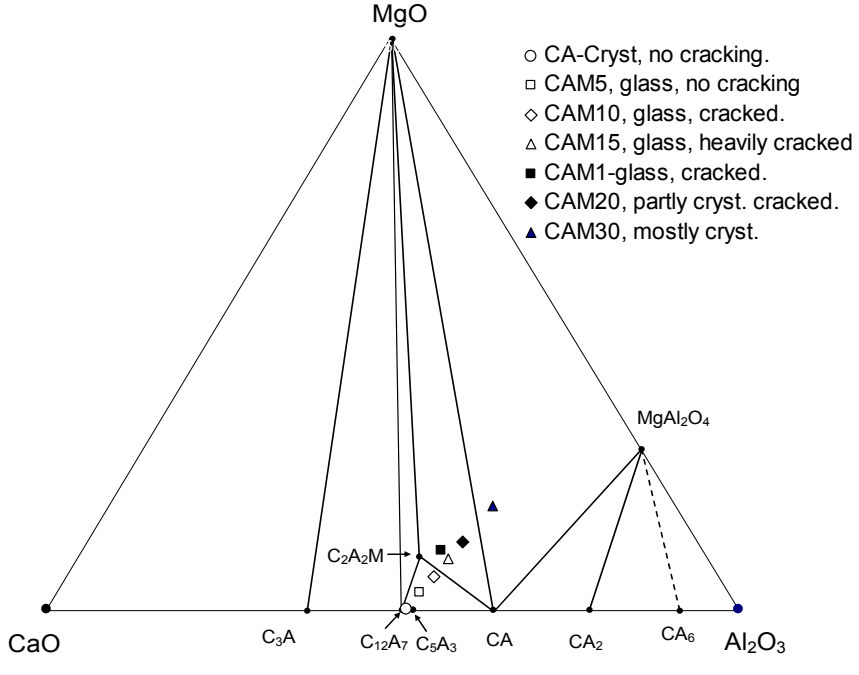

Figure 4.9
Phase diagram of the CaO-Al_2O_3-MgO system showing expected crystalline phases for the compositions in the CAMn-series [135, Figure 11300]

different opinions in the literature [124,136,137] whether the phase $C_{12}A_7$ is a pure phase or if it contains some water. According to Nurse et al. [137] the phase $C_{12}A_7$ enters into a reversible equilibrium with water in the temperature range 950-1350 ˚C. The phase can be described as $Ca_{12}Al_{14}O_{32}(OH)_2$ corresponding to a water content of 1.3 %. In the pure $CaO\text{-}Al_2O_3$ system the phase C_5A_3 would be formed. Since no special care has been taken in the present work to obtain completely dry atmosphere during the crystallization experiments it is reasonable that both mentioned phases can be formed. On the other hand the phase C_3MA_2 was expected from the phase diagram but was not observed. This can be explained by the deviation from equilibrium or by some solid solution of MgO. For sample CAM10, with the double amount of MgO compared to CAM5 the phase C_3MA_2 was identified as expected. Sample CAM30 did not contain the expected crystalline phases since the XRD analysis was made on the quenched sample. For the CAB1 and CAS1 glasses the identified crystalline phases are all expected from the phase diagrams ([135], Figures 2451 and 2484). In the BAS system there is extensive solid solution between CaO and SrO.

4.4.5 Density

Table 4.9 shows that the compositions CAM5 and CAM10 have a considerable lower density as crystallised material than as glassy material contrary to what is expected. One explanation might be that both these compositions contain the phase $C_{12}A_7$, which according to the X-ray powder diffraction files [135] (see Table 4.9) have a density, D_x, of 2.677 g/cm^3. The low density of $C_{12}A_7$ can explain the rather low density of the glass compared to the crystalline material. The density of the base glass CA was measured to be 2.69 g/cm^3 after the crystallization cycle (72 h at 1050 °C). This is reasonable since the only crystalline phase found in this composition was $C_{12}A_7$.

Table 4.9

Density data from powder diffraction files (PDF) for some phases in the MgO-$CaO\text{-}Al_2O_3$ system [135]

Phase	Density (g/cm^3)		PDF-file
Short form.	D_x Calculated	D_m Measured	
CA	2.945		01-070-0134
C_5A_3	3.040	3.030	00-011-0357
$C_{12}A_7$	2.677		00-009-0413
C_3MA_2	2.971	2.960	00-017-0737
MA	3.579		00-021-1152

M=MgO, C=CaO, A=Al_2O_3

4.4.6 Durability in water

The substitution of MgO for CaO increases the durability in water. From the XRD-pattern of the water treated powder of sample CA it is indicated that the white coating, which is observed in Figure 4.8 is a mixture of a hydroxide and a carbonate. The alkaline earth elements Ca and Mg form carbonates easily and the reaction goes faster when water is involved. The first step results in a hydroxide, which reacts further into a carbonate as shown in equations 4.1 and 4.2 where M=Mg, Ca, Sr and Ba.

Step 1: $MO + H_2O = M(OH)_2$ 4.1

Step 2: $M(OH)_2 + CO_2 = MCO_3 + H_2O$ 4.2

At elevated temperatures the hydroxides and carbonates will decompose. However as mentioned earlier, in atmospheres containing water vapour the hydroxide phase $C_{12}A_7O_{32}(OH)_2$ can be formed in the temperature range 950 ˚C-1350 ˚C.

4.4.7 Conclusion

The glass forming ability of $CaO\text{-}Al_2O_3$ based glasses with addition of a third oxide (MgO, SrO, BaO) has been investigated. The stability of the CA based glass increased with the addition of a third oxide, and a maximum in stability was observed with substitution of CaO with MgO. The glass transition temperature was observed to decrease with increasing MgO content, while the crystallization temperature was less dependent on the MgO substitution. The thermal expansion of the glasses was observed to increase with increasing MgO substitution.

The thermal properties of the glasses including glass transition temperature, crystallization temperature, softening point and viscosity have been established by thermal analyses. Finally durability tests have demonstrated that the glasses are not stable in contact with water at ambient temperatures.

5 Preparation of La_2NiO_4 and $LaNbO_4$ membrane materials

5.1 Experimental

5.1.1 $LaNbO_4$

The $LaNbO_4$ powder was processed by spray pyrolysis following the same route as described by Mokkelbost et al. [11]. The particular batch used in the present work was doped with 0.5 % Sr giving the composition: $La_{0.995}Sr_{0.005}NbO_4$, and the powder was calcined at 1000 °C. Different shapes (sheets with diameter 10-25 mm and 1 mm thickness and tablets ø 10-20 mm height 7-20 mm) were made by uniaxial pressing at 30-50 MPa. Tablets with ø 10 mm and height 15-20 mm were used to determine the sintering properties and thermal expansion of dense samples. Thermal expansion measurement was performed by heating the pressed tablet to 1400 °C in the dilatometer using the same procedure and equipment as described in chapter 4.2.4. Based on the sintering curve the program shown in Figure 5.1 was used for sintering the test samples: The sintering program was designed to obtain a dense material with as small grains as possible. X-ray diffraction was performed by using BRUKER Focus D8 diffractometer equipped with a solid state "Lynx Eye" detector. The density was measured using the Archimedian method in ethanol. The grain size was measured by use of an optical microscope.

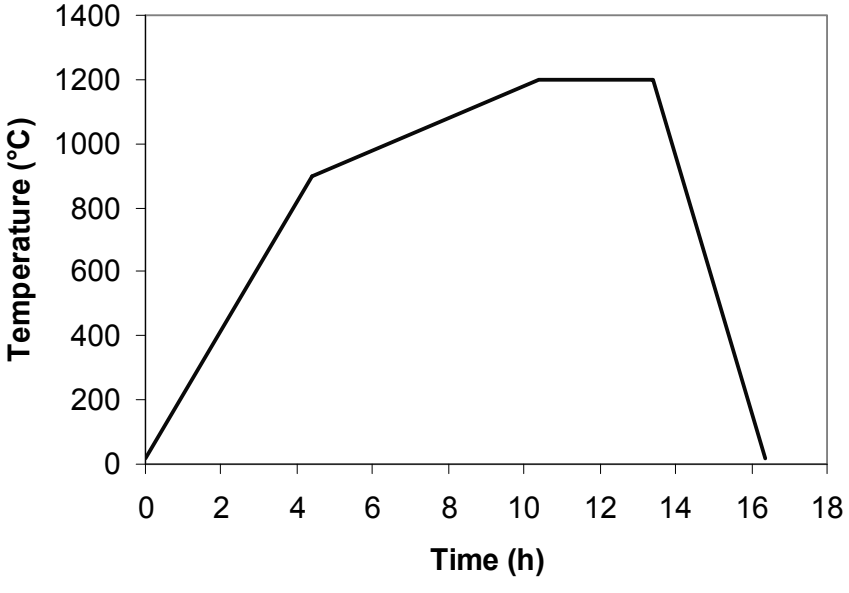

Figure 5.1 *Firing schedule for sintering of $LaNbO_4$ samples*

5.1.2 La_2NiO_4

The La_2NiO_4 powder was processed from metal nitrides dissolved in water by a similar spray pyrolysis method as used for $LaNbO_4$. After the spray pyrolysis the powder was calcined at 800 °C for 8 hours and wet ball milled for 18 hours in polyethylene bottle with zirconia balls (ø 4 mm) and isopropanol as liquid. The rest of the experimental procedure was the similar as for $LaNbO_4$. The La_2NiO_4 samples were sintered at 1320 °C for 1 or 2 hours using a heating rate between 1000 and 1320 °C of 40 or 50 °C/h. The heating rate from 20 to 1000 °C was either 200 or 300 °C/h and the cooling rate was either 300 or 400 °C /h as shown in Figure 5.2.

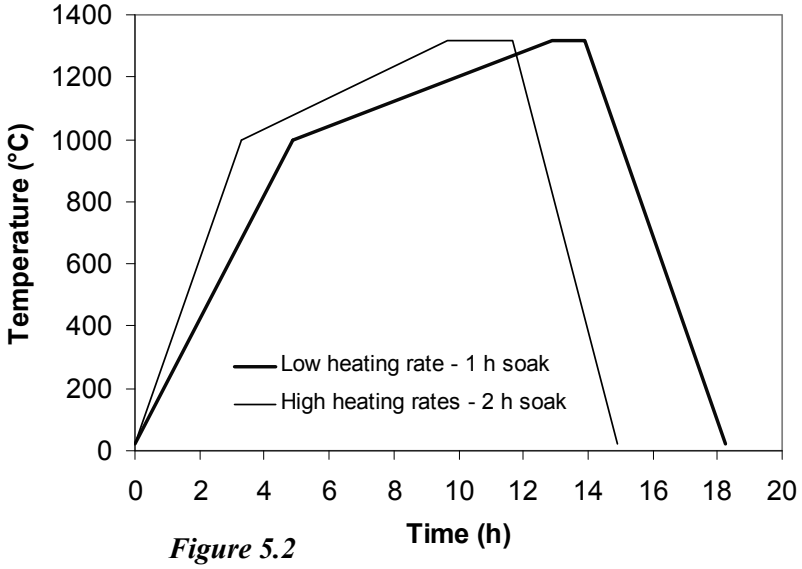

Figure 5.2
Firing schedules for sintering of La_2NiO_4 samples

5.2 Results

5.2.1 $LaNbO_4$

The X-ray pattern of the calcined powder is shown in Figure 5.3 demonstrating that the powder was phase pure. The structure identification in Figure 5.3 is from PDF file 01-081-1973 [138]. The sintering and thermal expansion curves are shown in Figures 5.4 and 5.5 respectively. The sintering of $LaNbO_4$ powder starts at ~ 900 °C and is finished at ~1300 °C. The sintering rate ($(\Delta L/L_0)/\Delta T$, % $°C^{-1}$) was almost constant between 900 and 1200 °C. The thermal expansion of dense $LaNbO_4$ shows a phase transition at ~ 530-540 °C. Below this transition temperature the thermal expansion coefficient was $13.3 \cdot 10^{-6}$ $°C^{-1}$ while above the transition temperature the TEC was $6.7 \cdot 10^{-6}$ $°C^{-1}$. With respect to sealing nonlinear

expansion behaviour might be a challenge. Immersion of the sintered samples in ethanol showed no weight gain demonstrating that the materials contained no open porosity. The densities measured were in the range 5.55-5.67 g/cm^3 or 95-97 % of the theoretical density. Optical microscopy showed a fully sintered material with grain size between 2 and 8 μm.

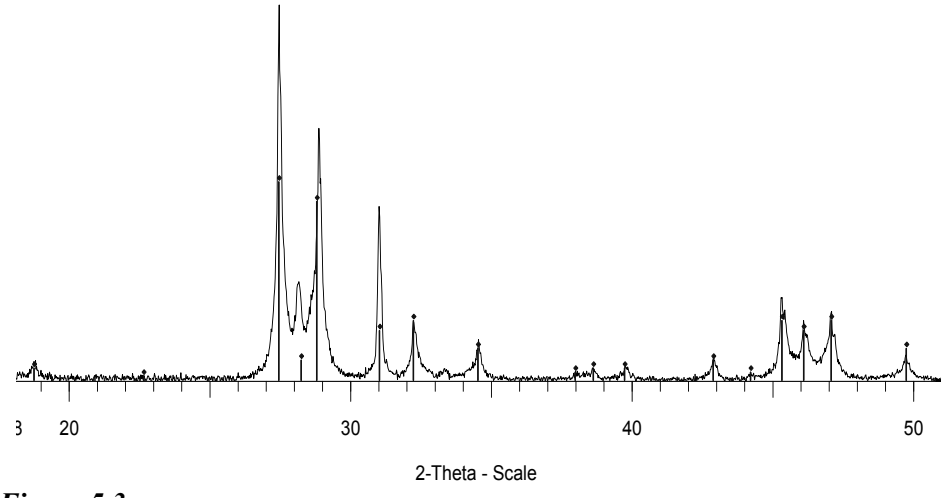

Figure 5.3
X-ray diffraction pattern of $LaNbO_4$ powder used for membrane material samples. The structure identification is based on PDF file 01-081-1973 [135,138]

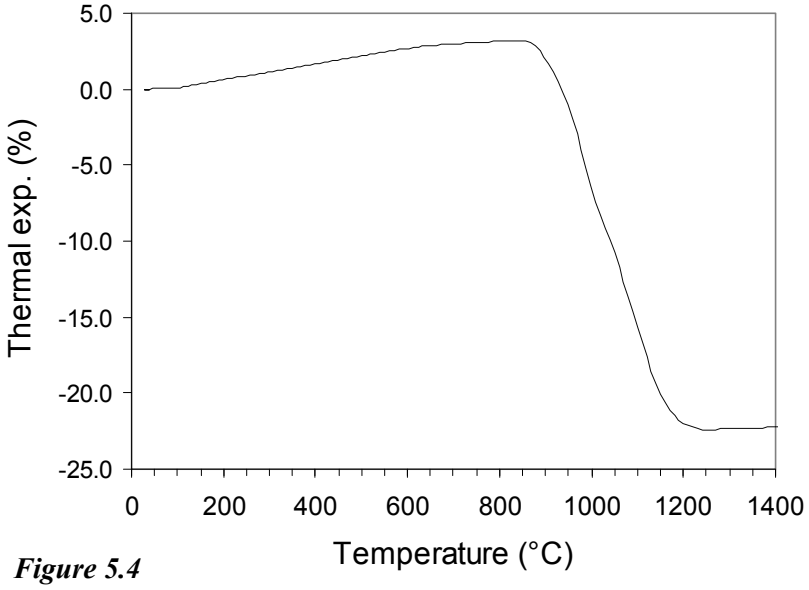

Figure 5.4
Sintering curve of $LaNbO_4$ obtained by a heating rate of 2 °C /min in air

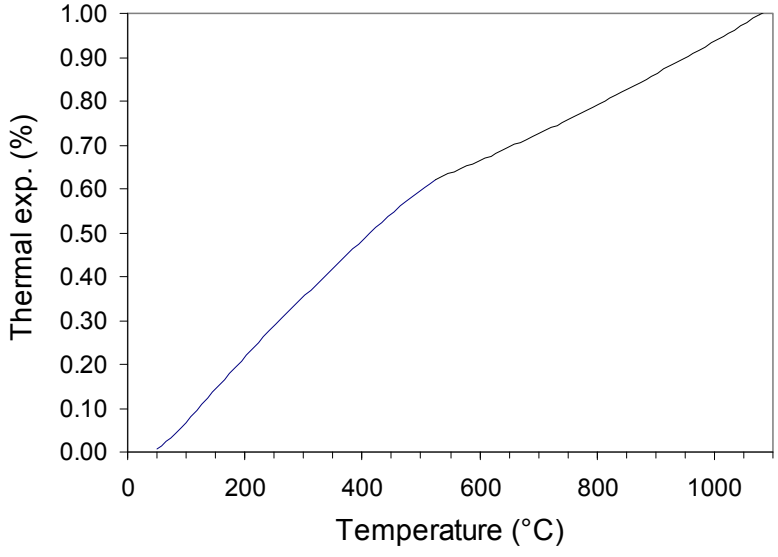

Figure 5.5
Thermal expansion of $LaNbO_4$ sintered at 1200 °C. TEC: 20-536 °C: 13.3 $\cdot 10^{-6}$ $°C^{-1}$, 536-1200 °C: 6.7$\cdot 10^{-6}$ $°C^{-1}$

5.2.2 La_2NiO_4

The X-ray diffraction pattern of La_2NiO_4 sintered at 1300 °C shown in Figure 5.6 demonstrates that La_2NiO_4 is the only phase identified.

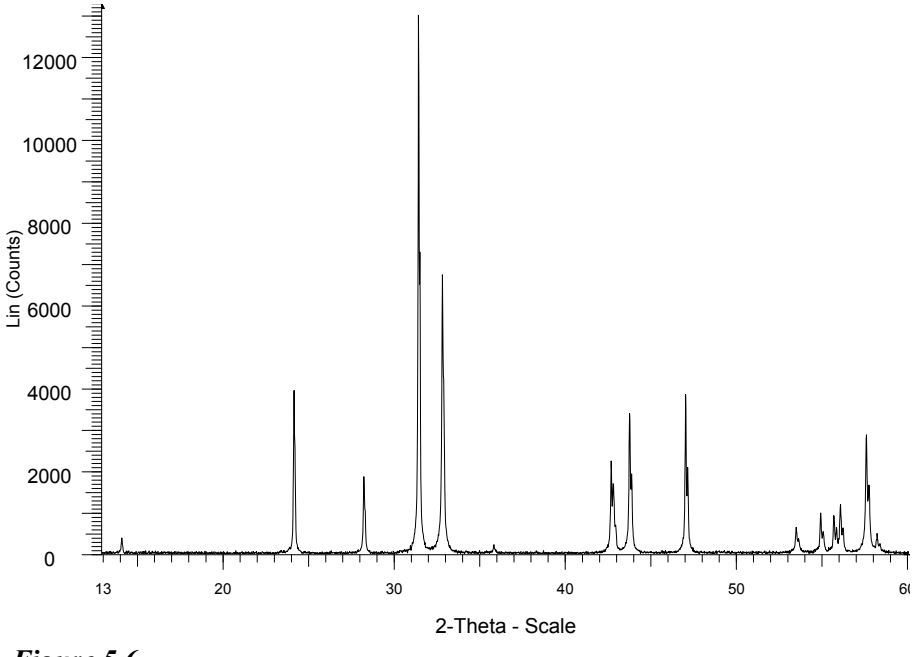

Figure 5.6
X-ray diffraction pattern of La_2NiO_4 powder sintered at 1300 °C demonstrating that the sintered material consists of only La_2NiO_4.

The dilatometric measurements showed that La_2NiO_4 starts to sinter at ~ 900 °C and that the sintering was finished at ~ 1300 °C as shown in Figure 5.7. The abrupt stop in the sintering curve is due to that the dilatometric measurement system passed the range limit. Thermal expansion of dense La_2NiO_4 is shown in Figure 5.8. The thermal expansion is almost linear from RT up to 1000 °C giving a TEC between 25 and 1000 °C of $12.4 \cdot 10^{-6}$ $°C^{-1}$. Optical microscopy of sintered samples showed a dense microstructure consisting of grains in the size range 1-8 µm. The density was in the range 6.64-6.70 g/cm^3 representing 94-95 % of the theoretical value.

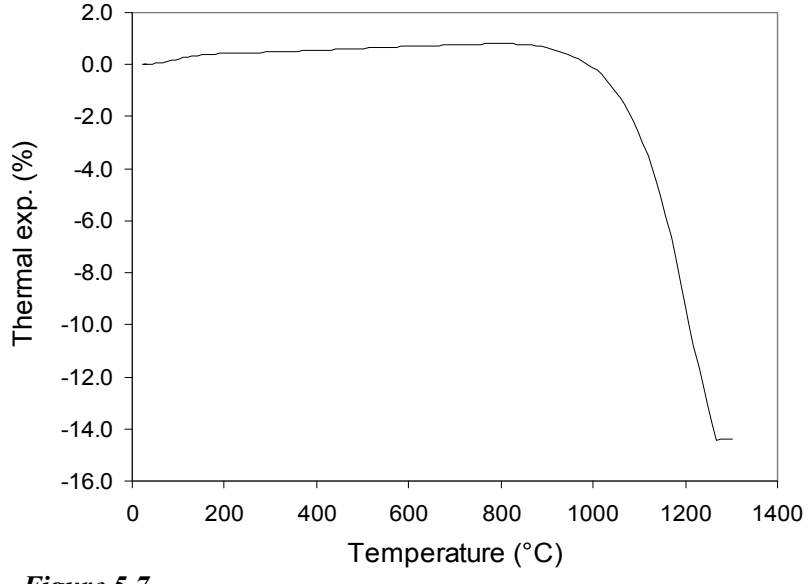

Figure 5.7
Sintering curve for La_2NiO_4 obtained by heating at 2 °C /min in air

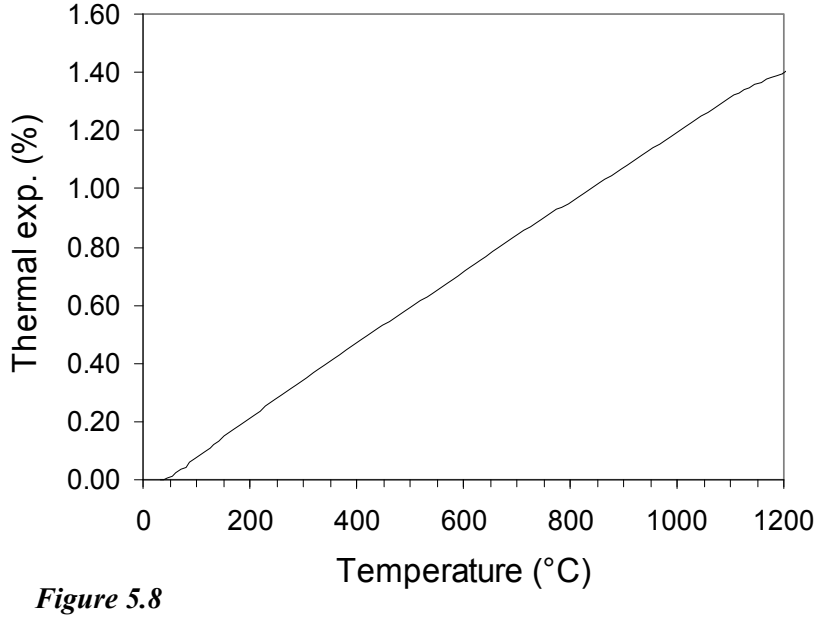

Figure 5.8
Thermal expansion of densified La_2NiO_4 in air at heating rate 2 °C/min

6 Reactions between calcium-magnesium- aluminate glass ceramic, $LaNbO_4$ and Al_2O_3

6.1 Introduction

The physical properties of the aluminate glasses evaluated in chapter 4 revealed that the compositions CAM10 and CAM15 have thermal expansion coefficients attractive for sealing of $LaNbO_4$ materials. To evaluate the chemical compatibility between the materials, the crystalline phases and microstructure were studied in powder mixtures of CAM10 and $LaNbO_4$ after heat treatment at high temperatures. In addition, two types of diffusion couples were prepared to study reaction mechanisms. The first diffusion couple consisted of CAM10 glass in contact with presintered $LaNbO_4$ or Al_2O_3. The second type of diffusion couple ("Flux test sample") was an assembly of a $LaNbO_4$ membrane joined to an Al_2O_3 substrate prepared to study the seal performance in a leakage test experiment (see chapter 8). Reactions between CAM-glass and $LaNbO_4$ and Al_2O_3 were studied by means of electron microprobe analysis (EMPA) and XRD.

6.2 Experimental

6.2.1 Preparation of powder mixtures

The aluminate glass denoted CAM10 (see Table 4.1) prepared as described in chapter 4.2.1, was milled in a planetary mill and the fraction with particle size < 45μm was separated by dry sieving. The $LaNbO_4$ powder was the same as described in chapter 5.1.1. Three different mixtures of the two powders (30/70, 50/50 and 70/30 wt %) were prepared. In addition one powder mixture of 50 wt % Al_2O_3 (sub micron powder from Martinswerk denoted "Martoxid MDS-6") and 50 % CAM10 glass was prepared. The calculated elemental compositions of the mixtures are given in Table 6.1.

Table 6.1
Nominal elemental composition of the CAM10 seal glass and of the powder mixtures CAM10/$LaNbO_4$ and CAM10/Al_2O_3

Mixture Composition	Mixture (wt. %)	Elemental composition (at. %)					
		Mg	Ca	Al	La	Nb	O
CAM10	100	1.0	6.0	8.6			19.9
CAM10/$LaNbO_4$	30/70	1.4	8.2	11.5	8.7	8.7	61.6
CAM10/$LaNbO_4$	50/50	1.9	11.7	16.4	5.3	5.3	59.4
CAM10/$LaNbO_4$	70/30	2.4	14.2	20.1	2.8	2.8	57.8
CAM10/Al_2O_3	50/50	1.3	8	32.5			58.1

Tablets with diameter 10-15 mm and height 15-25 mm were pressed, sintered and milled to particle size <45μm for XRD analyses. The heat

treatment of the different mixtures is given in Table 6.2. A flow sheet describing the preparation steps is shown in Figure 6.1.

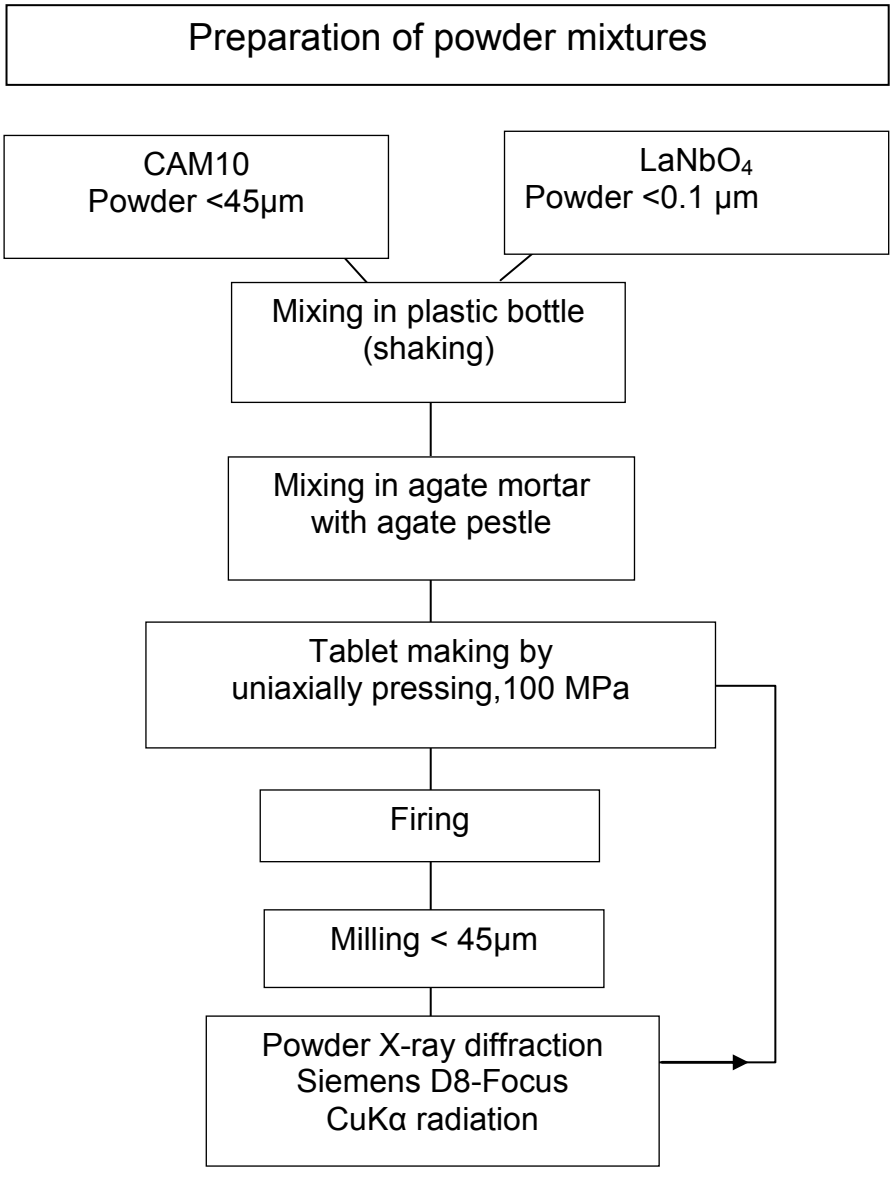

Figure 6.1
Flow sheet for evaluation of the crystalline phases formed during reaction between CAM10 glass powder and $LaNbO_4$ at elevated temperatures

***Table 6.2**. Heat treatment of powder mixtures of CAM10/$LaNbO_4$*

Cycle no.:→	1	2	3	4
Mixture (wt %) CAM10/$LaNbO_4$	Temp/Hold (°C/h)	Temp/Hold (°C/h)	Temp/Hold (°C/h)	Temp/Hold (°C/h)
30/70	1300/30	1300/40	1300/18	1375/100
50/50 (1)*	1300/30	1300/40		
50/50 (2)*	1375/20	1375/72		
70/30	1300/24	1250/40	1300/18	1375/100

* Due to experimental problems a new batch of mixture 50/50 had to be made after 2 heating cycles. The second batch, 50/50 (2), was fired twice at 1375 °C; 20 hours and 72 hours.

6.2.2 Preparation of diffusion couples

Four diffusion couples were prepared between the sealant glass and $LaNbO_4/Al_2O_3$. The $LaNbO_4$ and alumina tablets were polished with SiC-paper FEPA 1100 and cleaned 20 minutes in ultrasonic bath (ethanol) prior to the sealing. The first diffusion couple consisted of a $LaNbO_4$ tablet (diameter 10 mm) with the top face covered with a 1 mm layer of CAM10 glass powder dispersed in ethanol. On top of the seal a tablet of sintered alumina (Haldenwanger 99.7 % Al_2O_3) was placed as shown in Figure 6.2. Figure 6.2 also shows the composition of the 3 other diffusion couples. The heat treatment of the four diffusion couples is given in Table 6.3. Common for all is that the samples were heated to a high temperature for the seal to melt or sinter, and then held at a lower temperature for the seal glass to crystallise. The seal glass on diffusion couple 1 turned out to be poorly sintered. The melting stage for the next diffusion couples was therefore performed at a higher temperature (1400 °C), which resulted in dense seals. Diffusion couple 3 was the "Flux test sample" described in chapter 8.

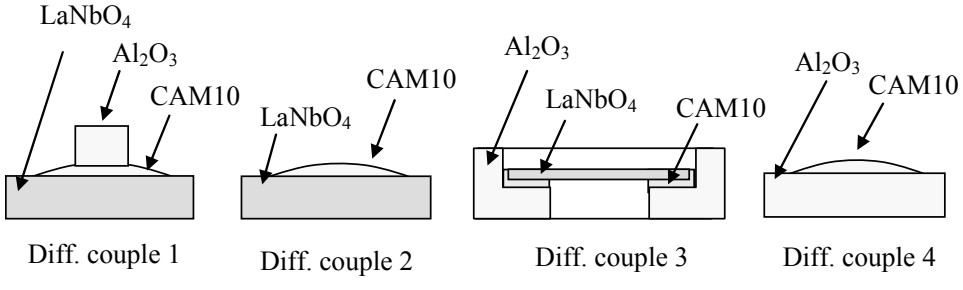

Figure 6.2
Diffusion couples used for studying reactions between the seal glass (CAM10), $LaNbO_4$ and Al_2O_3

Table 6.3 *Heat treatment of diffusion couples*

Diffusion couple	Melting Temp./Hold time (°C/Hours)	Crystallization Temp./Hold time (°C/Hours)
1	1300/2	1100/56
2	1400/1	1300/110
3	1400/1	1060/47 1004/84
4	1400/1	1300/110

6.2.3 Characterization

Powder X-ray diffraction were performed on all the powder mixtures (particle size <45µm) by using a BRUKER diffractometer Focus 8 with Cu-Kα radiation and Lynx-Eye detector. After the final firing EMPA was performed on polished cross sections of the diffusion couples and the sintered powder mixtures using a Jeol JXA-8900 electron microprobe. Backscatter images were taken of the microstructure of all mixtures. For all identified phases at least 3 point analysis were made from three different grains.

6.3 Results

6.3.1 Electron microprobe analysis of CAM10/$LaNbO_4$ mixtures

The microstructure of the sintered powder mixtures showed that the phase distribution was not completely homogeneous. However, the main phases are expected to be close to the equilibrium composition. The composition of the various phases observed by EMPA is summarized in Table 6.4 and the microstructure of the powder samples is shown in Figures 6.3-6.5. The letters in the "Phase ID" column in Table 6.4 correspond to the marked phases in Figures 6.3-6.5. This notation is used for the same phases in the following. $LaNbO_4$ was identified only in samples 30/70 and 50/50.

In the mixture 30/70, $LaNbO_4$ was evenly distributed through the whole sample demonstrating that $LaNbO_4$ is a stable phase for this powder mixture. In the mixture 50/50 the amount of $LaNbO_4$ was considerably lower. $LaNbO_4$ was concentrated in a few large grains (100-150 µm), showing that the mixture had not been completely homogeneous before the final firing. The low $LaNbO_4$ content indicates however that $LaNbO_4$ is nearly completely consumed in the reaction with the glass. For 70/30, $LaNbO_4$ was not detected.

La and/or Nb from $LaNbO_4$ are found in four new phases. The first of these (P6) was present in all three powder mixtures and has a composition close to $Ca_2LaAl_2NbO_9$. This can also be regarded as a double perovskite expressed as; $Ca_{2/3}La_{1/3}Al_{2/3}Nb_{1/3}O_3$. The second phase denoted "$Ca_2Nb_2O_7$" (P2), was present in the mixtures 30/70 and 50/50.

A closer examination of the composition of the "$Ca_2Nb_2O_7$" revealed that this phase also contained small amounts of Mg, Al and La and that Ca+La and Al+Mg+Nb in all cases could be summed up to 20 at. % respectively, giving the general formula $(CaLa)_2(AlMgNb)_2O_6$ for this phase. The third phase $CaLaAl_3O_7$, (P10) was only present in the mixture with 70 wt % CAM10. The fourth phase (P9) denoted β-alumina, was present in the same mixtures as $Ca_2Nb_2O_7$. The β-alumina contains Ca, La and Mg. The microprobe analysis of the β-alumina phase was quite similar in the two mixtures where this phase was identified, giving the nominal composition as: $CaMgLaAl_{17}O_{29}$. The last two phases detected in the powder mixtures were CA_2 (P4) and $MgAl_2O_4$ (P8), which both are stable in the CaO-MgO-Al_2O_3 system. The crystallites in the 50/50 mixture of Al_2O_3 and CAM10 were too small to give reliable composition from EMPA and the composition for this sample is therefore not presented.

Table 6.4
Electron microprobe analysis of the three powder mixtures of CAM10/$LaNbO_4$; 30/70, 50/50 and 70/30

Mixture	Phase ID	Composition at. %						Simplified composition
		Ca	La	Al	Mg	Nb	O	
30/70	P1	0.5	18.6	0.4	0	18.7	61.7	$LaNbO_4$
	P2	11.2	8.9	2	2.1	16.4	59.5	"$Ca_2Nb_2O_7$"
	P6	11	9.7	14.2	0.3	7.1	57.7	$Ca_2LaAl_2Nb_2O_9$
	P9	0.8	2.6	34.3	2.4	0.3	59.5	β-Alumina
50/50	P1	0.3	18.6	0	0	18.6	62.4	$LaNbO_4$
	P2	11.2	8.8	1.6	2.1	16.4	59.9	"$Ca_2Nb_2O_7$"
	P6	13.5	7.8	13.4	0.5	7.3	57.5	$Ca_2LaAl_2NbO_9$
	P8	0.4	0.2	26.9	13.8	0.2	58.5	$MgAl_2O_4$ (spinel)
	P9	1.3	2	34.4	2.1	0.1	60	β-Alumina
70/30	P4	8	0.1	32.6	1.4	0	58	$CaAl_4O_7$ (CA_2)
	P6	14.5	7.3	13.7	0.3	7.3	56.9	$Ca_2LaAl_2NbO_9$
	P10	9.8	6.9	24.9	0.7	0.4	57.4	$CaLaAl_3O_7$

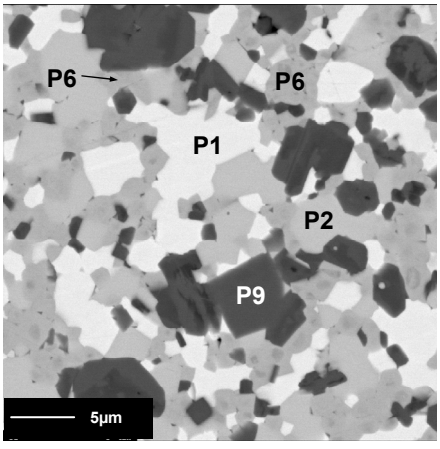

Figure 6.3
Backscatter image of the mixture CAM10/$LaNbO_4$ 30/70 P1: $LaNbO_4$, P2: "$Ca_2Nb_2O_7$", P6: $Ca_2LaAl_2NbO_9$ and P9: β-Alumina

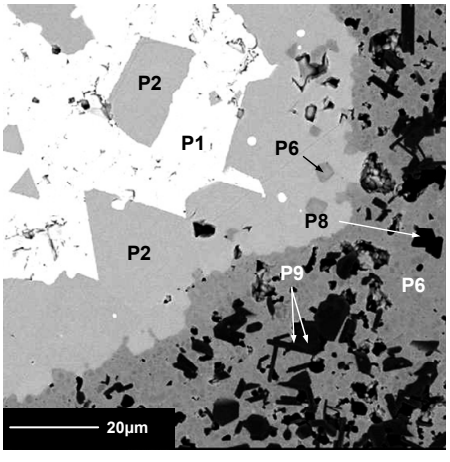

Figure 6.4
Backscatter image of the mixture CAM10/$LaNbO_4$ 50/50. P1: $LaNbO_4$, P2: "$Ca_2Nb_2O_7$", P6: $Ca_2LaAl_2NbO_9$, P8: $MgAl_2O_4$ (Spinel), P9: β-alumina

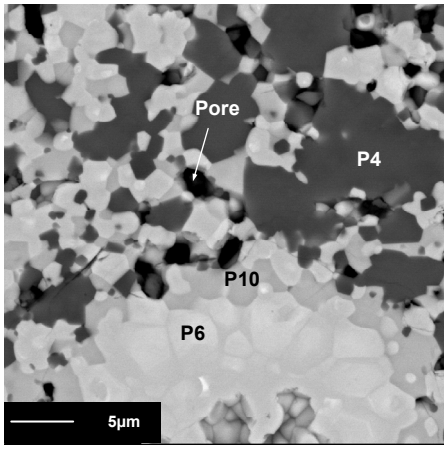

Figure 6.5
Backscatter image of th mixture CAM10/$LaNbO_4$ 70/30. P4: $CaAl_4O_7$ (CA_2), P6: $Ca_2LaAl_2NbO_9$, P10: $CaLaAl_3O_7$,

6.3.2 X-ray diffraction of powder mixtures

Three heat treatments were necessary to achieve equilibrium in the powder mixtures. This is demonstrated by the XRD patterns of CAM10/LN 50/50 powder mixture shown in Figure 6.6. The presence of $LaNbO_4$ was evident after the first and second heat treatment, while after the third heating cycle (92 h) only trace amount of $LaNbO_4$ was observed. This observation is consistent with the microscopy results and illustrates that the $LaNbO_4$ and devitrified glass are not coexistent. The opposite is the case with β-alumina and spinel, which become more abundant with increased heating time. The phase CA was present after 30 h while CA_2 was present in the first two heat treatments. These observations are summarized in Table 6.5.

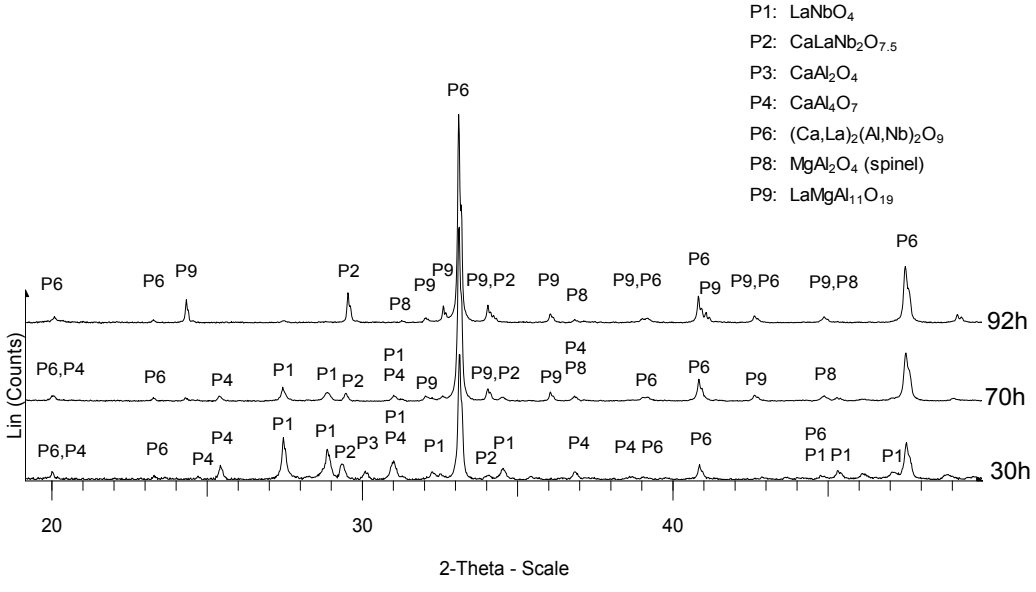

Figure 6.6
XRD -pattern of powder mixture 50/50 wt% CAM10/$LaNbO_4$ after 30, 70 and 92h

Table 6.5
Phase development of mixture CAM10/$LaNbO_4$ 50/50 versus increased heating time. "x" means phase identified, "-" means trace amounts.

Phase ID	Phase	1300 °C 30 h	1300 °C 70 h	1375 °C 92 h
P1	$LaNbO_4$	x	-	
P2	$CaLaNb_2O_{7.5}$	x	x	x
P3	$CaAl_2O_4$	x		
P4	$CaAl_4O_7$	x	x	
P6	$Ca_2LaAl_2NbO_9$	x	x	x
P8	$MgAl_2O_4$ (spinel)		x	x
P9	$LaMgAl_{11}O_{19}$			x

The identified phases and the corresponding PDF-files [135] after the final heat treatment of the powder mixtures are given in Table 6.6 while the corresponding X-ray diffraction patterns are shown in Figure 6.7. Table 6.6 also includes the crystalline phases in devitrified CAM10 glass that were reported in chapter 4.

The phases identified in the 50/50 CAM10/Al_2O_3 mixture were all in accordance to the phase diagram in Figure 4.8. Regarding the mixtures of CAM10 and $LaNbO_4$ all except one phase correspond to the phases that were identified by EMPA. The exception is the spinel phase that was identified only in mixture 50/50 while the X-ray analysis shows that spinel is also present in mixture 70/30.

Table 6.6
Crystalline phases identified in the pure seal glass CAM10 and in the powder mixtures. The PDF-file numbers are from [135]

CAM10/$LaNbO_4$ (wt%)	Phases identified by XRD	Phase ID	PDF number [135]
CAM10	$CaAl_2O_4$ (CA)	P9	01-070-0134
	$Ca_3MgAl_4O_{10}$ (C_3MA_2)	P13	00-017-0737
	$Ca_{12}Al_{14}O_{33}$ ($C_{12}A_7$)	P15	00-009-0413
CAM10/Al_2O_3 50/50	$CaAl_2O_4$ (CA)	P9	01-070-0134
	$MgAl_2O_4$ (Spinel)	P12	00-021-1152
	$CaAl_4O_7$ (CA_2)	P14	00-023-1037
CAM10/$LaNbO_4$ 30/70	"$Ca_2Nb_2O_7$"	P7	01-081-0841
	$LaNbO_4$	P1	01-071-1405
	$LaMgAl_{11}O_{19}$ (β-alumina)	P8	00-026-0873
	$Ca_2LaAl_2NbO_9$	P6	[139]
CAM10/$LaNbO_4$ 50/50	"$Ca_2Nb_2O_7$"	P7	01-081-0841
	$LaNbO_4$ (traces)	P1	01-071-1405
	$LaMgAl_{11}O_{19}$ (β-alumina)	P8	00-026-0873
	$Ca_2LaAl_2NbO_9$	P6	[139]
	$MgAl_2O_4$ (spinel)	P12	00-021-1152
CAM10/$LaNbO_4$ 70/30	$CaLaAl_3O_7$	P16	01-081-1797
	$CaAl_4O_7$ (CA_2)	P14	00-023-1037
	$Ca_2LaAl_2NbO_9$	P6	[139]
	$MgAl_2O_4$ (Spinel)	P12	00-021-1152

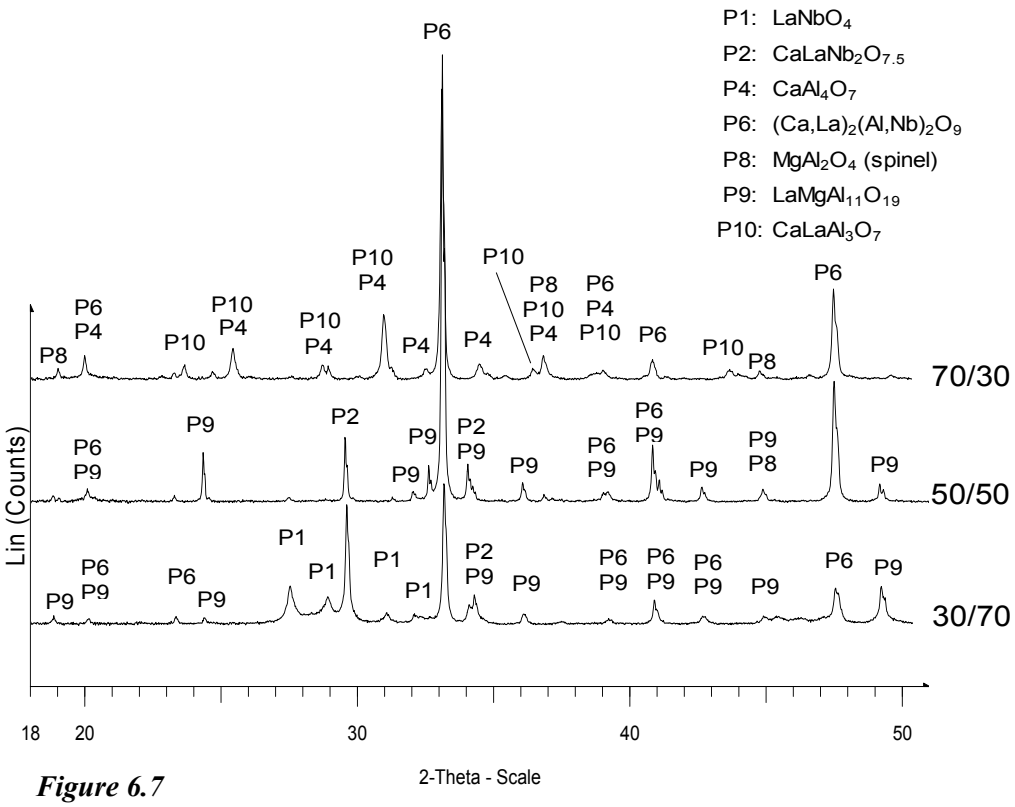

Figure 6.7
X-ray diffraction patterns of the three powder mixtures after the final heat treatment (see Table 6.2)

The phase $LaMgAl_{11}O_{19}$ (hexagonal structure), which was present in the 50/50 and 30/70 mixtures, corresponds to the β-alumina (P9) identified in the same samples by EMPA. The phase $Ca_2LaAl_2NbO_9$ (P6) was present in all mixtures. The X-ray diffraction pattern for this compound is similar to the pattern reported for Ca_2AlNbO_6, which was indexed by Vanderah et al. [139] based on a monoclinic perovskite with unit cell ($P2_{1/n}$). In the present work, the composition is proven to be $Ca_2LaAl_2NbO_9$. The phase denoted "$Ca_2Nb_2O_7$" corresponds to $CaLaNb_2O_7$, which is reported in PDF file 1-081-0841 [135]. To maintain the charge balance of this compound there should be 7.5 oxygen atoms and not 7 as reported. According to Lewandowski et al. [141] $CaLaNb_2O_7$ possesses a cubic pyrochlore structure (pyrochlore; $A_2B_2O_7$). On the other hand the phase $Ca_2Nb_2O_7$, which is described in many papers [139-141] possesses according to [141], a pyrochlore structure below 650 °C and a perovskite structure above 650 °C.

6.3.3 Diffusion couples

6.3.3.1 Diffusion couple 1 -2 h/1300 ˚C + 5 h/1100 ˚C

The microstructure of diffusion couple 1 showed that the CAM10 coating was porous demonstrating that the temperature during sealing was too low. However, a promising physical contact between $LaNbO_4$ and the glass had been formed as shown in Figure 6.8. (Due to the poor densification only the interface between $LaNbO_4$ and CAM10 glass was analysed in this sample. The reaction between alumina and seal glass was studied on diffusion couple 4). The main phase in the reaction zone between the glass and $LaNbO_4$ was identified to be "$Ca_2Nb_2O_7$" (P2). Also present in the same region was the phase $CaAlNbO_5$ (P15). The elemental analysis shows that P2 also contains 2 % Mg and 2 % Al. In the CAM10 matrix close to the reaction zone, a scattered light grey phase formed as "fingers" was observed.

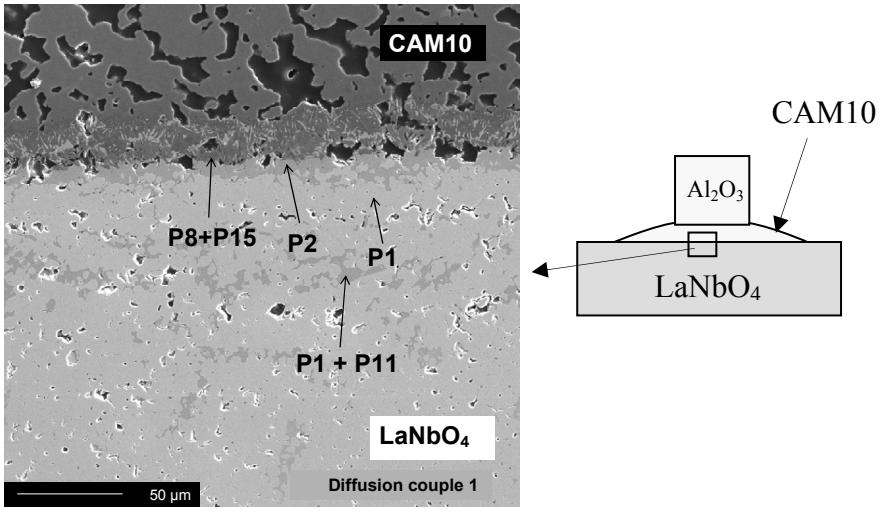

Figure 6.8
Backscatter image of the microstructure of the reaction zone between CAM10-glass and sintered $LaNbO_4$.in diffusion couple 1. The sample was fired for 2 h at 1300 °C and for 56 h at 1100°C. P1: $LaNbO_4$, P2: "$Ca_2Nb_2O_7$", P8: $MgAl_2O_4$,, P11: $CaLa_6Nb_8O_{30}$,P15: $CaAlNbO_5$. See Table 6.7 for elemental composition

The "fingers" were composed of at least two phases with nominal composition $Ca_{10}Al_6Nb_4Si_3O_{29}$ and $Mg_5Ca_7Nb_2Al_{20}Si_4O_{51}$, respectively. These phases contained Si-impurities from an unknown source and will not be discussed any further. In $LaNbO_4$, two phases were observed, distinguished by different grey colour. The lightest was as expected $LaNbO_4$. The other (P11) was essentially $LaNbO_4$ but this phase also

contained 2.2 at% Ca. The elemental composition of the phases is summarized in Table 6.7.

Table 6.7
Electron microprobe analysis of diffusion couple 1.The phase corresponding to the analysed points is shown in Figure 6.8

Phase	Composition (at.%)							
ID	Ca	La	Al	Mg	Nb	O	Sum	"Compound"
P1	0.6	18.7	0.2	0.1	19.7	60.9	100.0	$LaNbO_4$
P2	20.6	2.1	2.3	0.3	21.3	52.7	100.0	$Ca_2Nb_2O_7$
P8	3.9	0.3	22.8	9.1	2.6	59.8	99.9	$MgAl_2O_4$
P11	2.2	13.4	0.0		18.4	65.9	99.9	$CaLa_6Nb_8O_{30}$
P15	11.5	1.2	9.7	0.7	10.6	65.0	99.9	$CaAlNbO_5$

6.3.3.2 Diffusion couple 2

The microstructure of the diffusion couple CAM10/$LaNbO_4$ heat treated for 110 h at 1300˚C reveals a distinct reaction zone between the glass and $LaNbO_4$ as shown in Figure 6.9. This reaction is promising with respect to using CAM-type glasses as sealing material for $LaNbO_4$. Some cracks have developed perpendicular to the interface but have not propagated into the CAM10-matrix.

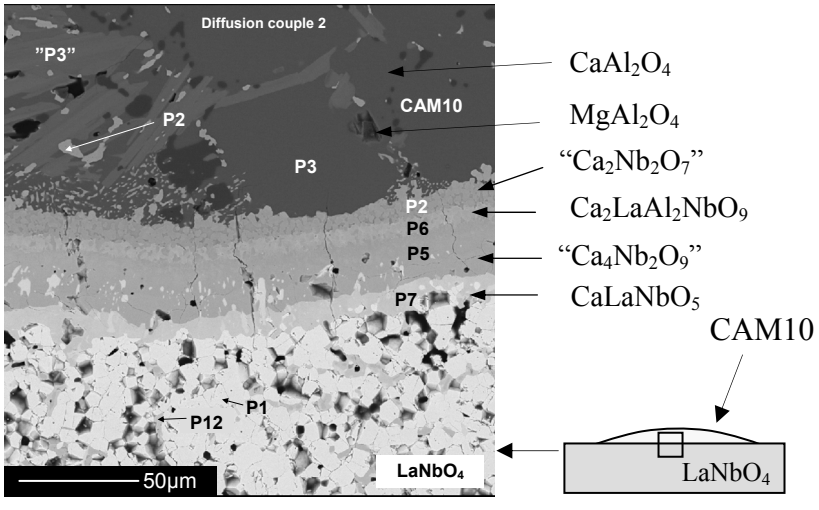

Figure 6.9
Backscatter image of reaction zone between CAM10 and $LaNbO_4$ in diffusion couple 2 heated for 110 h at 1300 °C. See Table 6.8 for phase identification

The reaction zone is more complex in diffusion couple 2 compared to diffusion couple 1. Four different reaction layers can be distinguished by different grey colours in Fig. 6.9. Closest to $LaNbO_4$ is a phase (P7) with the simplified composition $CaLaNbO_5$. Then follow a ~ 20 µm wide layer consisting of a phase (P5) with the simplified composition "$Ca_4Nb_2O_9$". This phase is proposed to be related to the compound $Ca_4Nb_2O_9$, which is a polymorphic ordered perovskite [139,142]. The next layer is composed mainly of the phase P6 with the simplified composition $Ca_2LaAl_2NbO_9$ corresponding to the "double perovskite" described in chapter 6.3.1. Finally, closest to CAM10, is a layer (P2) of "$Ca_2Nb_2O_7$", which can be given the more general composition $(CaLa)_2(AlMgNb)_2O_6$ as in the powder mixtures. In the devitrified glass the main phase close to the reaction border is $CaAl_2O_4$ (P3). A similar phase (denoted "P3"in Figure 6.9) occurs as grey elongated crystals. The nominal composition was $Mg_{0.1}La_{0.1}Ca_{1.2}Al_{2.0}O_{4.5}$, which essentially is the same as P3 ($CaAl_2O_4$). The elemental composition of the analysed phases is given in Table 6.8.

Table 6.8
EMPA of phases in the reaction zone between CAM10 glass and $LaNbO_4$ of diffusion couple 2 after 110h at 1300˚C. The analysed phases are illustrated in Figure 6.9

Phase ID	Composition (at. %)						Simplified composition
	Ca	La	Al	Mg	Nb	O	
P1	0.1	16.7	0.2	0.0	15.7	67.2	$LaNbO_4$
P2	17.4	2.0	8.4	2.1	8.3	61.9	"$Ca_2Nb_2O_7$"
P3	13.7	0.6	24.7	0.9	0.0	60.1	$CaAl_2O_4$ (CA)
P5	20.3	3.7	0.3	2.4	10.9	62.3	$Ca_4Nb_2O_9$
P6	12.5	6.7	13.3	0.3	5.9	61.3	$Ca_2LaAl_2NbO_9$
P7	11.0	9.6	0.4	0.6	13.7	64.7	$CaLaNbO_5$
P12	12.5	3.3	0.5	0.3	16.2	67.1	$Ca_4LaNb_5O_{18}$

6.3.3.3 Diffusion couple 3 - flux test sample

Diffusion couple 3 demonstrates the good seal towards $LaNbO_4$ as shown in the backscatter image in Figure 6.10. The results of the microprobe analysis are given in Table 6.9. A distinct reaction zone is also evident in this diffusion couple. The reaction zone is composed of two main layers. Closest to $LaNbO_4$ is a narrow more or less continuous belt of a phase with the simplified composition $CaLaNbO_5$ (P7) analogous to what was observed in diffusion couple 2. Then follows a continuous belt ~ 12-15 µm wide (P5), of the phase "$Ca_4Nb_2O_9$". The next layer (P2) is recognized as "$Ca_2Nb_2O_7$".

Both P2 and P5 are analogous to what was found in diffusion couple 2 (Figure 6.9). The distribution of P2 in diffusion couple 3 looks like ice flakes that are braking loose contrary to diffusion couple 2 where the corresponding layer was more continuous. This difference reflects the different thermal history of the two samples. The main phases identified in the CAM10 glass close to the $LaNbO_4$ interface, are $MgAlO_4$ (P8) and $CaAl_2O_4$ (P3). Also in this sample the phase "P3" was present, which essentially had the composition CA but with small amounts of Mg and La.

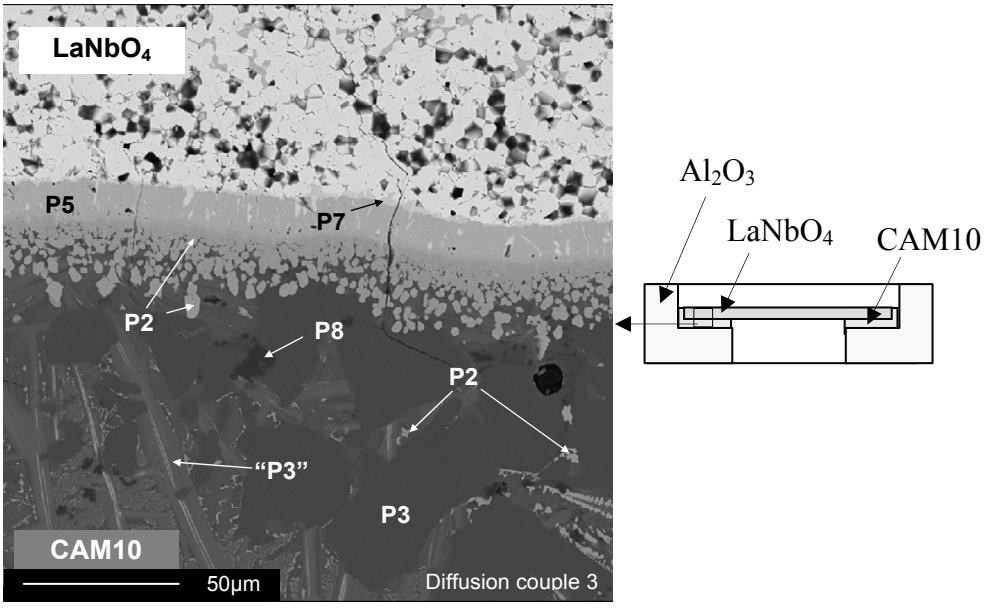

Figure 6.10
Backscatter image of the reaction border between$LaNbO_4$ and CAM10 glass in diffusion couple 3 -flux test sample that was heated 1400 °C/1 h, 1060 °C/4 7h, 1004 °C/84 h. See Table 6.9 for phase identification

Table 6.9
Electron microprobe analysis of diffusion couple 3, focusing on the reaction between CAM glass with 10 mol % MgO and $LaNbO_4$ after seal performance testing. The heat treatment is given in Table 6.3

Phase	Composition (at. %)						Simplified
ID	Ca	La	Al	Mg	Nb	O	composition
P2	15.4	3.9	11.1	1.8	6.5	61.3	"$Ca_2Nb_2O_7$"
P3	13.1	0.1	26.3	0.1	0.0	60.4	$CaAl_2O_4$ (CA)
P5	19.3	5.7	0.3	2.1	10.3	62.3	$Ca_4Nb_2O_9$
P7	11.8	10.0	0.5	0.8	12.3	64.3	$CaLaNbO_5$
P8	0.3	0.0	25.6	12.5	0.0	61.6	$MgAl_2O_4$ (spinel)

6.3.3.4 Reactions between Al_2O_3 and CAM10 in diffusion couple 4

The phases observed in the reaction layer between sintered alumina and devitrified CAM10 glass, are shown in Figure 6.11. First of all there is a good physical contact between the glass and alumina, which demonstrates that CAM10 is a perfect seal for alumina. The primary reaction layer consists only of the crystalline phase CA_2 (P4 in Figure 6.11). All other phases that were identified; C_3MA_2 (P13), $C_{12}A_7$ (P14) and CA (P3) are in accordance with the phase diagram presented in Figure 4.9. The phase marked Cont. contained ZrO_2, probably from the zirconia lining in the furnace. The results of the microprobe analysis are given in Table 6.10. Some fractures are observed in the glass matrix especially in the C_3MA_2 region but not across the primary reaction zone.

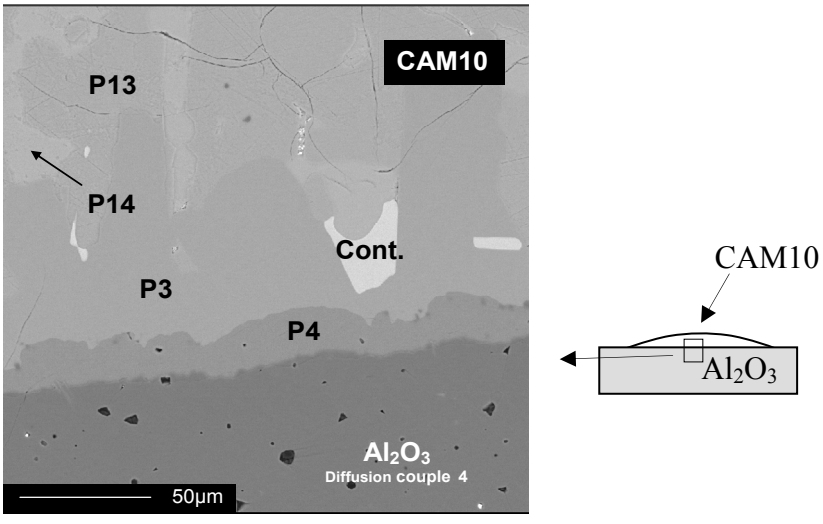

Figure 6.11
Backscatter image of reaction zone between devitrified CAM10 glass and alumina in diffusion couple 4 after 11 0h at 1300 °C. See table 6.10 for phase identification. The phase denoted Cont. is a contamination probably caused by zirconia from the furnace lining

Table 6.10
Electron microprobe analysis of phases present diffusion couple 4 due to reaction between devitrified CAM10 glass and sintered alumina

Phase ID	Composition (at. %)				Phase Composition
	Mg	Ca	Al	O	
P3	0.0	13.1	26.2	60.6	$CaAl_2O_3$ (CA)
P4	0.2	7.6	30.8	61.3	$CaAl_4O_7$ (CA_2)
P13	4.8	15.3	20.6	59.3	$Ca_3MgAl_4O_{10}$ (C_3MA_2)
P14	0.5	18.4	21.2	59.9	$Ca_{12}Al_{14}O_{33}$ ($C_{12}A_7$)

6.4 Discussion

6.4.1 Phase relations in powder mixtures

The system MgO-CaO-La_2O_3-Al_2O_3-Nb_2O_5 is a 5 component system when the oxidation state of all the elements is constant. At constant pressure and temperature a maximum of 5 condensed phases are present at equilibrium. The number of phases observed in the powder mixtures is therefore in accordance with the Gibbs phase rule.

The results from XRD and EMPA are consistent regarding the identified crystalline phases demonstrating that the heat treatment has resulted in microstructures that are close to chemical equilibrium. The phase denoted $Ca_2LaAl_2NbO_9$ with perovskite structure is present in all mixtures. Ca and La are located on the A-site while Al and Nb on the B-site in the perovskite ABO_3 lattice. The microprobe analysis indicate that in the mixture (30/70) with 70 wt% $LaNbO_4$ the ratio Ca/La=1, Al/Nb=2 and Al/Ca=4/3 giving the composition $Ca_{1/2}La_{1/2}Al_{2/3}Nb_{1/3}O_{3.08}$. In the 50/50 and 70/30 mixtures the ratio Ca/La=Al/Nb=2 and Ca/Al=1.0, giving the composition $Ca_{2/3}La_{1/3}Al_{2/3}Nb_{1/3}O_3$. This is considered as a stable phase in the quaternary system CaO-Al_2O_3-La_2O_3-Nb_2O_5. The compositions of the β-alumina phases (Table 6.4) were consistent with the XRD analysis given in Table 6.6. According to EMPA the β-alumina could be expressed as $CaMg_2La_2Al_{34}O_{60}$ where the ratio Mg/La =1.0. By dividing by 3 the composition becomes close to $MgLaAl_{11}O_{19}$, which is the compound identified by XRD. On this basis it is reasonable to state that the β-alumina in the present work is $MgLaAl_{11}O_{19}$. The phases present were determined by the overall composition of the actual powder mixture. As $LaNbO_4$ is consumed La and Nb enter new phases together with the glass components. This is illustrated in Figure 6.12 where the relative intensities of the strongest diffraction lines of the phases are plotted versus CAM10/$LaNbO_4$ fraction.

The phase $CaLaNb_2O_{7.5}$ appears with $Ca_2LaAl_2NbO_9$ ($Ca_{2/3}La_{1/3}Al_{2/3}Nb_{1/3}O_3$) and β-alumina, and these three phases are all present in both 30/70 and 50/50 mixtures. At excess glass content, $CaLaNb_2O_{7.5}$ disappears and the phase $CaLaAl_3O_7$ is formed. To summarize, the experimental observations can be explained by the following reactions:

30/70: CAM10+$LaNbO_4$ →

$$MgLaAl_{11}O_{19} + CaLaNb_2O_{7.5} + Ca_{1/2}La_{1/2}Al_{2/3}Nb_{1/3}O_{3.08} \quad 6.1$$

50/50: CAM10+$LaNbO_4$ →

$$MgLaAl_{11}O_{19} + CaLaNb_2O_{7.5} + Ca_{2/3}La_{1/3}Al_{2/3}Nb_{1/3}O_{3.} + MgAl_2O_4 \quad 6.2$$

70/30: CAM10+$LaNbO_4$ →

$$CaLaAl_3O_7 + Ca_{2/3}La_{1/3}Al_{2/3}Nb_{1/3}O_3 + CaAl_2O_4 + MgAl_2O_4 \quad 6.3$$

The phases formed in the sintered 50/50 wt% Al_2O_3/CAM10 powder mixture identified by the XRD analysis (Table 6.6), can be accounted for by the following reaction:

$$Ca_6MgAl_{8.6}O_{19.9} + 8Al_2O_3 = 0.7CaAl_2O_4 + 5.3CaAl_4O_7 + MgAl_2O_4 \quad 6.4$$

The main phase is $CaAl_4O_7$ (CA_2) amounting to 84 weight % of the total.

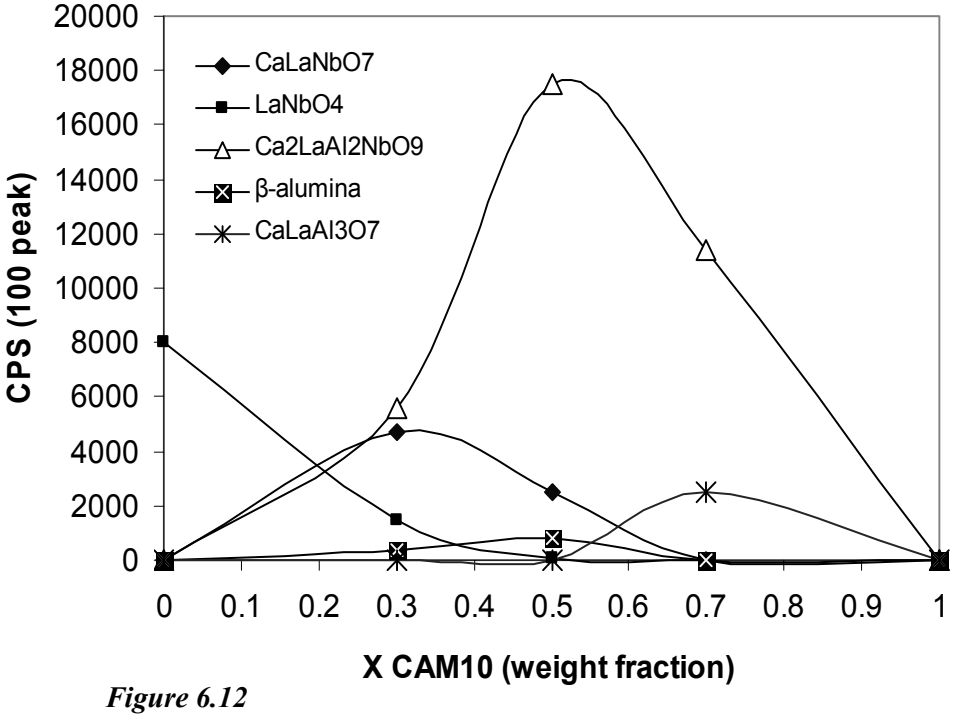

Figure 6.12
Changes in phase composition of powder mixtures with increasing content of CAM10 glass relative to $LaNbO_4$

6.4.2 Reaction mechanisms

The three diffusion couples in Figures 6.8-6.10 give information of how the reaction between CAM10 and $LaNbO_4$ proceeds. The early stage is demonstrated by diffusion couple 1. The first of the secondary phases formed in the reaction zone are apparently (simplified compositions) "$Ca_2Nb_2O_7$" (P2) and $CaAlNbO_5$ (P15). The next stage is demonstrated by diffusion couple 3 where the phase in intimate contact with $LaNbO_4$ is

$CaLaNbO_5$ (P7, Figure 6.10). The next phase (P5) can be expressed as"$Ca_4Nb_2O_9$" followed by the phase (P2) "$Ca_2Nb_2O_7$". The "final" stage in the reaction development is represented by diffusion couple 2. The phases present in this sample are the same as were present in diffusion couple 3. $CaLaNbO_5$ (P7) and "$Ca_4Nb_2O_9$" (P5) are present close to the initial interface between the glass and $LaNbO_4$. Then follow the double perovskite $(Ca_2La)(Al_2Nb)O_9$ and finally in direct contact with CAM10, "$Ca_2Nb_2O_7$". From these observations it seems that "$Ca_2Nb_2O_7$" is an intermediate phase making up the reaction front in direct contact with CAM10. Behind this phase is the stable double perovskite $(Ca_2La)(Al_2Nb)O_9$. Another phase that is present in diffusion couples 2 and 3 is $Ca_4Mg_{0.5}LaNb_2O_{11}$ denoted "$Ca_4Nb_2O_9$", which appears together with $CaLaNbO_5$ and $Ca_2LaAl_2NbO_9$. It is not clear if $Ca_4Nb_2O_9$ is a stable phase or if it is an intermediate phase. According to Levin et al. [142] $Ca_4Nb_2O_9$ has four perovskite -related polymorphs, two above 1400 °C and two below 1400 °C.

The reaction mechanism at the interface is governed by diffusion of the cations in the two materials. As illustrated in Figure 6.13, La and Nb are diffusing into the glass while the components in the glass are diffusing in the opposite direction. Since the initial interface was not marked with an inert marker (e.g. Pt) it is not possible to conclude regarding the most mobile metal ions. Nb seems to be more mobile than La since Nb can be found in the phase towards the glass. Ca and Al were found in the phase next to $LaNbO_4$ showing that these two elements are diffusing across the reaction zone.

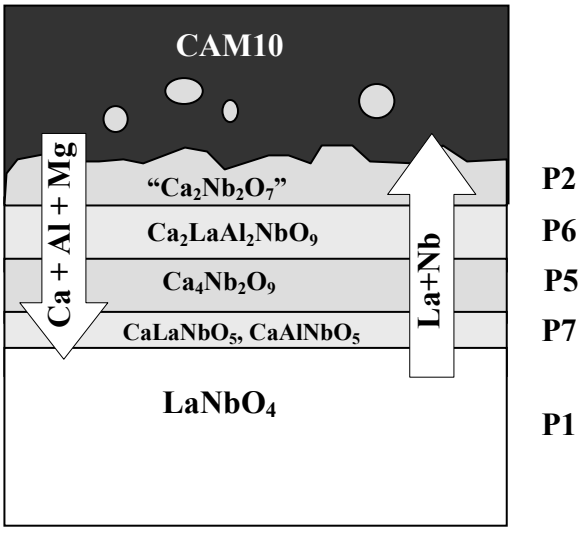

Figure 6.13
Simplified sketch of the elemental diffusion and phases in the reaction zone between $LaNbO_4$ and CAM10 glass for diffusion couple 3

6.4.3 Sealing properties

The diffusion couples demonstrate clearly that the CAM10-glass forms a very tight and solid bond to $LaNbO_4$. This is important in order to achieve a seal that performs well during operation of the device. Some fractures were observed across the reaction zone in diffusion couples 2 and 3 (Figures 6.9 and 6.10). The fractures are an indication of thermal expansion mismatch between the secondary phases and the joined materials. It is important that the thermal expansion coefficient of all secondary phases matches that of the pure crystallised glass and that of the $LaNbO_4$ membrane. The direction of the cracks, perpendicular to the membrane, indicates that the phases within the reaction zone have a higher thermal expansion than the CAM10 glass and $LaNbO_4$. The TEC of the secondary phases has to be known to figure out if the cracking is caused by the thermal expansion mismatch, or if the heating cycle during sealing has any influence. The sealing procedure can be further optimized by changing the sealing temperature, the holding time at the sealing temperature, and finally the holding time for crystallization of the glass. It is of particular importance to reduce the time at the highest temperature (sealing stage) to avoid extended reaction at the interface.

7 Reactions between La-Ba-silicate glass (BLS) and La_2NiO_4

7.1 Introduction

A Ba-La-silicate glass (BLS) originally developed and patented [50] as seal material for La_2NiO_4 HT membrane reactors has been prepared. The thermal properties of the BLS glass were studied by means of DSC-analyses and dilatometry. The chemical compatibility of BLS with La_2NiO_4 has been studied by evaluating the microstructure and phase composition of sintered powder mixtures while reaction mechanisms and seal performance were studied on two different types of diffusion couples.

7.2 Experimental

7.2.1 Preparation of BLS glass

A barium-lanthanum silicate glass (BLS) with the composition $Ba_{11.1}La_{4.6}Si_{22.0}O_{62.2}$ (molar composition $31.4BaO{\cdot}6.5La_2O_3{\cdot}62.1SiO_2$) was prepared from $BaCO_3$, La_2O_3 and SiO_2 following the same procedure as described in chapter 4.2.1. The quenched glass was crushed and wet milled in a planetary mill (Retsch PM100) using isopropanol as liquid, alumina grinding balls and a grinding jar lined with alumina. After milling, the powder was dried in vacuum by use of a "Rotavapor". A fraction of particles with diameter <45 μm was separated from the powder batch by sieving. The rest of the powder was remilled to particle size d_{90}<32 μm for the preparation of the powder mixtures. A coarse fraction of glass particles in the range 45-150 μm was separated from the crushed glass for use in DSC-measurements.

7.2.2 Preparation of powder mixtures

Mixtures of BLS glass powder and La_2NiO_4 powder made by spray pyrolysis (chapter 5.1.2) were prepared in weight ratios BLS/La_2NiO_4 of: 30/70, 50/50 and 70/30. The calculated elemental composition of these mixtures and the BLS glass is given in Table 7.1. The BLS/La_2NiO_4 powder mixtures were mixed in an agate mortar, pressed to tablets with diameter 10-15 mm at 100 MPa and heat treated according to Table 7.2. After each heat treatment the samples were milled to particle size < 45 μm and repressed to tablets following the flow sheet presented in Figure 6.1.

The BLS/La_2NiO_4 powder mixtures prepared for EMPA were fabricated in the same way as described for the XRD samples using the powder fraction with d_{90}<32 μm. The heat treatment was performed according to Table 7.3.

Table 7.1
Calculated elemental composition of BLS glass and powder mixtures of BLS and La_2NiO_4

Material mixture	Mixture (wt. %)	Composition (at. %)				
		Ba	Si	La	Ni	O
BLS	100.0	11.1	22.0	4.6		62.2
BLS/La_2NiO_4	30/70	4.4	8.7	19.2	8.7	59.1
BLS/La_2NiO_4	50/50	6.7	13.3	14.2	5.7	61.1
BLS/La_2NiO_4	70/30	8.7	17.2	9.9	3.2	60.8

Table 7.2 *Heat treatment of BLS/La_2NiO_4 powder samples*

Cycle no.	Temp. (°C)	Time (h)	BLS	BLS/La_2NiO_4 mixture		
				30/70	50/50	70/30
1	1230	30	x			
2	1300	24		x	x	x
3	1250	40				x
4	1300	20		x	x	x
5	1200	86		x	x	x

Table 7.3
Heat treatment of BLS glass fracture, BLS/La_2NiO_4 powder mixtures and $Ba_2La_2Si_4O_{13}$ prepared for EMPA.

Mixture	Temperature (°C)	Time (h)
BLS (Glass fracture)	1000	72
	1200	60
BLS/LN 30/70	1240	50
	1300	50
	1350	100
	1400	50
BLS/LN 50/50	1240	50
	1250	50
	1280	70.4
	1300	50
	1350	100
BLS/LN 70/30	1240	50
	1250	50
	1280	70.4
$Ba_2La_2Si_4O_{13}$	After cycle 4 in Table 7.2	

The BLS sample prepared for electron microprobe analysis was a glass fracture crystallised in a heating cycle with holding time 72 h at 1000 °C followed by 60 h at 1200 °C. XRD analyzes of the milled BLS powder showed traces of alumina. "Quantitative" XRD analysis of the powder added 1.11 and 2.97 wt % alumina, respectively, showed that the contaminated powder contained ~0.5 wt. % alumina. This amount is so small that is has no importance regarding the reaction mechanisms and the main conclusions, but as will be seen later aluminium was identified in the EMPA analyses.

7.2.3 Preparation of $Ba_2La_2Si_4O_{13}$ and $Ba_2La_8Si_6O_{26}$

Two of the crystalline phases; $Ba_2La_2Si_4O_{13}$ and $Ba_2La_8Si_6O_{26}$ respectively that were formed during the reaction between BLS and La_2NiO_4 will be described in chapter 7.3.2. Since these two phases turned out to be of great importance in the seal development they were synthesized from SiO_2, $BaCO_3$ and La_2O_3 powders and evaluated with respect to elemental composition (EMPA), structure (XRD) and thermal expansion. The production process followed the same route as for the powder mixtures (Chap. 7.2.2), but the raw materials were mixed by gentle ball milling for 18 h in polyethylene bottles with alumina balls (ø 4 mm) and isopropanol as liquid. The dried powder mixtures were pressed into tablets with diameter 10 mm by uniaxial pressing. The $Ba_2La_2Si_4O_{13}$ was heat treated 4 times while $Ba_2La_8Si_6O_{26}$ was heat treated 2 times according to Table 7.4.

Table 7.4
Heat treatment of $Ba_2La_2Si_4O_{13}$ and $Ba_2La_8Si_6O_{26}$

Cycle	Temperature (°C)	Holding time (h)	$Ba_2La_2Si_4O_{13}$	$Ba_2La_8Si_6O_{26}$
1	1200	50	x	x
2	1350	36	x	x
3	1350	60	x	
4	1400	40	x	

7.2.4 Preparation of diffusion couples

Two diffusion couples of the system BLS -La_2NiO_4 were prepared. The first sample (Figure 7.1) was made by dripping a mixture of BLS glass powder (<45 μm particle diameter) and distilled water added polyvinyl alcohol

(PVA) binder on top of a polished plate of sintered La_2NiO_4. After drying at room temperature for 2 hours, the assembly was fired in air at 1300 °C for 30 h.

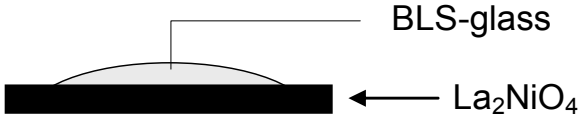

Figure 7.1
Diffusion couple 1. BLS glass powder (-45µm particle diameter) on top of polished and sintered La_2NiO_4 membrane. Heat treated in air 30h at 1300 ˚C

A polished cross section of the sample was analysed for reaction between the two materials. The second diffusion couple consisted of three parts: La_2NiO_4 support, the BLS seal and the La_2NiO_4 membrane as illustrated in Figure 7.2. A detailed description of the preparation is given i chapter 8. The seal was established by heating the sample for 2 hours at 1300 °C and crystallised at 1050 °C for 5 hours. Before the electron microprobe analysis was performed diffusion couple 2 was used for leakage testing of the seal (see Chapter 8). In this test the sample was exposed to temperatures above 900 ˚C for 263 hours (55 h at 1062 ˚C, 94 h at 1002 ˚C and finally 106 h at 904 ˚C + heating and cooling ramps).

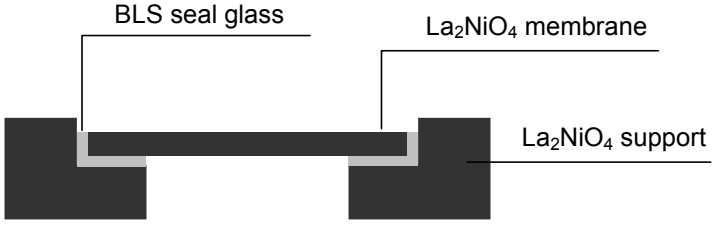

Figure 7.2
Cross section of diffusion couple 2 (flux test sample) that consisted of La_2NiO_4 substrate, BLS seal glass (d<45µm) and La_2NiO_4 membrane. The seal was established by heating 2 hours at 1300 °C followed by crystallization at 1050 °C for 5 hours

7.2.5 Preparation of samples for thermal expansion measurement

Small bars of BLS glass were prepared by uniaxial pressing of powder with particle size < 45 µm. The bars were sintered at 800 °C for 1 h and the heating and cooling rates were 100 and 200 °C/h, respectively. Thermal

expansion of $Ba_2La_8Si_6O_{26}$ was performed on a sample that was heat treated twice (1230 °C/30 h + 1300 °C/24 h). Thermal expansion of $Ba_2La_2Si_4O_{13}$ was performed on a bar (10x10x56 mm) that was pressed from the powder from heat treatment cycle 4 (Table 7.4). The bar was sintered in two steps: 50 h at 1250 °C followed by 50 h at 1300 °C respectively, prior to the thermal expansion measurements.

7.2.6 Characterisation

Powder XRD analysis and EMPA were performed to characterize the fired samples. The samples for XRD studies were milled to particle size < 45 μm by using a Retsch Mixermill. The XRD analysis were performed as described in chapter 6.2.3. Refinement of X-ray patterns were performed using the program "Topas" [144]. XRD of BLS and the BLS/La_2NiO_4 powder mixtures were performed after each heat treatment given in Table 7.2. Regarding $Ba_2La_2Si_4O_{13}$ and $Ba_2La_8Si_6O_{26}$, XRD was performed after each heat treatment given in Table 7.4.

EMPA was performed on polished cross sections of the sintered samples using a Jeol JXA-8900. Backscatter images were recorded of all samples and point analysis were made on 3 different grains of each identified phase. The samples of BLS glass fracture and sintered powder mixtures were prepared after the final heat treatment given in Table 7.3. EMPA of $Ba_2La_2Si_4O_{13}$ was performed on a polished cross section of a sintered sample after heat treatment cycle 4 (Table 7.4). Particle size analysis were obtained either by sieving or by use of a Malvern 2000 Mastersizer with samples dispersed in water.

DSC analysis was performed on crushed fractions of BLS glass with particle size in the range of 45-150 μm. The dilatometric analysis of BLS glass was performed 3 times. The first heating cycle had a maximum temperature of 1024 °C while the two last cycles were run up to ~ 1170 °C. The instruments and measurement procedures for DSC and dilatometry were the same as described in chapter 4.2.2 and 4.2.4.

7.3 Results

7.3.1 DSC analysis of BLS glass

The results of the DSC analysis are given in Table 7.5. The DSC analysis demonstrated that the onset of the glass transition appears at 760 °C and the end appears at 779 °C. The BLS glass started to crystallise at 924 °C and has a crystallization peak T_p at 966 °C.

Table 7.5
Results from DSC and dilatometric analysis of BLS glass

Comment	Temp ID	DSC (°C)	Dil (°C)
Glass transition onset	T_g	760	747
Glass transition end	$T_{g'}$	779	
Softening point	T_s		856
Crystallisation onset	T_x	924	926
Crystallisation peak	T_p	966	

7.3.2 Thermal expansion of BLS glass

The thermal expansion measurements of BLS showed that in the first cycle, while the sample still was amorphous, the expansion curve followed a classical expansion pattern for glass as shown in Figure 7.3 by the bold curve. The expansion was linear until the temperature entered the glass transition region. Here the expansion curve became steeper before it reached the maximum expansion at the dilatometric softening point. By further temperature rise, the sample partly sintered and partly deformed by the pressure from the dilatometer push rod, until the glass started to crystallise at 926 °C. As soon as the crystallization process started a stiffening of the sample occurred, followed by new expansion during the further heating. After 3 cycles in the dilatometer the thermal expansion curve became stable

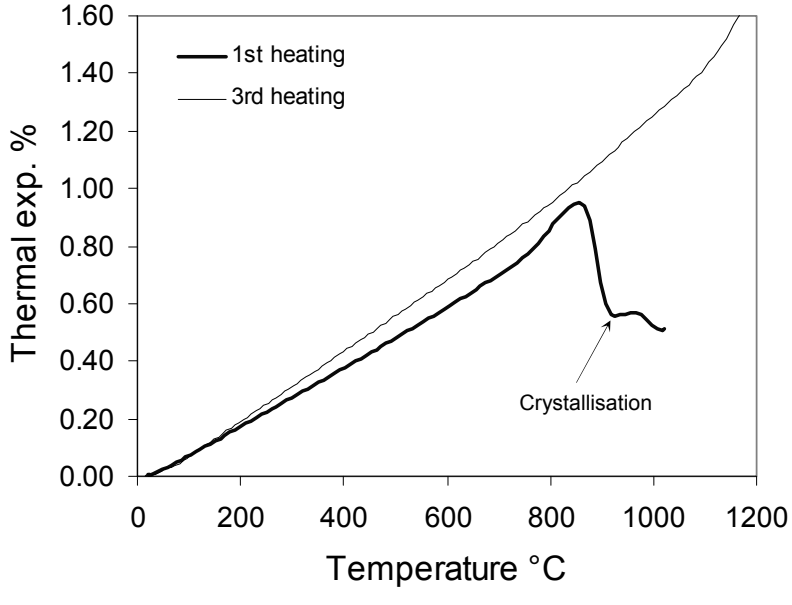

Thermal expansion of BLS glass (bold line) and devitrified BLS glass (thin line)

as shown by the thin curve in Figure 7.3, demonstrating that the sample had become fully crystalline. T_g, T_s and T_x derived from the dilatometer curve for the BLS glass is given in Table 7.5. T_g measured by the dilatometer was 747 °C, which is 13 °C lower than the temperature measured by DSC. This was expected due to 5 times higher heating rate in the DSC-measurements compared to the dilatometric measurements. The dilatometric softening point appeared at 856 °C and the onset of crystallization appeared at 926 °C, which is approximately the same as measured by DSC.

The thermal expansion of the crystallised glass is almost linear and shows no phase transitions in the range 20-1170 °C. The TEC is increasing in the whole temperature range with values as given in Table 7.6. The mean TEC in the range 20-1000 °C is $12.8 \cdot 10^{-6}$ °C^{-1}, which is close to the TEC of La_2NiO_4 of $12.4 \cdot 10^{-6}$ °C^{-1}. At ~ 850 °C the TECs of BLS and La_2NiO_4 are equal.

Table 7.6
Thermal expansion coefficients of crystallised BLS glass

Thermal expansion coefficients (TEC) x 10^{-6} °C^{-1}		
20-800 °C	20-1000 °C	20-1150 °C
12.2	12.8	13.5

7.3.3 EMPA of devitrified BLS glass

Backscatter image of the sintered and crystallised sample of BLS-glass revealed that three major phases were present distinguished by different grey colour as shown in Figure 7.4. The elemental composition is given in Table 7.7 as mean values of three independent analysis of each phase.

The most abundant phase seems to be the lightest phase S4 corresponding to $Ba_2La_2Si_4O_{13}$. The light grey phase (S5) was identified as $Ba_3Si_5O_{13}$ and the dark grey phase (S6) as $BaSi_2O_5$. A minor phase denoted C6 (the capital C followed by a number is used for contaminated phases) was occurring as black spots ~ 1μm or smaller located at triple points. This phase was contaminated with alumina probably from the sample preparation. Since the amount of this phase is negligible it has no influence on the conclusions and will not be discussed any further.

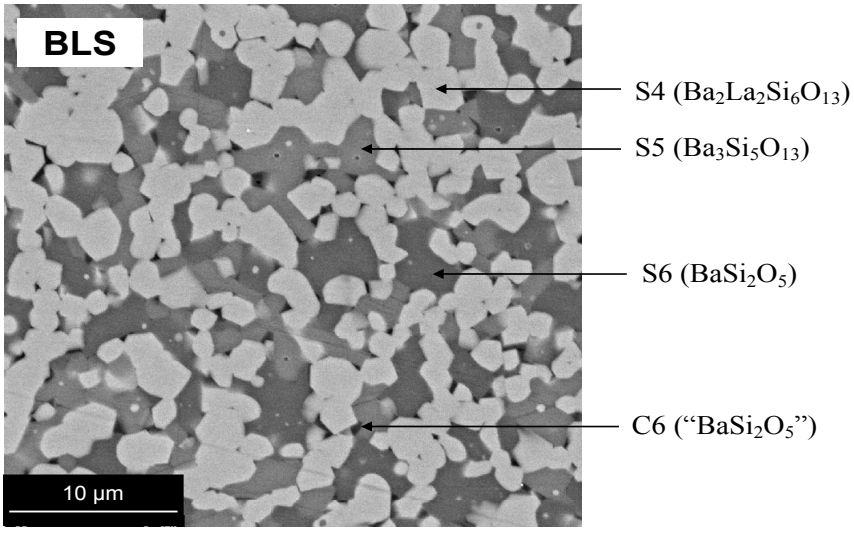

Figure 7.4
Backscatter image of BLS glass heated for 72 h at 1000 °C and 60 h at 1200 °C

Table 7.7
EMPA of phases identified in sintered BLS, fired 60 h at 1200 °C

Mixture	Phase ID	Composition (at. %)						Simplified composition
		Ba	La	Ni	Si	Al	O	
BLS	S4	10.5	10.2	0.0	22.0	0.1	57.2	$Ba_2La_2Si_4O_{13}$
	S5	15.2	0.5	0.0	26.3	0.4	57.6	$Ba_3Si_5O_{13}$
	S6	12.9	0.6	0.0	27.3	0.2	59.0	$BaSi_2O_5$
	C6	9.8	3.2	0.0	22.8	8.6	55.7	"$BaSi_2O_5$"

7.3.4 EMPA of BLS/La_2NiO_4 mixtures

The crystalline phases of the sintered 30/70, 50/50 and 70/30 mixtures were well developed and easy to distinguish from each other as demonstrated in Figure 7.5 a-c. The corresponding elemental analysis is given in Table 7.8.

In the 30/70 mixture three major phases were present. The most abundant phase appearing as light grey matrix phase was $Ba_2La_8Si_6O_{26}$ denoted S2 in Table 7.8. The "white" phase was La_2NiO_4 (S1). In mixture 50/50 the most dominant phase was $Ba_2La_8S_6O_{26}$ (S2) appearing as large "white" elongated crystals with hexagonal cross section. The grey phase between the S2 phase was "$BaSiO_3$" contaminated with alumina (denoted C8 in Table 7.6).

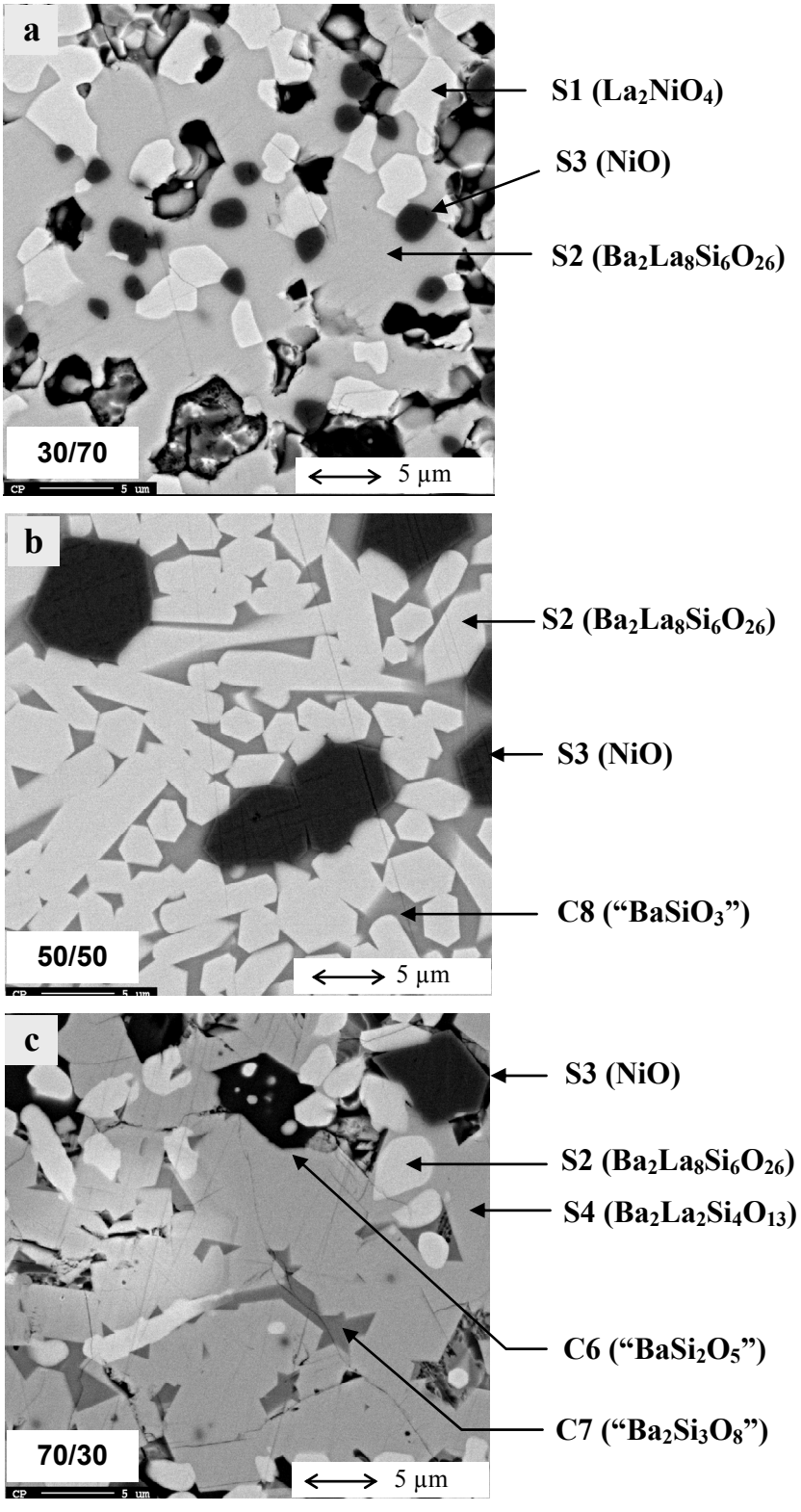

Figure 7.5
Backscatter images of the microstructure in powder mixtures of BLS/La_2NiO_4 heat treated for 170-320 h above 1240 °C

The microstructure of mixture 70/30 shown in Figure 7.4c was mostly constituted of a light grey phase (S4) with composition $Ba_2La_2Si_4O_{13}$. In addition the phase $Ba_2La_8Si_4O_{26}$ (white) was present. In accordance with expectation NiO (S3) was identified in all samples, visible as black rounded grains with blurred rim.

Two contaminated phases were identified in mixture 70/30; one black (C6), which contained 28 % alumina and one dark grey (C7), containing 14 % alumina and 2 % Ni. If the alumina is neglected the phase C6 becomes $BaSi_2O_5$ while the phase C7 becomes $Ba_2Si_3O_8$.

Table 7.8
EMPA of BLS/La_2NiO_4 powder mixtures after the final firing (see Table 7.3)

Mixture	Phase	Composition (at. %)						Simplified
	ID	Ba	La	Ni	Si	Al	O	composition
BLS/La_2NiO_4	S1	2.7	29.3	15.1	0.2	1.1	51.7	La_2NiO_4
30/70	S2	4.2	21.8	0.4	14.4	2.5	56.8	$Ba_2La_8Si_6O_{26}$
	S3	0.1	0.7	52.3	0.2	0.0	46.8	NiO
BLS/La_2NiO_4	S2	5.7	20.4	0.4	15.7	0.3	57.5	$Ba_2La_8Si_6O_{26}$
50/50	S3	0.2	0.4	52.8	0.2	0.1	46.3	NiO
	C8	14.2	1.7	0.9	15.6	15.6	52.0	"$BaSiO_3$"
BLS/La_2NiO_4	S2	5.5	19.2	0.2	16.1	2.6	56.4	$Ba_2La_8Si_6O_{26}$
70/30	S3	0.2	0.3	53.0	0.3	0.1	46.1	NiO
	S4	10.5	10.4	0.1	20.8	0.2	57.9	$Ba_2La_2Si_4O_{13}$
	C7	12.6	1.2	2.1	16.9	14.4	52.7	"$Ba_2Si_3O_8$"
	C6	6.7	0.2	0.2	14.1	28.5	50.4	"$BaSi_2O_5$"

7.3.5 X-ray diffraction of BLS glass and powder mixtures

Only the phase $BaSi_2O_5$ could be identified with certainty in the XRD pattern of the crystallised BLS glass as shown in Figure 7.6. Based on the EMPA of devitrified BLS glass (Table 7.7) the phases $Ba_3Si_5O_{13}$ and $Ba_2La_2Si_4O_{13}$ should also be present giving the following reaction:

$$BLS \rightarrow BaSi_2O_5 + Ba_3Si_5O_{13} + Ba_2La_2Si_4O_{13} \qquad 7.1$$

Regarding the BLS/La_2NiO_4 powder mixtures three phases were identified in the XRD patterns as demonstrated in Figure 7.7.

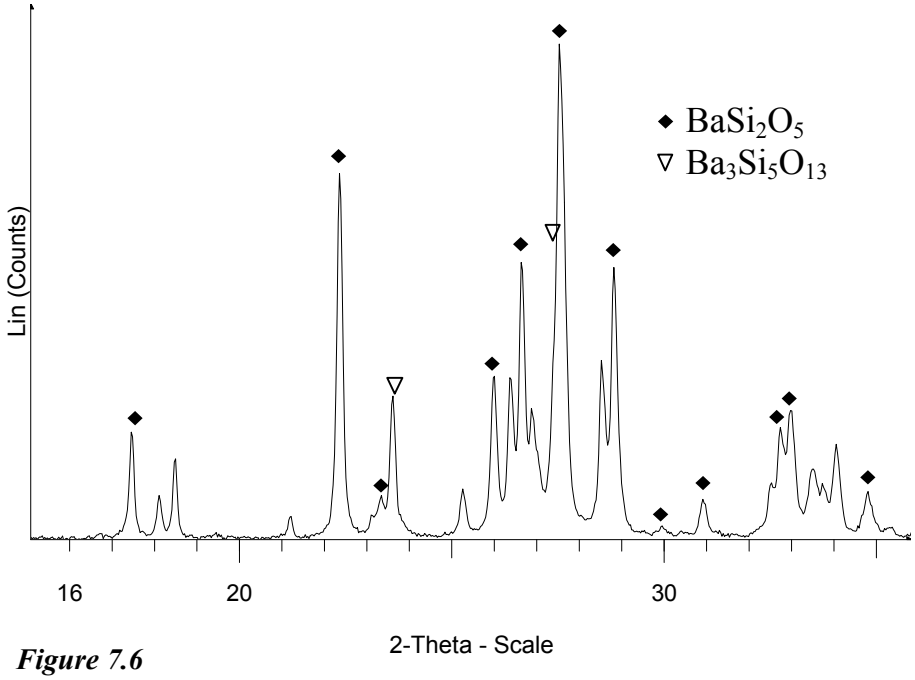

Figure 7.6
X-ray diffraction pattern of BLS glass heat treated for 30 h at 1230 °C. Only the phase $BaSi_2O_5$ could be identified with certainty. Unknown peaks are unmarked

The XRD diagrams of the three powder mixtures are almost identical and the most dominating reflections were due to $Ba_2La_8Si_6O_{26}$. With respect to La_2NiO_4, the X-ray diffractograms demonstrate that this compound is clearly present in the 30/70 mixture only. In the 50/50 mixture only trace amounts of La_2NiO_4 were detected while the 70/30 mixture contained no La_2NiO_4. NiO was present in all mixtures.

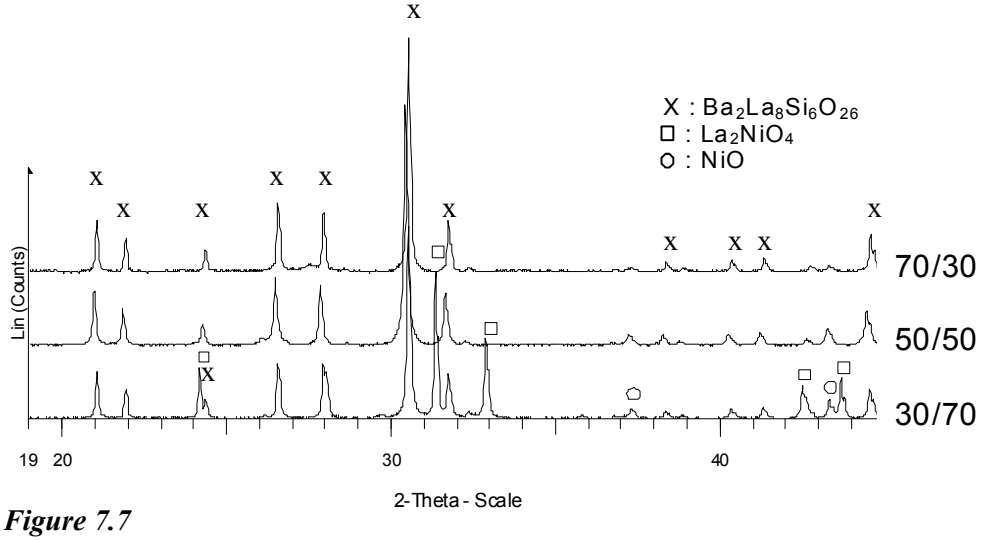

Figure 7.7
X-ray diffraction pattern of BLS/LN mixtures after the final heat treatment (1200 °C /86 h). The phases identified are given in the figure

These results show that La_2NiO_4 is consumed in the reaction with the glass, resulting in the formation of NiO and Ba-La-silicates and demonstrate that La_2NiO_4 is not coexistent with the glass.

The main phase formed in the reaction between BLS and La_2NiO_4 is belonging to the series: $Ba_xLa_{10-x}Si_6O_{27-x/2}$ possessing an apatite structure (Apatite: $A_6A_4(MO_4)_6O_2$) with $0.25 \leq x \leq 2$ [143]. The unit cell dimensions of this series increases with increasing content of Ba. The XRD pattern of the sample 30/70 was refined by a structureless Pawley type fitting procedure [144]. The resulting unit cell parameters were calculated to: a=9.778 Å and c= 7.329 Å. By comparing these values with data given by Vincent et al. [143] the composition is suggested to be $Ba_2La_8Si_6O_{26}$, which is in accordance with the EMPA. This phase is claimed to be a stable phase while compositions with $x \neq 2$ contain additional phases [145]. The only file in the PDF database that fitted the structure of $Ba_2La_8Si_6O_{26}$ was the file (00-027-0037) for the compound $Ba_4La_6Si_6O_{25}$, which possess an apatite structure and belongs to the apatite series $B_{2+x}La_{8-x}Si_6O_{26-x/2}$, x=0-2 [145]. The results are summarised in Table 7.9 where the powder diffraction files (PDF) used for the identification are included.

Table 7.9
Crystalline phases identified by XRD -analysis of sintered samples with reference to the PDF-files used for the identification [135]

Mixture	Phases identified by XRD	PDF-file [135]
BLS 1230°C	$BaSi_2O_5$	01-072-0171
	$Ba_3Si_5O_{13}$	00-26-0179
BLS/LN 30/70	NiO	01-075-0197
	La_2NiO_4	01-070-1333
	$Ba_2La_8Si_6O_{26}$	00-027-0037*
BLS/LN 50/50	NiO	01-075-0197
	La_2NiO_4	01-070-1333
	$Ba_2La_8Si_6O_{26}$	00-027-0037
BLS/LN 70/30	NiO	01-075-0197
	$Ba_2La_8Si_6O_{26}$	00-027-0037
	$Ba_2Si_3O_8$	01-072-1084

* PDF-file number is for the compound $Ba_4La_6Si_6O_{25}$

The X-ray powder analysis suggests that the main reaction taking place between the BLS-glass and La_2NiO_4 is:

$$BLS + La_2NiO_4 \rightarrow NiO + Ba_2La_8Si_6O_{26} \qquad 7.2$$

The findings from the EMPA are consistent with the XRD analysis and verify that equation 7.2 is the main reaction. La and Ni from La_2NiO_4 diffuse into the BLS-glass and form $Ba_2La_8Si_6O_{26}$ and $Ba_2La_2Ba_4O_{13}$. The NiO solubility in the silicate phases is low and pure NiO is observed with the silicate phases.

7.3.6 Diffusion couples La_2NiO_4-BLS

The reaction zone between BLS glass and La_2NiO_4 of the first diffusion couple (1300˚C/30 h) is depicted (backscatter image) in Figure 7.8, while the elemental composition of the identified phases is given in Table 7.10. Because the seal and membrane separated during the heat treatment only the seal is shown in Figure 7.8. Some horizontal cracks can be seen where the seal had been in contact with the membrane material. This will be commented in chapter 7.3.7.

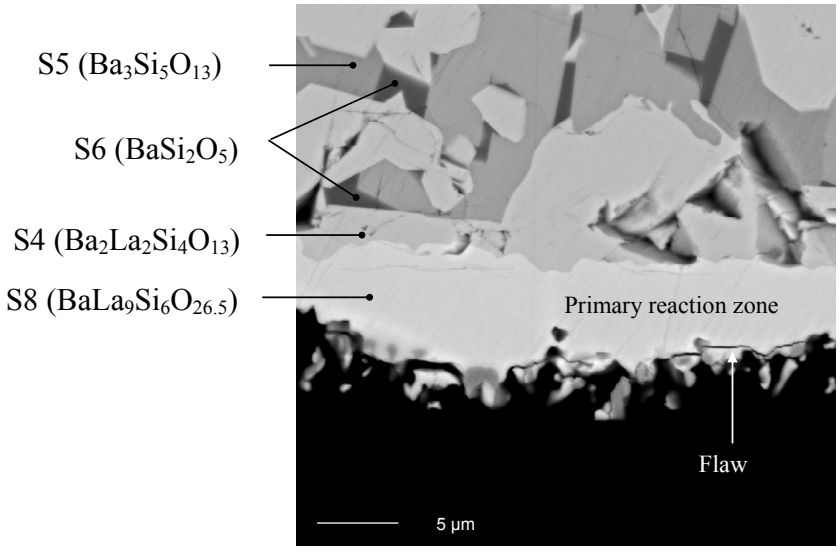

Figure 7.8
Backscatter image of diffusion couple 1; BLS glass/La_2NiO_4 heat treated for 30 h at 1300 °C

EMPA showed that at least four different crystalline phases were present in the seal, distinguished by different grey scale. The phase in intimate contact

with La_2NiO_4 has the composition $BaLa_9Si_6O_{26.5}$ (denoted S8), which is recognized as one of the compounds in the $Ba_xLa_{10-x}Si_6O_{27-x/2}$ apatite series. The thickness of this "primary" reaction zone is in the range 4-7 μm. In contact with the primary reaction zone follows a more or less continuous layer with the nominal composition $Ba_2La_2Si_4O_{13}$, recognized as the "new" silicate was formed. The same phase was also found far from the reaction border in form of well defined grains (light grey) together with the two other Ba-silicate phases: $BaSi_2O_5$ (S6 dark grey) and $Ba_3Si_5O_{13}$ (S5 grey). All phases are in good agreement with the phases identified in the sintered powder mixtures.

Table 7.10
EMPA of crystalline phases in diffusion couple1 (BLS glass in contact with La_2NiO_4 after 30 h at 1300 ˚C). The tabulated results are mean values of three independent point analysis in each phase

Phase ID	Composition (at. %)					Simplified composition
	Ba	La	Ni	Si	O	
S4	9.9	10.1	0.0	21.2	58.8	$Ba_2La_2Si_4O_{13}$
S6	11.5	0.1	0.0	27.4	61.1	$BaSi_2O_5$
S5	13.8	0.1	0.0	26.1	60.0	$Ba_3Si_5O_{13}$
S8	2.3	22.8	0.3	15.6	59.0	$BaLa_9Si_6O_{26.5}$

7.3.7 Diffusion couple 2

The microstructure of diffusion couple 2 was similar to the microstructure seen in diffusion couple 1 despite the much longer heating time. A backscatter image showing the complete seal layer between the La_2NiO_4 materials is depicted in Figure 7.9. The Figure shows that several flaws have been developed in the reaction zone. The elemental analysis of the phases identified in diffusion couple 2 is given in Table 7.11 while Figure 7.10 shows a backscatter image of the area where the EMPA was performed.

The composition of the primary reaction zone was $Ba_{1.5}La_{8.5}Si_6O_{26.25}$ (denoted S9), which is slightly different from the corresponding phase (S8) in diffusion couple 1, but is still one of the compounds in the Ba-La-Si apatite series and closer to the stable phase $Ba_2La_8Si_6O_{26}$. The thickness of the reaction zone is ~ 4-6 μm. On top of the primary reaction zone is an almost continuous layer of $Ba_2La_2Si_4O_{13}$. The same phase is also present in the crystallised glass far from the reaction interface together with the barium silicate phases $BaSi_2O_5$ and $Ba_3Si_5O_{13}$. $BaSi_2O_5$ was present in the two

darkest grey phases, while $Ba_3Si_5O_{13}$ was concentrated in the lightest grey phase, just as seen for diffusion couple 1.

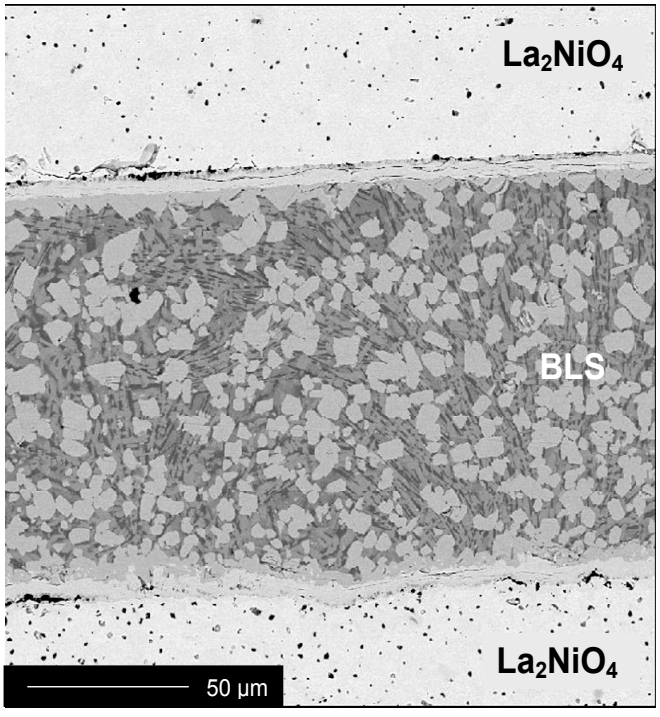

Figure 7.9
Backscatter image of the complete seal layer between the La_2NiO_4 ceramic parts in diffusion couple 2. A solid connection has developed between BLS-glass and La_2NiO_4 but flaws have developed along the reaction zone due to high shear forces

Table 7.11
EMPA of the observed phases in diffusion couple 2. The numbers are mean values of five independent point analyses of each phase

Phase ID	Composition (at.%)					Simplified composition
	Ba	La	Ni	Si	O	
S4	10.7	10.4	0.1	21.6	57.2	$Ba_2La_2Si_4O_{13}$
S5	15.4	0.2	0.1	27.0	57.3	$Ba_3Si_5O_{13}$
S6	11.2	0.2	1.1	24.0	63.5	$BaSi_2O_5$
S9	3.9	22.8	0.3	16.1	56.8	$Ba_{1.5}La_{8.5}Si_6O_{26.25}$
S1	0.0	31.2	16.4	0.1	52.3	La_2NiO_4

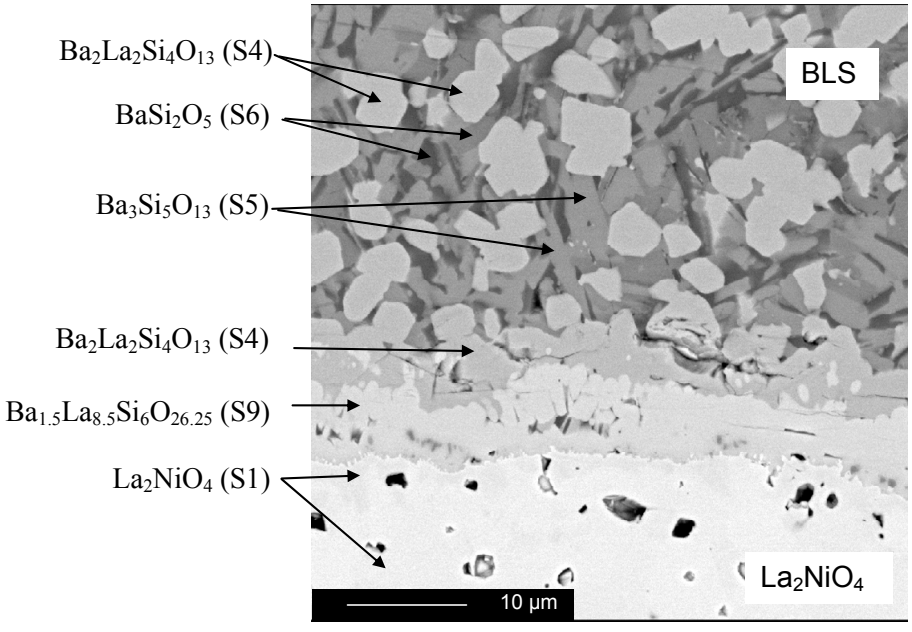

Figure 7.10
Backscatter image of the reaction zone between BLS glass and La_2NiO_4 in the diffusion couple 2. This sample had been held at temperatures in the range 900-1300 °C for 263 h

7.3.8 Characterization of $Ba_2La_2Si_4O_{13}$

EMPA of the synthesised $Ba_2La_2Si_4O_{13}$ showed that the sample was almost phase pure. Traces of the apatite phase $Ba_2La_8Si_8O_{26}$ and $Ba_3Si_5O_{13}$ were present as demonstrated in Figure 7.11b. Table 7.12 summarises the EMPA analysis.

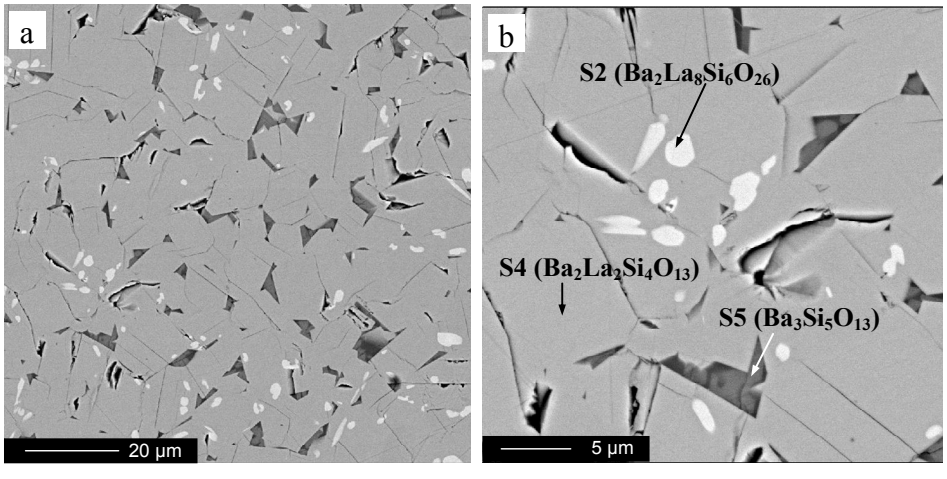

Figure 7.11
Electron backscatter images of the synthesized silicate $Ba_2La_2Si_4O_{13}$

Table 7.12
EMPA of synthesised $Ba_2La_2Si_4O_{13}$. The numbers are mean values of three independent analysis for each phase

Phase ID	Composition (at. %)				Comment	Simplified composition
	Ba	La	Si	O		
S2	5.0	20.4	16.1	58.5	White	$Ba_2La_8Si_6O_{26}$
S4	9.8	10.0	20.2	60.0	Grey	$Ba_2La_2Si_4O_{13}$
S5	14.0	1.1	24.2	60.7	Dark grey	$Ba_3Si_5O_{13}$

The XRD patterns changed for each firing (Figure 7.12) showing that equilibrium was not fully established. The results from EMPA support this observation. After the final heat treatment the system must be close to equilibrium, accordingly the XRD diagram obtained after heating for 96h at 1350 °C reflects the structure of $Ba_2La_2Si_4O_{13}$.

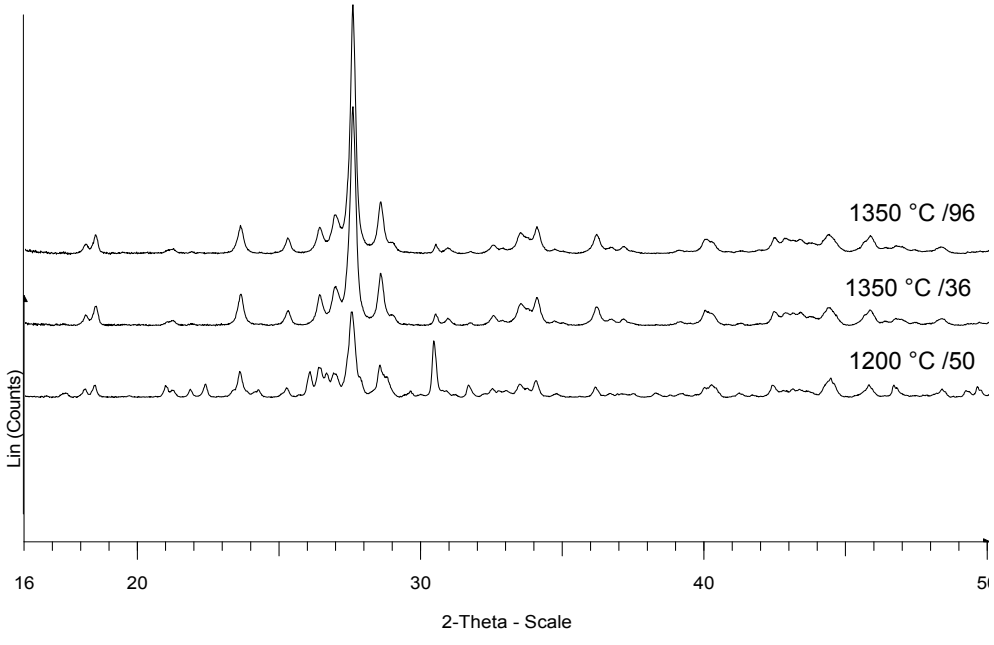

Figure 7.12
X-ray diffraction pattern of $Ba_2La_2Si_4O_{13,}$ showing how the crystal structure changes for different heat treatments

The XRD patterns after 36 and 96 h at 1350 °C are similar, while the pattern after 50 h at 1200 °C shows some diffraction lines that disappear at higher temperatures. The diffraction patterns are dominated by one strong line at 2θ =27.60° and quite a few reflections with low intensity. The strongest line

increases in intensity with increasing heat treatment showing that the structure becomes more and more ordered. The complexity of the pattern and the reflections at low 2θ suggest a crystal structure with low symmetry and a large unit cell volume. Based on the EMPA it is demonstrated that $Ba_2La_2Si_4O_{13}$ is a single ternary phase in the $BaO\text{-}La_2O_3\text{-}SiO_2$ system.

7.3.9 Thermal expansion of $Ba_2La_2Si_4O_{13}$ and $Ba_2La_8Si_6O_{26}$

The thermal expansion of $Ba_2La_2Si_4O_{13}$ after 2 thermal expansion cycles and of $Ba_2La_8Si_6O_{26}$ after 4 thermal expansion cycles is shown in Figure 7.13. From room temperature and up to 1000 °C $Ba_2La_2Si_4O_{13}$ expands 1.02 % while $Ba_2La_8Si_6O_{26}$ expands only 0.80 %. A more detailed analysis demonstrates that $Ba_2La_2Si_4O_{13}$ expands linearly from room temperature to 820 °C corresponding to a TEC of $10.1 \cdot 10^{-6}$ °C^{-1}. At 820°C the expansion becomes higher indicating that at this temperature there is a structural change in the material. From 820 °C the expansion continues linearly up to the maximum temperature, which was 1168 °C. The TEC in the temperature range 820-1168 °C was $12.8 \cdot 10^{-6}$ °C^{-1}. The mean TEC in the range 20-1168 °C was $10.8 \cdot 10^{-6}$ °C^{-1}, which is at the same level as for many of the electrolytes and interconnects that are candidate materials for SOFC and HT membrane reactors (see Chapter 3).

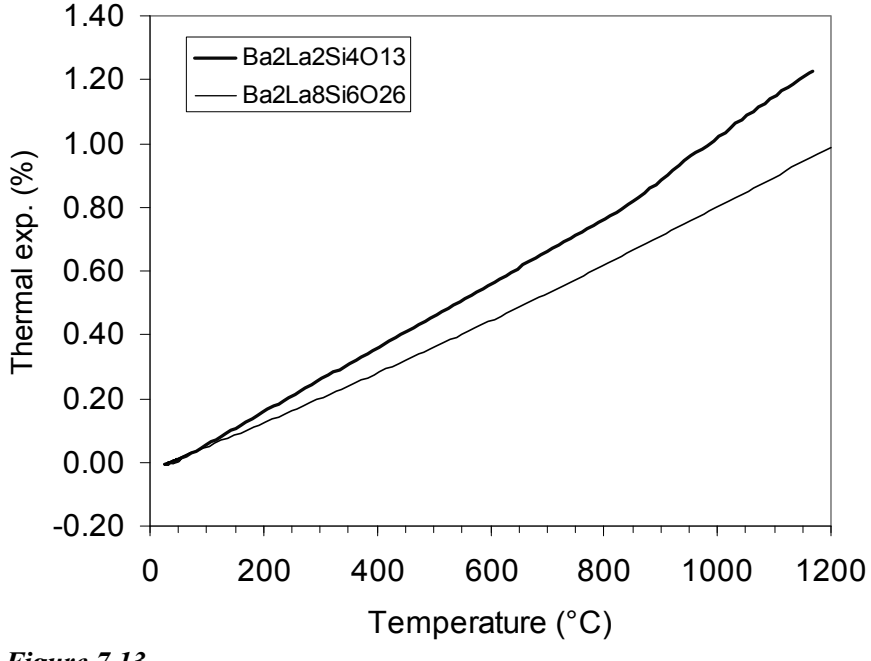

Figure 7.13
Thermal expansion of $Ba_2La_2Si_4O_{13}$ (bold line) and $Ba_2La_8Si_6O_{26}$ measured in air, using a heating rate of 2 °C /minute

The thermal expansion of the apatite $Ba_2La_8Si_6O_{26}$ is almost linear in the whole temperature range 20-1200 °C with a mean TEC of $8.5 \cdot 10^{-6}$ °C^{-1}. This low TEC explains the cracks observed in the reaction zone of diffusion couple 2 where the main phase was constituted of $Ba_{1.5}La_{8.5}Si_6O_{26.25}$. Due to the smooth shape of the thermal expansion curve, the thermal expansion (TE) of $Ba_2La_8Si_6O_{26}$ can be expressed accurately as a polynomial of second order:

$$TE_{\ Ba2La8Si6O26}\ (\%) = -0.02 + 7.126 \cdot 10^{-4}T + 1.104 \cdot 10^{-7}T^2 \qquad 7.3$$

Here T is given in °C and the polynomial is valid for the temperature range 20-1200 °C.

7.4 Discussion

7.4.1 Sealing properties

The combination of matching thermal expansion and extensive reaction between BLS-glass and La_2NiO_4 at elevated temperatures makes BLS-glass a good seal candidate for La_2NiO_4. As has been demonstrated the thermal expansion of the $Ba_2La_8Si_6O_{26}$ phase formed in the reaction between BLS-glass and La_2NiO_4, is however too low compared to the other phases present and causes extensive crack formation within the reaction zone[2]. The direction of the cracks indicates that shear forces have been dominating, which explains why the seal and membrane separated in diffusion couple 1. This demonstrates the importance of microstructure control of unwanted phases during the sealing process. It is not sufficient that the seal glass and membrane have compatible thermal expansion coefficients unless the same demand is put on the secondary phases formed during the sealing process. One way to overcome this problem is to limit the extension of this particular phase by optimising the temperature cycle for the sealing process.

Based on the dilatometric measurements of the BLS glass it should be possible to sinter the glass in the temperature range T_x-T_g corresponding to 747-926 °C before the glass starts to crystallise. However due to the high viscosity at these low temperatures the sintering rate is low and as soon as the temperature is increased above 800 °C the nucleation starts contributing

[2] EMPA of the phases in the reaction interface shows that the phases present are either $BaLa_9Si_6O_{26.5}$, diffusion couple 1, or $Ba_{1.5}La_{8.5}O_{26.25}$, diffusion couple 2. The synthesized compound $Ba_2La_8Si_6O_{26}$ belongs to the same series of apatites which all are expected to have similar thermal expansion. The general effect of increased Ba content in silicates is to increase the TEC. It is therefore likely that the compounds $Ba_{1.5}La_{8.5}O_{26.25}$ and $BaLa_9Si_6O_{26.5}$ have lower TEC than $Ba_2La_8Si_6O_{26}$.

to an increase in viscosity. For sealing purposes the seal should be heated fast up to a temperature where there is no nucleation e.g. above T_{liq} for sintering before it is being crystallised at a lower temperature.

In the present work the BLS-glass/La_2NiO_4 assembly was held for 2 hours at 1300 °C to melt the glass and then the temperature was lowered to 1050 °C for crystallization. At 1300 °C the diffusion processes are fast resulting in a wide reaction zone. By reducing the maximum temperature and holding time the thickness of the reaction zone can be reduced significantly resulting in an increased ability to resist crack formation. A suggestion could be a holding time of 10 min at 1300 °C and crystallization at 1000 °C. Another approach is to change the seal glass composition to promote formation of secondary phases with a TEC matching the TEC of La_2NiO_4. Optimizing the seal heating cycle and chemical composition of the seal glass is left for future work. Other ways to limit the reaction between seal and the joining materials are discussed in Chapter 12.

7.4.2 Phase relations in the ternary system $BaO\text{-}La_2O_3\text{-}SiO_2$

The combined results from the EMPA and XRD measurements give information of, which phases that are coexistent in the ternary system BaO-La_2O_3-SiO_2. Actually we are dealing with the quaternary system BaO-NiO-La_2O_3-SiO_2, but since NiO does not make any compounds with the other oxides the system can be considered as a ternary system BaO-La_2O_3-SiO_2. This system is not described in the literature, but the binary systems BaO-SiO_2 [146], La_2O_3-SiO_2 [147] and BaO-La_2O_3 [148] are reported. The three binary diagrams have been used to compose the corresponding ternary phase diagram as shown in Figure 7.14.

The composition of all known binary phases as well as the Ba-La-Si apatite series $Ba_{2+x}La_{8-x}Si_6O_{26-x/2}$ for x=0-2 [144], the BLS/La_2NiO_4 mixtures and the BLS-glass are plotted in the phase diagram. Alkemade lines are drawn in accordance with EMPA and XRD analyses. The dotted lines are uncertain, while the solid lines are regarded as confirmed by the results of the present work.

The BLS/LN 30/70 mixture should crystallise into La_2NiO_4, Ba_2SiO_4 and $Ba_2L_8S_6O_{26}$. Since the composition of mixture 30/70 is close to the line La_2O_3-$Ba_2La_8Si_6O_{26}$ in the Alkemade triangle La_2O_3-Ba_2SiO_4-$Ba_2La_8Si_6O_{26}$ the most abundant phases should be $Ba_2La_8Si_6O_{26}$ and La_2NiO_4 (represented by La_2O_3 in the reduced quaternary system). This is confirmed by Figure 7.5a. In addition there should be traces of Ba_2SiO_4, but this phase was not identified by EMPA or by XRD.

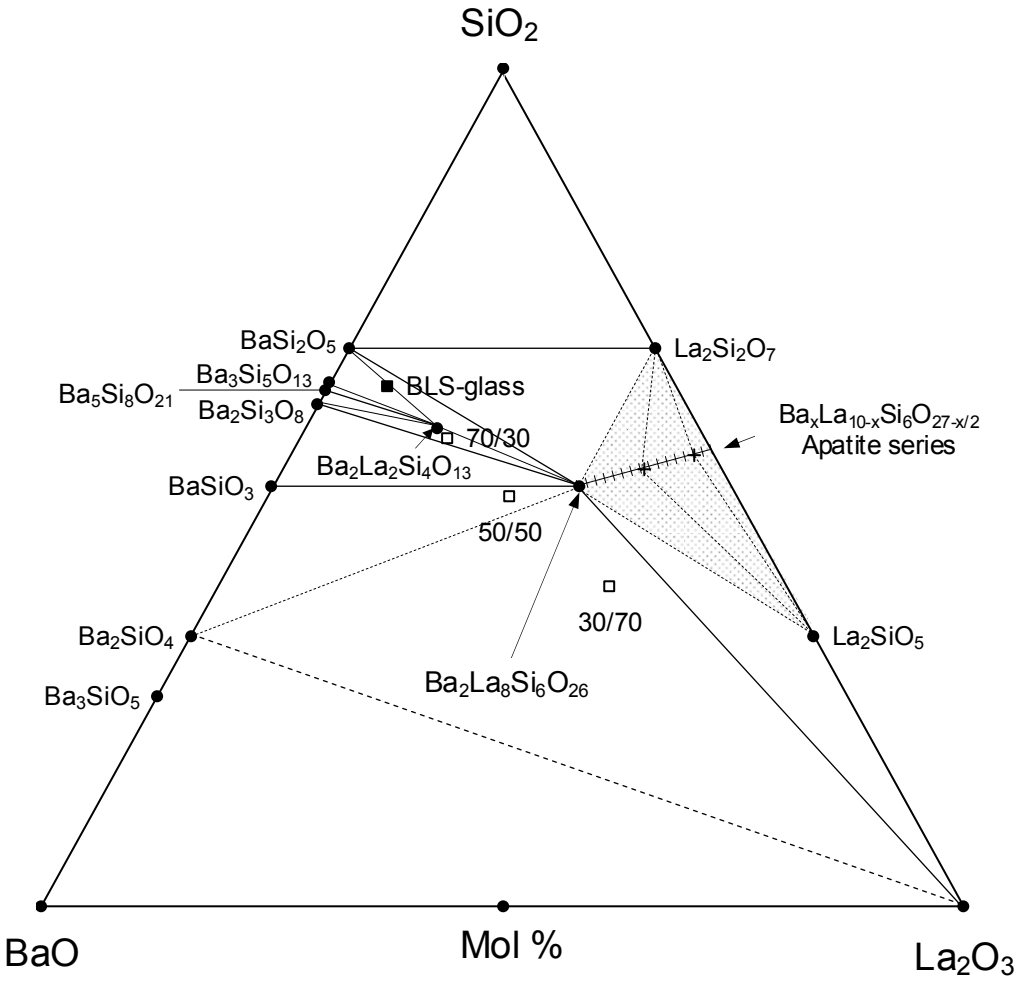

Figure 7.14
The ternary phase diagram composed of the three binary diagrams BaO-La_2O_3, BaO-SiO_2 and La_2O_3-SiO_2. The compositions of known phases and the powder mixtures studied in the present work are shown in the diagram

According to the proposed phase diagram in Figure 7.14 the 50/50 mixture should mainly consist of the apatite $Ba_2La_8Si_6O_{26}$ plus a few % of $BaSiO_3$ and should not contain any La_2NiO_4. This composition was confirmed by EMPA.

Mixture 70/30 has a composition within the Alkemade triangle $Ba_2Si_3O_8$-$Ba_2La_2Si_4O_{13}$-$Ba_2La_8Si_6O_{26}$ and should consist of only these three phases. Since the composition of mixture 70/30 is almost equal to $Ba_2La_2Si_4O_{13}$, $Ba_2La_2Si_4O_{13}$ should be the most abundant phase. In addition there should be some $Ba_2La_8Si_6O_{26}$ and traces of $Ba_2Si_3O_8$. This is in accordance with Figure 7.5c. The excellent agreement between the EMPA, the XRD data and the proposed phase diagram in Figure 7.14, make it possible to establish the reactions taking place between BLS-glass and La_2NiO_4 for the three mixtures:

BLS/La_2NiO_4 30/70

BLS-glass + $La_2NiO_4 \rightarrow Ba_2La_8Si_6O_{26} + La_2NiO_4 + Ba_2SiO_4$ 7.4

BLS/La_2NiO_4 50/50

BLS-glass + $La_2NiO_4 \rightarrow Ba_2La_8Si_6O_{26} + Ba_2SiO_4 + BaSiO_3$ 7.5

BLS/La_2NiO_4 70/30

BLS-glass + $La_2NiO_4 \rightarrow Ba_2La_2Si_4O_{13} + Ba_2La_8Si_6O_{26} + Ba_2Si_3O_8$ 7.6

Based on the reactions 7.1 and 7.4-7.6 exact mass balances have been calculated as given in Table 7.13. The number of moles of La_2NiO_4 that has reacted leaves an equal molar amount of NiO.

Table 7.13

Mass calculations of products based on the reactions 7.1 and 7.4-7.6

Reaction products	Amount of products (wt %)			
	Mixture BLS/La_2NiO_4 (wt.%)			BLS
	30/70	50/50	70/30	100.0
Ba_2SiO_4	6.6	4.0		
$Ba_2Si_3O_8$			19.7	
$Ba_3Si_5O_{13}$				4.0
$BaSiO_3$		10.2		
$BaSi_2O_5$				42.8
$Ba_2La_2Si_4O_{13}$			38.5	53.2
$Ba_2La_8Si_6O_{26}$	51.5	76.5	36.2	
NiO	6.4	9.3	5.6	
La_2NiO_4	35.4			

8 Seal performance - leakage tests

8.1 Introduction

The most important property for a seal is that it is tight and keeps tight for the whole life time of the device. The seal performance of the two assemblies CAM10-$LaNbO_4$-Al_2O_3 and La_2NiO_4-BLS-La_2NiO_4 has been tested at temperatures in the 900-1100 °C range by using an experimental setup designed for measuring gas permeation in dense membranes. One test on each system has been performed using air on one side of the membrane assembly and helium on the other side. Oxygen and nitrogen levels were measured on the He-side giving information about the leakage of the seal/membrane system. The chemical stability of the two glass seals in dry and humid CO_2 has also been tested.

8.2 Experimental

8.2.1 Preparation of flux test samples

The flux test samples were made as an assembly of the "flux test cup", seal and membrane as illustrated in Figure 8.1. The tablets for flux test cups and

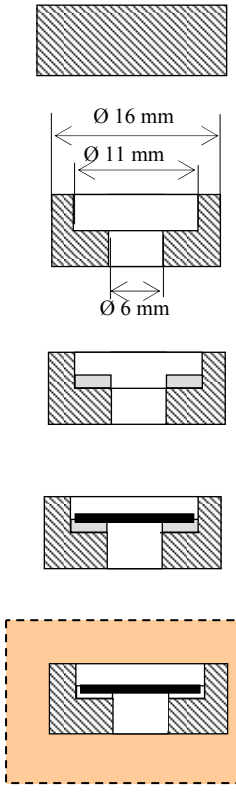

1: Sintered tablet Ø: 18-20 mm, Height: 7-9 mm

2: Machined tablet to fit a cylindrical membrane and seal, "Flux test cup".

3: Seal glass slurry in ethanol put in place in Flux test cup. The green seal was ca. 0.5-1 mm thick.

4: Polished membrane Ø 10 mm and 1-1.5 mm thick was put on top of seal.

5: Heat treatment of seal membrane assembly. Step 1: Glass melting, step 2: glass crystallization (see Table 8.1)

Figure 8.1 *Fabrication steps in preparing flux test samples*

the membranes were sintered as described in Chapter 5. The tablets (7-9 mm thick and 18-20 mm diameter) were machined (diamond tools) to fit for the membrane by making an 11 mm diameter hole half way through the tablets. In the centre a hole of 6 mm ø was drilled. Before the parts were assembled the membranes and flux test cups were polished (SiC-paper FEPA 2400 and 4000) and cleaned in an ultrasonic bath with ethanol. A thick slurry of seal glass powder (<45 µm particle size) in ethanol was placed in the bottom of the cups before the membranes were fixed by a gentle press.

The first assembly consisted of an alumina flux test cup, CAM-seal glass with 10 mol % MgO and $LaNbO_4$ membrane. The second assembly consisted of a La_2NiO_4 cup, BLS seal glass and La_2NiO_4 membrane as shown in Figure 8.2. After the seal slurry had dried for ~ 2 h at room temperature the flux test assemblies were heat treated according to Table 8.1 to establish the glass ceramic seals. The flux test sample with $LaNbO_4$ membrane ($LaNbO_4$ assembly) was heated to 1400 °C and the La_2NiO_4 assembly was heated to 1300 °C to melt the seal. The heating cycles are shown in Figures 8.3 and 8.4.

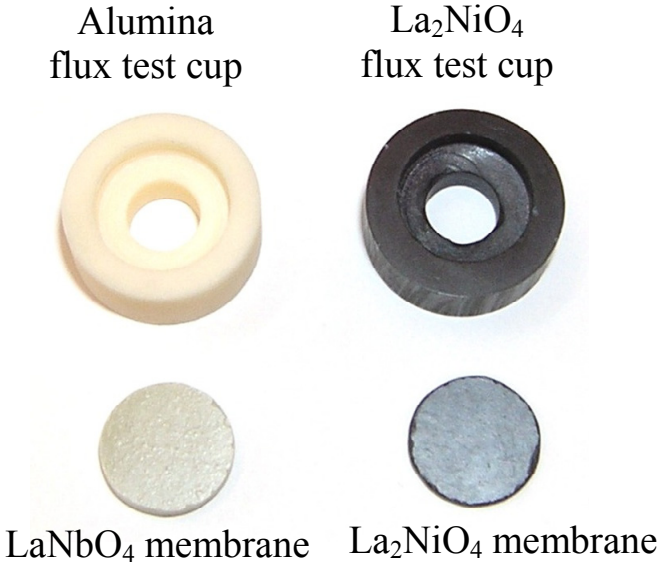

Figure 8.2
The machined alumina and La_2NiO_4 "cups" and the $LaNbO_4$ and La_2NiO_4 membranes (before polishing)

Table 8.1 *Temperature cycles for sealing of flux test samples*

Assembly	Temp. interval (°C)	Ramp (°C/h)	Hold (h)
$LaNbO_4$ assembly	20-1400	300	
	1400		1
	1400-1100	1000	
	1100		5
	1100-20	300	
La_2NiO_4 assembly	20-1300	200	
	1300		2
	1300-900	1000	
	900		0
	900-1050	200	
	1050		5
	1050-20	100	

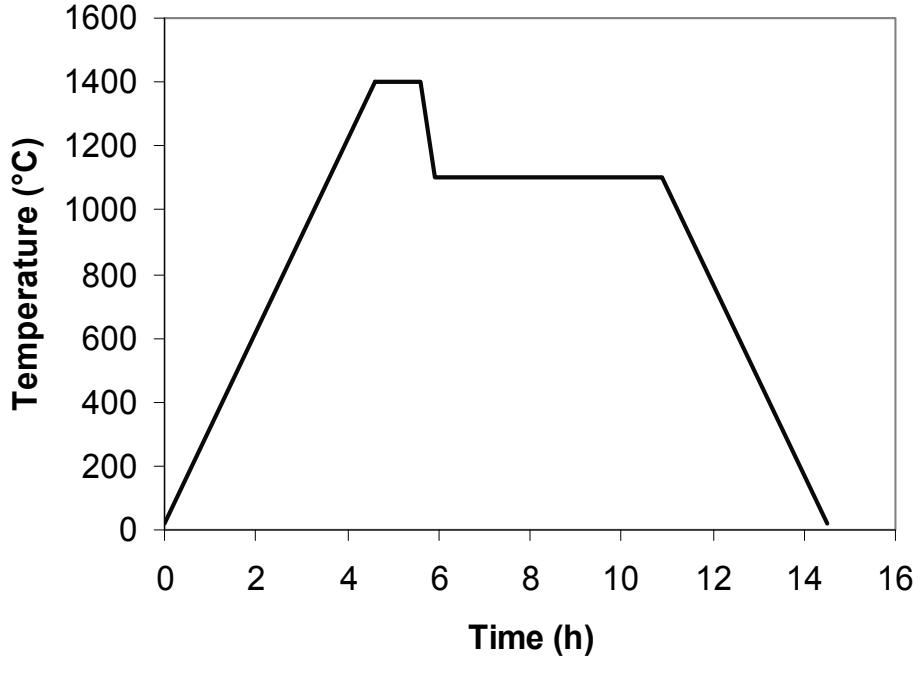

Figure 8.3
Heating cycle for sealing of $LaNbO_4$ -CAM10-Al_2O_3 flux test sample ($LaNbO_4$ assembly)

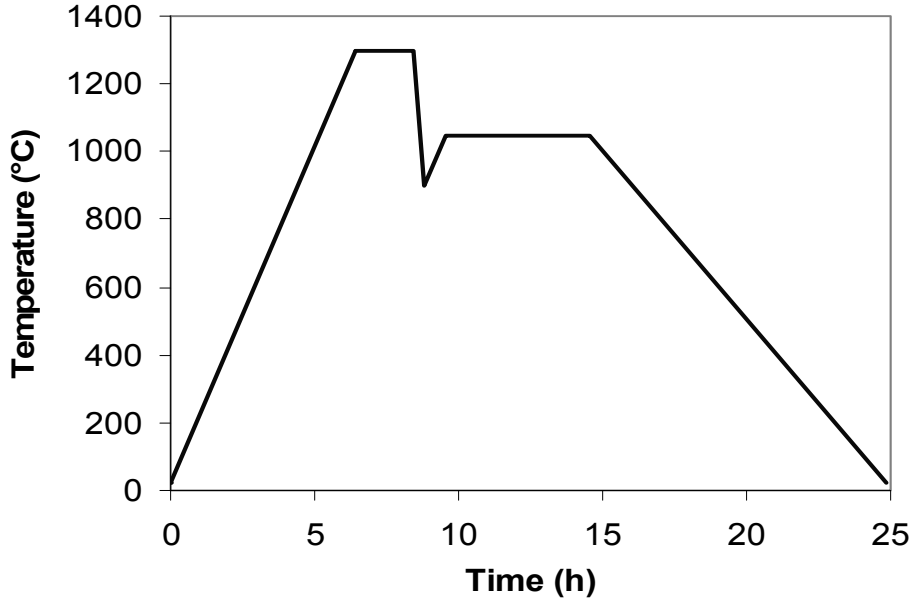

Figure 8.4
Heating cycle for sealing of the La_2NiO_4-BLS-La_2NiO_4 flux test sample (La_2NiO_4-assembly)

8.2.2 Experimental set up and gas analysis

The flux test was performed using the vertical furnace described in detail in Appendix 2. The sample was placed in the middle of the furnace between two alumina tubes sealed by use of a gold ring on each side of the sample as illustrated in Figure 8.5. The gold rings were made from 2.2 mm thick gold wire. To ensure that the gold seal was gas tight the assembly was heated close to the melting point of gold and kept at this temperature for 20 h using 2-3 kg load on the upper tube. During the test the lower tube (primary side) was flushed with synthetic air, while the tube on top (secondary side) was flushed with He 99.999 %. The gas leaving the secondary tube was analysed by means of a Micro GC (Varian Micro GC CP-2003, Varian Inc. USA). The GC was calibrated using 4 calibration gases consisting of He mixed with O_2 and N_2 in the concentrations given in Table 8.2. The temperature at the primary and secondary side was measured by two type S thermocouples inside the air and He gas tubes located 1-2 mm from the flux test sample as shown in Figure 8.5.

The calibration was performed by taking 15 independent measurements of each gas mixture following the calibration procedure given by the Micro-GC manufacturer (Varian Inc., USA). The gas flow used was 250-260 ml/min measured by a bubble flow meter (Agilent Optiflow 650). During

the flux test experiments the air and He flows were controlled using Brooks "Smart Mass Flow" controllers. During the test each measurement consisted of 15 individual scans that were run continually.

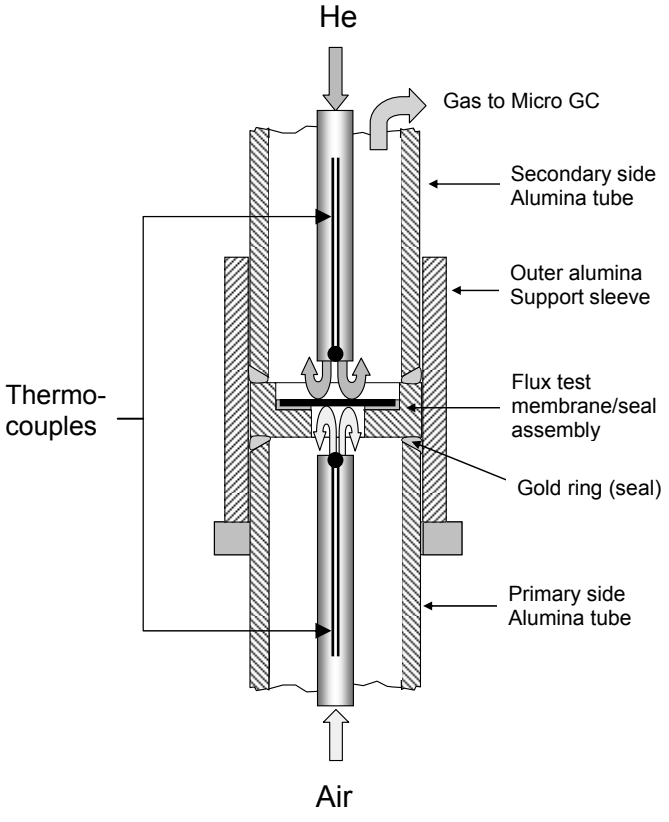

Figure 8.5
Flux test set up. The flux test assembly was sealed with gold rings that were pressed against the flux test sample by a load on the upper alumina tube. Air and He (99.999) was flushed on the primary and secondary side, respectively. The amount of oxygen and nitrogen in the He gas on secondary side was measured by means of a gas chromatograph

Table 8.2
Gases used for calibration of the Micro GC.

Gas	Mol %		
No	O_2	N_2	He
1	0.100	0.0957	Balance
2	0.95	1.02	Balance
3	3.01	13.84	Balance
4	6.06	22.4	Balance

The period between each individual measurement was approximately 3 minutes. High values for N_2 and O_2 were recorded for the first 2-5 analysis in a series of 15 measurements and these measurements were rejected. The mean value for N_2 and O_2 level for the other parallels was calculated. The total variation in each series was typically ±10 %. The test of BLS/La_2NiO_4 flux test sample was run for almost 11 days: 53 h at 1062 °C, 96 h at 1002 °C and 87 h at 904 °C. For sample CAM/$LaNbO_4$ a continuous measurement was performed over a period of 30 hours; 1 h at 1062 °C and 29 h at 1004 °C. The concentrations of oxygen and nitrogen in the He gas at the secondary side during the leakage tests were normally much lower than the concentrations in the calibration gas with the lowest content of oxygen and nitrogen. The uncertainty in the gas analysis is therefore considered to be substantially.

8.2.3 Heating procedure and data evaluation for BLS/La_2NiO_4 flux test sample

The samples were heated at a rate of 200 °C/h up to 1050 °C where the temperature was stabilized. The temperature was measured by the upper thermocouple. The temperature difference between the upper and lower thermocouples deviated less than 1.5 °C during the constant temperature periods. The load of 2-3 kg on the upper alumina tube was kept during the whole flux test. The temperature was increased manually in small steps from 1050 °C to 1062 °C (see Figure 8.6) to ensure a gas tight gold seal.

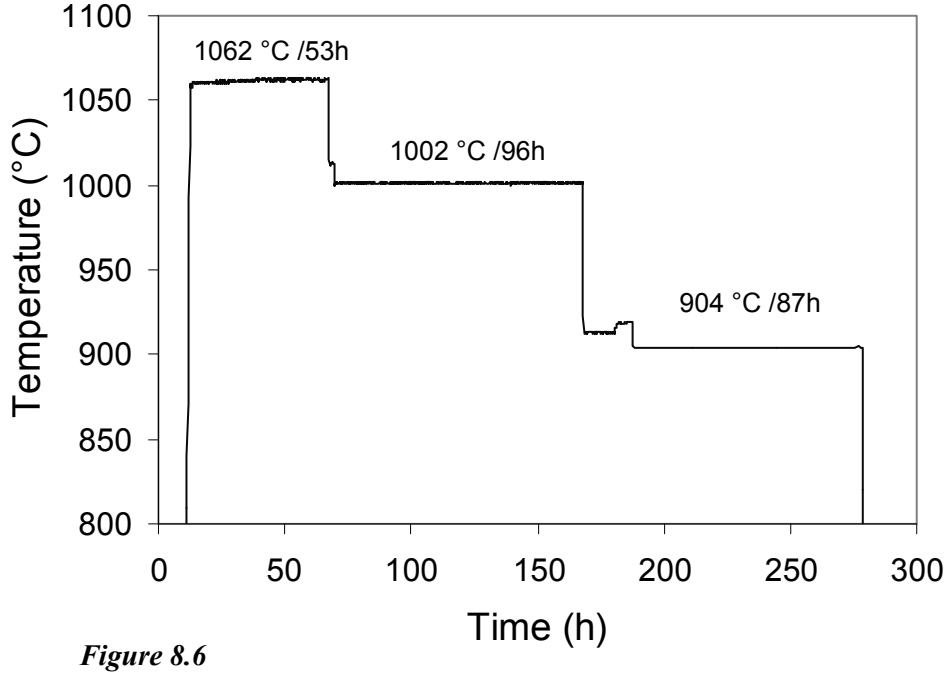

Figure 8.6
The temperature cycle used during leakage test of sample BLS/La_2NiO_4. The heating and cooling rates were 200 °C/h.

After 2 h at 1062 °C the measurements were started. Gas leakage measurements were performed over long periods at three different temperatures (1062 °C, 1002 °C and 962 °C). When the test was finished the furnace was cooled at a rate of 200 °C /h. The oxygen content on the secondary side due to air leakage was calculated from the nitrogen level on the secondary side since there is a constant O_2/N_2 ratio of 0.27 in air. The surplus of oxygen relative to air was due to oxygen permeation through the La_2NiO_4 membrane.

8.2.4 Heating cycle for CAM10/$LaNbO_4$/Al_2O_3 flux test sample

The leakage test of the CAM/$LaNbO_4$ assembly was more limited than for the BLS/La_2NiO_4 assembly due to problems with the equipment. The sample was held at 1062 °C for 47 h and at 1004 °C for 84 h as shown in Figure 8.7. Due to some experimental problems the gas analysis were not performed throughout the whole test period. The gas analysis obtained is for the last 1.2 h at 1062 °C period and for ~ 29 h at 1004 °C.

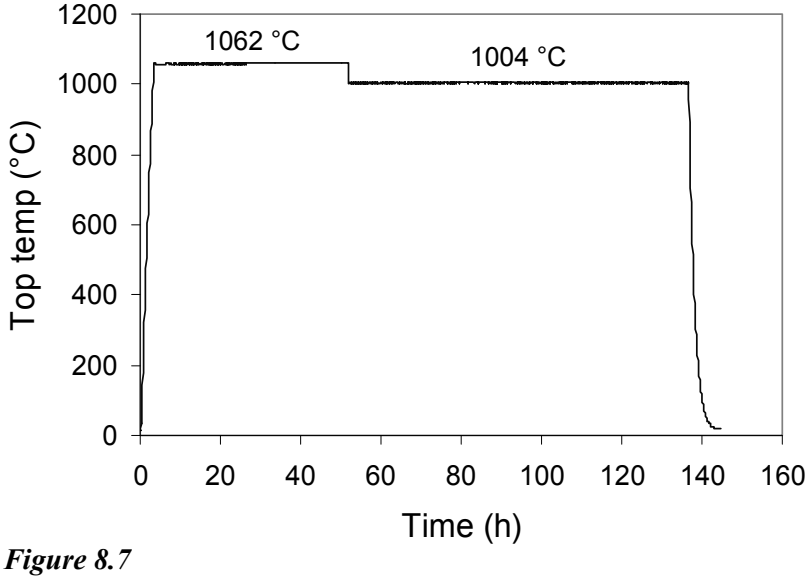

Figure 8.7
Temperature /time program for seal leakage test of sample CAM/$LaNbO_4$

8.3 Results

8.3.1 BLS/La_2NiO_4

The nitrogen and oxygen contents in the He-flow on the secondary side of the BLS/La_2NiO_4 flux test assembly increased as the temperature decreased, while the level of oxygen due to permeation through the membrane

decreased as shown in Figure 8.8. The increase in nitrogen level demonstrates an increasing leakage. The oxygen and nitrogen contents in the He-flow at 904 °C showed that the oxygen and nitrogen level increased slightly with time as demonstrated in Figure 8.9. The oxygen transport through the membrane was constant. Since the nitrogen level increased slightly an increasing air leakage occurred. This is consistent with the observed flaws in the reaction zone between the membrane and seal caused

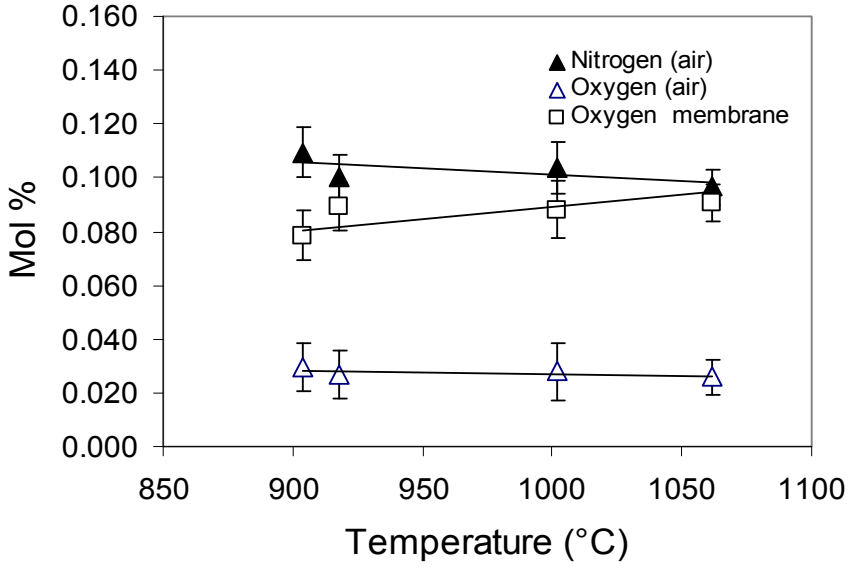

Figure 8.8
Nitrogen and oxygen level in gas flow on secondary side of the membrane seal assembly. The oxygen contribution from the membrane was calculated

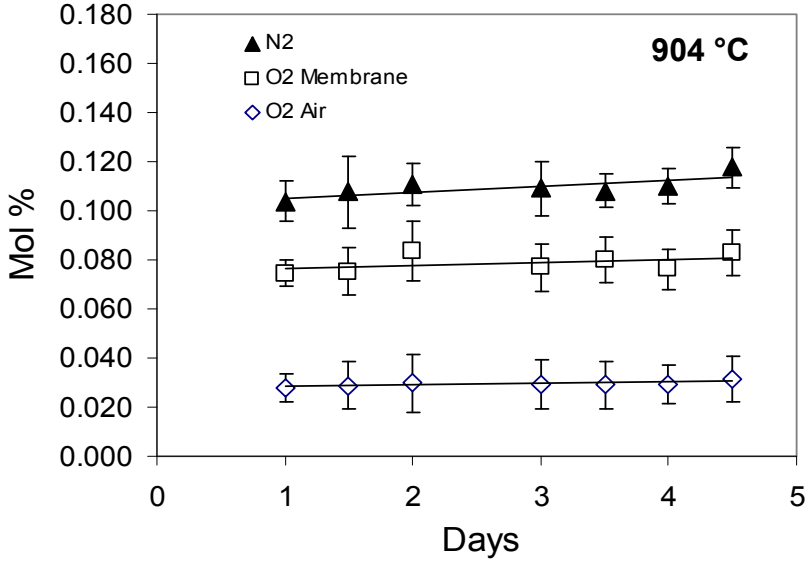

Figure 8.9
Oxygen and nitrogen content in the He-flush gas on secondary side of the seal/membrane assembly at temperature 904 °C

by the formation of the apatite phase $Ba_xLa_{10-x}Si_6O_{27-x/2}$ ($1<x<2$) (Figure 7.10). Since the reaction between membrane and seal will proceed at elevated temperatures the extent of crack formation will increase resulting in a gradually higher leakage rate. As the temperature is lowered the thermal expansion mismatch will increase and gradually lead to crack propagation, which also will give rise to an increased air leakage. The gas analysis results including the standard deviations are given in Table 8.3. The analysis performed after cooling (20 °C in Table 8.3) showed a ratio between oxygen and nitrogen of 1.0 demonstrating that the oxygen level was too high. This can not be explained by oxygen permeation through the membrane. The only explanation is that the measured oxygen content was too high or the nitrogen level too low.

Table 8.3
Micro GC analysis of oxygen and nitrogen levels in the He-flow on secondary side of the membrane seal assembly

Temp.	Measured (mol %)				Calculated (mol %)	
	O_2	O_2	N_2	N_2	O_2	O_2
(°C)		St. dev.		St. dev.	air leak.	membrane
1062	0.116	0.007	0.097	0.007	0.026	0.091
1002	0.116	0.011	0.104	0.010	0.028	0.088
918	0.116	0.009	0.100	0.008	0.027	0.089
904	0.108	0.009	0.110	0.009	0.029	0.078
20	0.083	0.008	0.102	0.009	0.027	0.056

8.3.2 CAM/$LaNbO_4$

The oxygen and nitrogen contents were practically constant in the whole period of measurements as shown in Figure 8.10. The mean values of the oxygen and nitrogen analysis confirm that there was no change in the concentration between 1062 and 1004 °C as given in Table 8.4. Since the $LaNbO_4$ essentially is a proton conductor it would be expected that the ratio between oxygen and nitrogen should be 0.27 as in air. The measured O_2 and N_2 gas concentrations gave an O_2/N_2 ratio of 0.78 showing that the oxygen level was much higher than in air. This can be explained by measurement uncertainty due to the low O_2 and N_2 concentrations. Another explanation can be that some oxygen has permeated through the membrane since $LaNbO_4$ at elevated temperatures is also to some extent an oxygen conductor. By calculating the amount of oxygen that is due to air leakage the result is 0.015 mol % (see Table 8.4), which shows that the seal can be considered as “gas tight”. The amount of oxygen due to oxygen permeation

through the membrane was 0.03 mol % (Table 8.4 column “Oxygen Mem”), which is the double of the leakage.

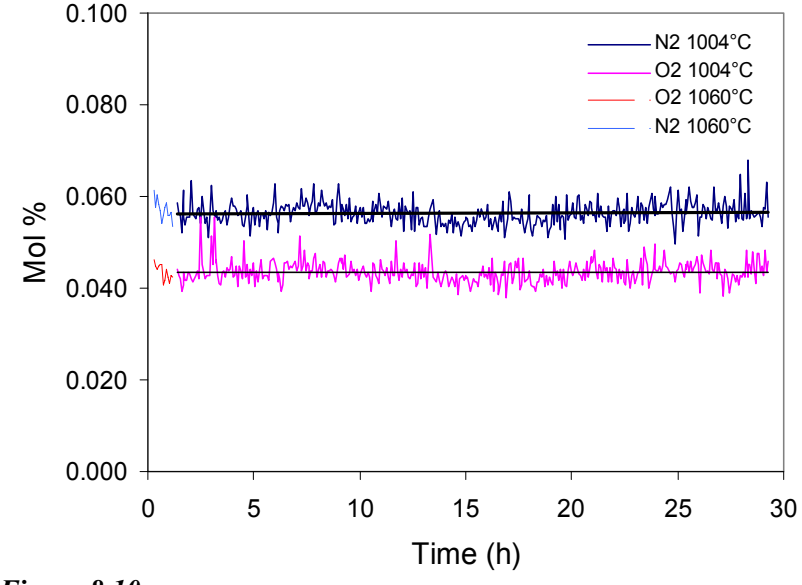

Figure 8.10
Oxygen and Nitrogen content in He-gas at secondary side of CAM/$LaNbO_4$ seal/membrane assembly at 1060 and 1004 °C

Table 8.4
Mean values of oxygen and nitrogen contents in He-gas at secondary side of CAM/$LaNbO_4$ seal/membrane assembly at 1060 and 1004 °C

Temp. (°C)	Oxygen Total (Mol %)	St. Dev. Total (Mol %)	Nitrogen Total (Mol %)	St.Dev Total (Mol %)	Oxygen Air (Mol %)	Oxygen Mem (Mol %)
1004	0.044	0.002	0.056	0.002	0.015	0.029
1060	0.043	0.002	0.057	0.002	0.015	0.028

8.4 Discussion

The leakage tests of the two membrane/seal assemblies showed that none of the seals had significant leakages but the experiments were not conclusive on this point due to two factors. The first is related to the low concentrations of nitrogen and oxygen that was measured in the He-gas at the secondary side. These concentrations were in the same range as- or lower than the oxygen and nitrogen concentrations of the calibration gas with the lowest oxygen and nitrogen contents, meaning that the analysis are associated with

uncertainties. In addition the Micro GC in it self had variations of ±10 % or more, between parallel measurements.

The second factor is related to the gold ring seal. When an air leakage occurs it is impossible with the current experimental setup to determine if the leakage is caused by the gold seal or by the glass ceramic seal. In the present work the "gold sealing" was prepared as carefully as possible and it is therefore believed that the gold seals were gas tight. By evaluating the gas analysis in the light of what was found by EMPA (Chapters 6 and 7) the results show that the BLS/La_2NiO_4 seal had a small leakage while the CAM/$LaNbO_4$ seal probably was gas tight. To be able to obtain conclusive results the flux test equipment must be improved so that all leakage sources can be measured individually.

9 Mechanical properties and residual stress

9.1 Stress calculations

Joining of two different materials by means of a third material acting as a rigid bonded seal put great demands on thermal expansion match of the three materials. Any mismatch in thermal expansion will cause residual stresses to build up during cooling from the temperature where the seal was established (sealing temperature). The material with the lower expansion will be in compression while the material with the higher expansion will be in tension. If the tensile stress passes the tensile strength, fracture of the material will occur. If accurate stress modelling is required the exact design of the device to be evaluated is necessary. The best is to use a finite element approach (FEM), but even simple models can give a good estimate of the stress levels and can be an effective tool in optimizing the performance of a given device. When rigid bonded seals are applied the most important material parameters are thermal expansion and mechanical strength.

An estimate of the residual stresses can be calculated from a simple model described by Faaland [150]. Figure 9.1 shows a typical assembly consisting of a substrate (3) with thickness t_3, the seal (2) with thickness t_2 and the membrane (1) with thickness t_1.

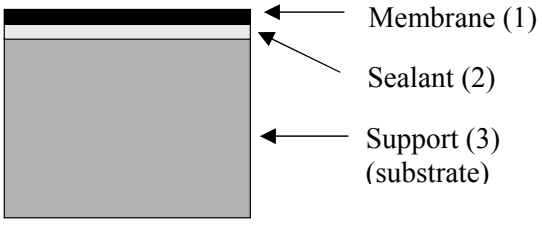

Figure 9.1
Support-seal-membrane assembly model

This geometry can be applied for stress modelling of the flux test samples described in Chapter 8, but also for stress calculations in planar SOFSs with design as shown in Figure 2.8 in Chapter 2.2.7, where a thin membrane is sealed to a thick interconnect (substrate). The support material will normally be much thicker than the membrane and seal. Typically the support thickness will be several mm, while the seal and membrane will be typically <100 μm thick. Bending will therefore not be allowed and all three layers will have the same strain ε.

By considering all layers to be isotropic and linearly elastic Hooke's law for an in-plane stress can be applied to this system. The stress normal to the

membrane surface is equal to zero; σ_z =0 and the stress in x- and y-directions are equal; $\sigma_x=\sigma_y$. With these preconditions the elastic stress in the layer i can be expressed as:

$$\sigma_i = \frac{E_i}{1-\nu_i}(\varepsilon_i - \alpha_i \Delta T) \qquad 9.1$$

Here: E_i = Young's modulus for layer i, υ_i is Posson's ratio (normally between 0.15 and 0.30), α_i is the TEC, ΔT is temperature change from a reference temperature T_0, and ε_i is the overall biaxial strain i.e. the actual expansion of a volume-element when it is not allowed to expand freely, but is constrained as part of an elastic body. The term $\alpha_i \Delta T$ is the thermal strain. Thus, the total strain in each layer is given as:

$$\varepsilon_i = \frac{(1-\upsilon_i)}{E_i}\sigma_i + \alpha_i \Delta T \qquad 9.2$$

Since all have the same strain: $\varepsilon_1=\varepsilon_2=\varepsilon_3$, we get the following equations:

$$\frac{(1-\upsilon_1)}{E_1}\sigma_1 + \alpha_1 \Delta T = \frac{(1-\upsilon_2)}{E_2}\sigma_2 + \alpha_2 \Delta T \qquad 9.3$$

$$\frac{(1-\upsilon_2)}{E_2}\sigma_2 + \alpha_2 \Delta T = \frac{(1-\upsilon_3)}{E_3}\sigma_3 + \alpha_3 \Delta T \qquad 9.4$$

Since there is no stress in z-direction force balance requires that:

$$\sum_{i=1}^{3} \sigma_i t_i = 0 \qquad 9.5$$

It can be shown [150] that solving equations 9.3-9.4 give the following results when the thickness of membrane and seal is negligible compared to the thickness of the support.

Membrane: $$\sigma_1 = -\Delta T(\alpha_1 - \alpha_3)\frac{E_1}{1-\nu_1} \quad 9.6$$

Sealant: $$\sigma_2 = -\Delta T(\alpha_2 - \alpha_3)\frac{E_2}{1-\nu_2} \quad 9.7$$

Support: $$\sigma_3 = 0 \quad 9.8$$

In addition to stresses caused by thermal expansion there might also be a contribution from chemical expansion that depends on the oxygen potential. This effect is neglected in the case studied here since La_2NiO_4 and $LaNbO_4$ have practically no chemical expansion. By convention, negative stress values indicate compressive stress and positive values tensile stress. Since ceramics are brittle materials the ideal case is to expose all components to moderate compressive stress and to avoid tensile stresses. By exposing the membrane and seal to moderate compressive stresses a moderate tensile stress will develop in the support. This can be achieved by choosing;

$$\alpha_1 \leq \alpha_2 \leq \alpha_3$$

9.2 Stress in rigid bonded assemblies of La_2NiO_4, Al_2O_3 and crystallised BLS

Important for the stress development in a rigid bonded system based on La_2NiO_4, Al_2O_3 and crystallised BLS is the thermal expansion of these compounds plus the secondary phase $Ba_2La_8Si_6O_{26}$ as shown in Figure 9.2. The values are calculated from a 3rd degree linear regression of the measured thermal expansion curves. The thermal expansion of Al_2O_3 and $Ba_2La_8Si_6O_{26}$ is almost the same and the thermal expansion of the crystallised BLS seal and La_2NiO_4 is also close in value. In a typical sealing cycle with BLS-glass the assembly, support-seal-membrane, is heated to a temperature where the glass viscosity is ~ 10^2 Pa·s in order to achieve a dense seal. After a short soak time the temperature is lowered rapidly to a level where nucleation starts. The temperature is then increased to a level where the seal will crystallise during a reasonable time. At this temperature $T_{o,}$ the whole assembly will be under zero stress.

The residual stress build up depends on the relative thermal shrinkage of the materials from T_o to room temperature. The relative thermal expansion of the four materials taking T_o as 1000 °C is shown in Figure 9.3. There will be almost no stress between Al_2O_3 and $Ba_2La_8Si_6O_{26}$ during cooling from 1100

°C. The alumina will be in moderate compression and $Ba_2La_8Si_6O_{26}$ in moderate tension. A similar situation occurs for BLS-La_2NiO_4, but since the thermal expansion mismatch is higher, the stress levels will also be higher. The membrane will be in compression from 1000 °C to room temperature. Figure 9.3 also shows that alumina is not a good choice as support for the La_2NiO_4/BLS membrane seal system. By applying equations 9.6 and 9.7, a quantitative picture of the stress levels can be obtained as shown in Figure 9.4.

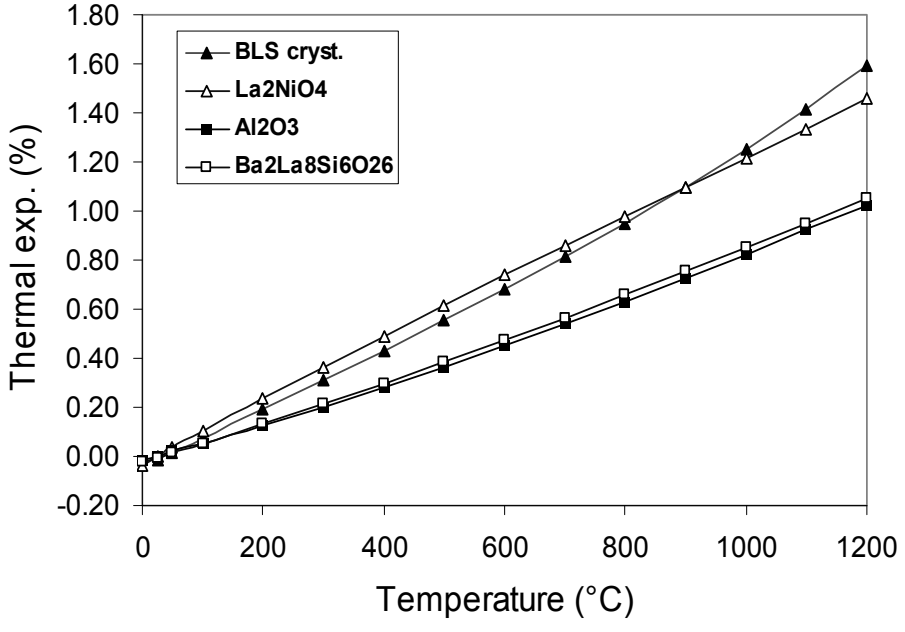

Figure 9.2
Thermal expansion of alumina, La_2NiO_4, crystallised BLS seal and $Ba_2Las_8Si_6O_{26}$

Poisson's ratio was set to 0.25 for all materials in the calculations. Young's modulus for the crystallised seal and $Ba_2La_8Si_6O_{26}$ was set to 100 MPa and for La_2NiO_4 to 200 MPa. The data show that there is a considerable tensile stress in both the membrane and the seal when alumina is used as support as shown in Figure 9.4 by the open and close triangles respectively. If a tensile strength of 100-150 MPa is assumed for the membrane and the seal the membrane and seal would crack at a temperature in the range 700-800 °C. When La_2NiO_4 is used as support the maximum tensile stress in the BLS seal is calculated to 128 MPa showing the possibility to cool to room temperature without cracking. However this requires refinement of the sealing cycle in order to reduce the amount of the apatite phases $Ba_xLa_{10-x}Si_6O_{27-x/2}$ ($1<x<2$) as discussed in chapter 7.3.4.

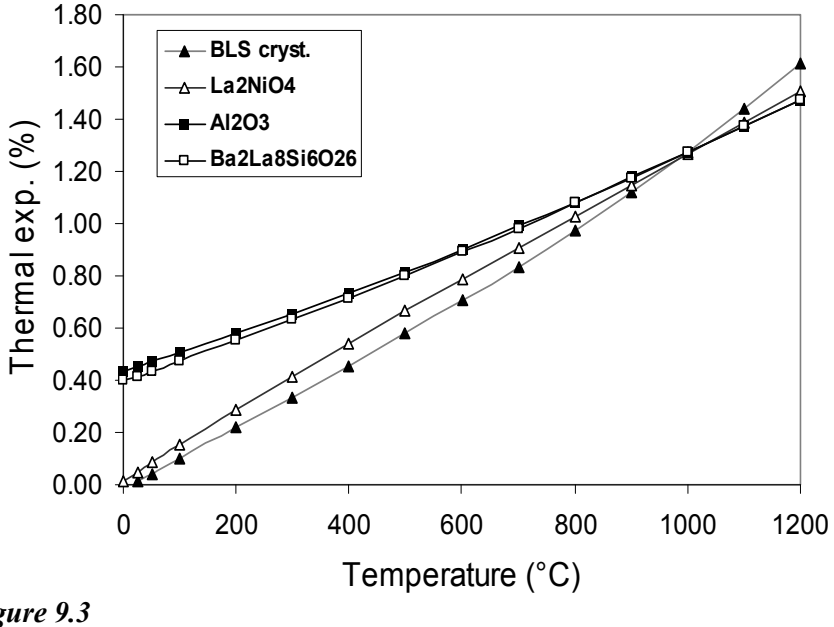

Figure 9.3
Thermal expansion of La_2NiO_4, Al_2O_3, BLS and $Ba_2La_8Si_6O_{26}$ for the case of zero stress at 1000 °C

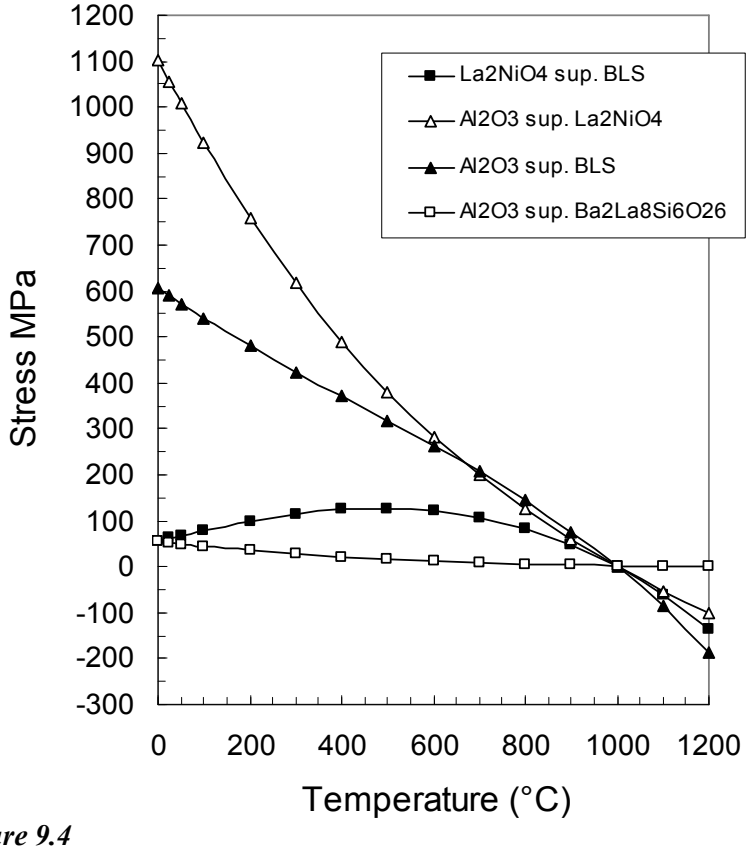

Figure 9.4
Calculated residual stress in BLS with La_2NiO_4 as support (closed squares), BLS with Al_2O_3 as support (closed triangles), La_2NiO_4 on alumina support (open triangles) and $Ba_2La_8Si_6O_{26}$ on alumina support (open squares), for the case of zero stress at 1000 °C. Negative stress means compression by convention

9.3 Stress in the bonded system $LaNbO_4$-CAM10-alumina

The residual stress in a system consisting of alumina as support material, CAM10 as seal material and $LaNbO_4$ as membrane has been evaluated using the same approach as for the La_2NiO_4-BLS system. The thermal expansion of the three materials calculated from 3rd degree linear regression of the thermal expansion curves is shown in Figure 9.5.

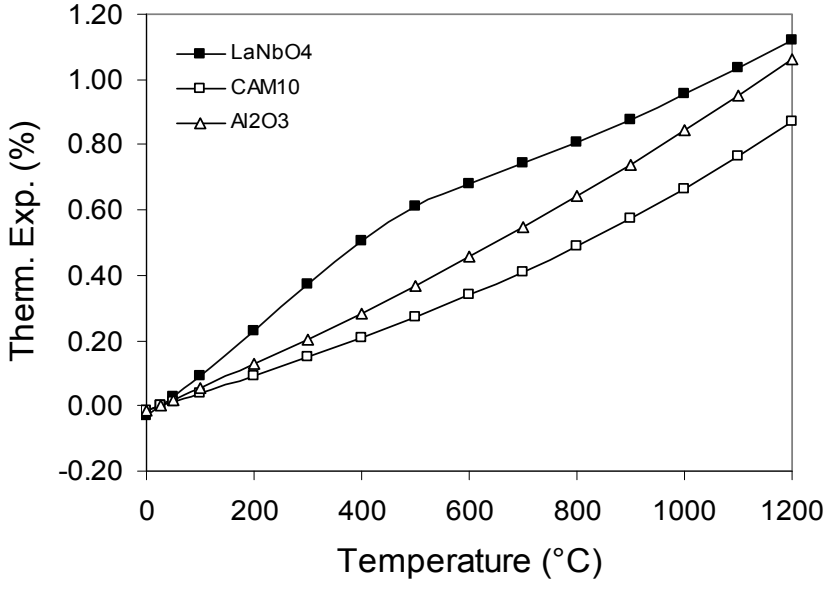

Figure 9.5
Thermal expansion of $LaNbO_4$, crystallised CAM10 and Al_2O_3

Since $LaNbO_4$ has a phase transition at ~ 530 °C two polynomials have been used to calculate the expansion, one polynomial for temperatures below 530 °C and one for temperatures above 530 °C. The sealing temperature where the system is unstressed is set to 1100 °C, giving the thermal expansion curves shown in Figure 9.6. The difference in thermal expansion is not large and extreme stresses are not expected to develop. The stress that builds up in the membrane and the seal at temperatures different from the sealing temperature at 1100 °C is shown in Figure 9.7. The calculations are based on a Poisson ratio of 0.25 for all three materials, a Young's modulus of 100 MPa for the CAM10 seal and 50 MPa for $LaNbO_4$[3].

[3] The Young's modulus of $LaNbO_4$ was estimated on basis of the stress strain measurements performed by Mokkelbost at ambient temperature [151] on $LaNbO_4$ sintered at 1200 °C. The mean value for Young's modulus at increasing stress for the linear part of the stress strain curves was 53 GPa. At elevated temperatures Young's modulus normally decreases slightly. In the calculations an E-modulus of 50 GPa has been applied.

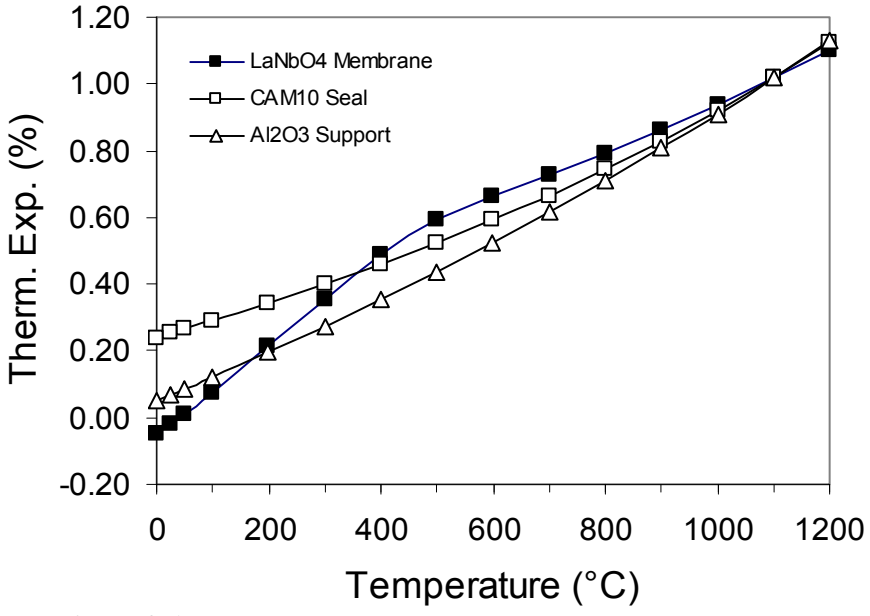

Figure 9.6
Thermal expansion of $LaNbO_4$, crystallised CAM10 and Al_2O_3 with reference temperature 1100 °C

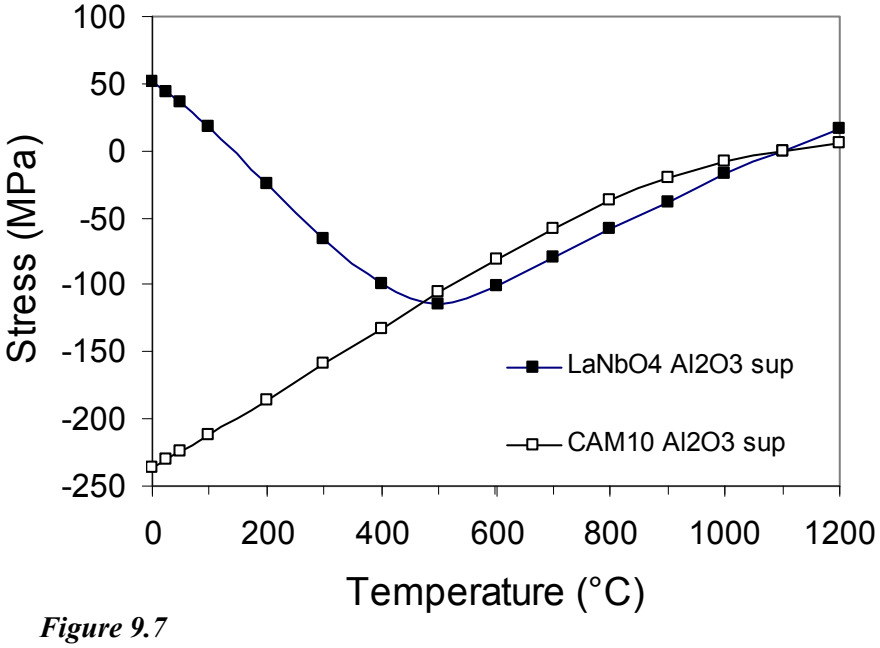

Figure 9.7
Calculated stress in $LaNbO_4$ membrane (closed squares) and CAM10 (open squares) in the temperature range 25-1200 °C with Al_2O_3 as substrate material. At 1100 °C the system is unstressed

With the alumina support the CAM10 seal is in compression in the whole temperature range 1100-25 °C. At 1200 °C the seal is in low tension of 5 MPa. At 25 °C the compressive stress in the seal is calculated to 230 MPa. The membrane is in compression from 1100 °C to ~ 140 °C and in moderate tension at lower temperatures. The relative stress between membrane and seal is reasonably low from 1100 °C to ~ 470 °C. Below ~ 470 °C the stress builds up, but if it will result in crack formation is uncertain since the strength of the seal and membrane has not been measured.

9.4 Conclusion

The stress calculations for $LaNbO_4$/CAM10/Al_2O_3 show that alumina is well suited as support. The residual stresses building up during cooling from the sealing temperature of 1100 °C are so low that this system looks promising. For La_2NiO_4/BLS/Al_2O_3 the mismatch in thermal expansion between seal/membrane and alumina is so large that the seal/membrane will separate from the alumina support due to high shear forces. Alumina can not be used as support in this case. A suggestion is to use the seal material as a combined seal and support.

10 Reaction between seal glass and the atmosphere

10.1 Introduction

Materials that are to be applied in SOFC's and high temperature membrane reactors will be exposed to both oxidizing and reducing humid atmospheres. In combustion systems the atmosphere will typically contain CO, CO_2, H_2 and CH_4. The alkaline earth elements are known to form stable carbonates and hydroxides and since the two seal materials CAM and BLS contain Ca, Mg and Ba they were exposed to humid atmosphere containing CO_2 at elevated temperatures to evaluate the stability under these conditions.

10.2 Experimental

10.2.1 Experimental set up for gas exposure

The general experimental set up for the gas exposure tests is shown in Figure 10.1. Powdered samples (1.1-1.9 g batches) of BLS, CAM10 and CAM with 10 mol % MgO (denoted CAM10b), both glassy and crystallised, where placed in alumina "boats" and exposed to wet and dry CO_2 and air atmospheres. A horizontal gas tight tube furnace was used. A constant flow of CO_2 (99.9992) was led through the furnace. The gas flow of 3 Nl/h (Nl = normal liter) was controlled by mass flow meters (MFM) (Bronkhorst)

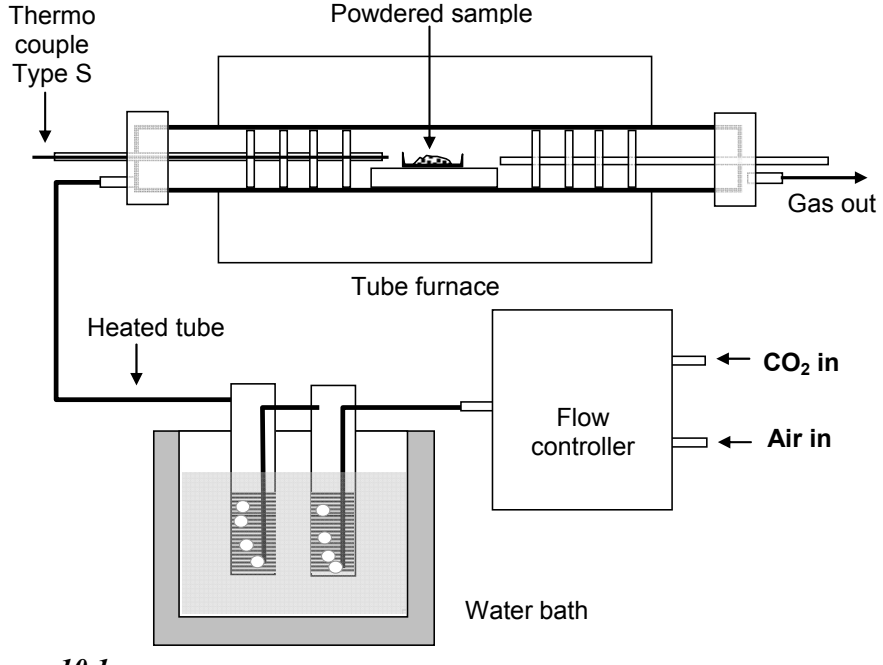

Figure 10.1
Sketch of the main experimental setup for gas exposure experiments with wet and dry gas

except for the first run (dry atmosphere) where the flow was measured by leading the gas from the furnace through a bubble flask. The bubbling rate (80-120 bubbles/min) represented a flow in the range 2-3 l/h. For the humid atmosphere experiments, the CO_2 gas was led through two water filled gas washing flasks at 41 °C before it was led into the furnace through a heated tube to avoid condensation of water. The samples from the gas exposure experiments were characterised by XRD and by weighing using a Mettler AE100 balance with resolution 0.1 mg.

10.2.2 Glassy and crystalline CAM10 in dry CO_2

CAM10 glass and CAM10 crystallised for 40 h at 1300 °C CAM10 and milled to particle diameter < 45 µm, were exposed to dry CO_2 for 72 h at 792 °C. The CO_2 flow was measured by means of a bubble flask, however a large leakage in the furnace gave a real CO_2 flow much higher than 2-3 Nl/h. The glassy sample was heated again to 1000 °C for 20 h in dry air. X-ray diffraction was performed both after the CO_2 and air exposure.

10.2.3 CAM10 glass exposed to alternating dry CO_2 and air at 800-1100 °C

The effect of alternating atmospheres of CO_2 and air at different temperatures and exposure times on CAM10 glass (particle diameter < 45 µm) was studied in two experimental series. In the first series the CAM10 glass was kept at temperatures in the range 800 to 1100 °C with holding times of 20 h at each temperature as shown in Figure 10.2.

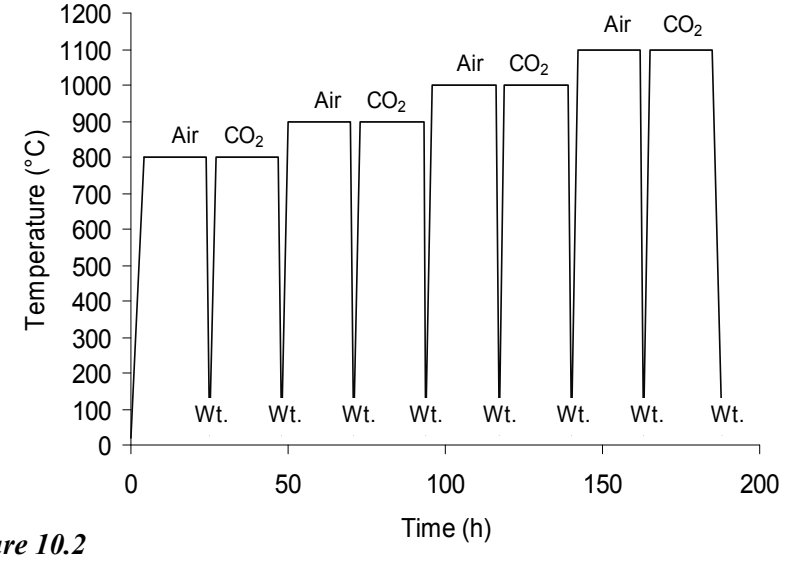

Figure 10.2
Experimental procedure during testing of CAM10 in dry alternating air and CO_2 atmosphere. Holding time between gas shifts was 20h."Wt." indicates the weighing of the samples

The second series was similar to the first series except that the temperature was held constant at 1100 °C and the exposure time between the gas shifts was 43h as shown in Figure 10.3. In both series the samples were weighed after each gas shift by removing the samples from the furnace at elevated temperatures (300-500 °C), weighing and placing them back into the furnace for further exposure.

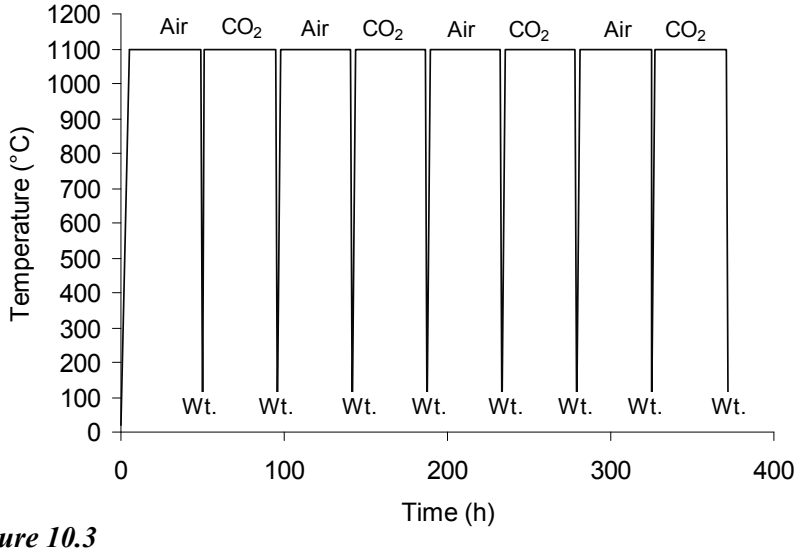

Figure 10.3
Experimental procedure during testing of CAM10 in dry alternating air and CO_2 atmospheres at 1100 °C. Holding time between gas shifts was 43h. "Wt." indicates the weighing of the samples

10.2.4 Crystallised CAM10 glass exposed to humid CO_2/air atmosphere

Crystallised CAM10 powder with particle diameter < 45 µm was heated in alternating wet CO_2 and wet air atmosphere in a similar series as shown in Figure 10.2. The test was performed in the temperature range 800-1100 °C. The start weight of the sample was 1.8885 g. The exposure time at each temperature was 20 h.

10.2.5 CAM10b and BLS glass exposed to humid CO_2

The influence of wet CO_2 atmosphere on CAM10b and BLS glass was studied by keeping the glass samples at temperatures in the range 800 to 1100 °C in wet CO_2. The particle diameter of the glass was in the range 45-150 µm and the exposure time varied between 8 and 105 h as given in Table 10.1 and illustrated in Figure 10.4.

Table 10.1
Experimental conditions in testing the influence of wet CO_2 gas on CAM10b and BLS glass powder at elevated temperatures.

Cycle	Sample	Type	Particle diamter (μm)	Temp. (°C)	Exp. time (h)
1	BLS	Glass	<150+45	800	21.2
	CAM10b	Glass	<150+45	800	21.2
2	BLS	Glass	<150+45	800	36.2
	CAM10b	Glass	<150+45	800	36.2
3	LN2	Glass	<150+45	900	21.2
	CAM10b	Glass	<150+45	900	21.2
4	BLS	Glass	<150+45	1000	8.1
	CAM10b	Glass	<150+45	1000	8.1
5	BLS	Glass	<150+45	1000	31.6
	CAM10b	Glass	<150+45	1000	31.6
6	BLS	Glass	<150+45	1100	62.0
	CAM10b	Glass	<150+45	1100	62.0
7	BLS	Glass	<150+45	1100	105.0
	CAM10b	Glass	<150+45	1100	105.0

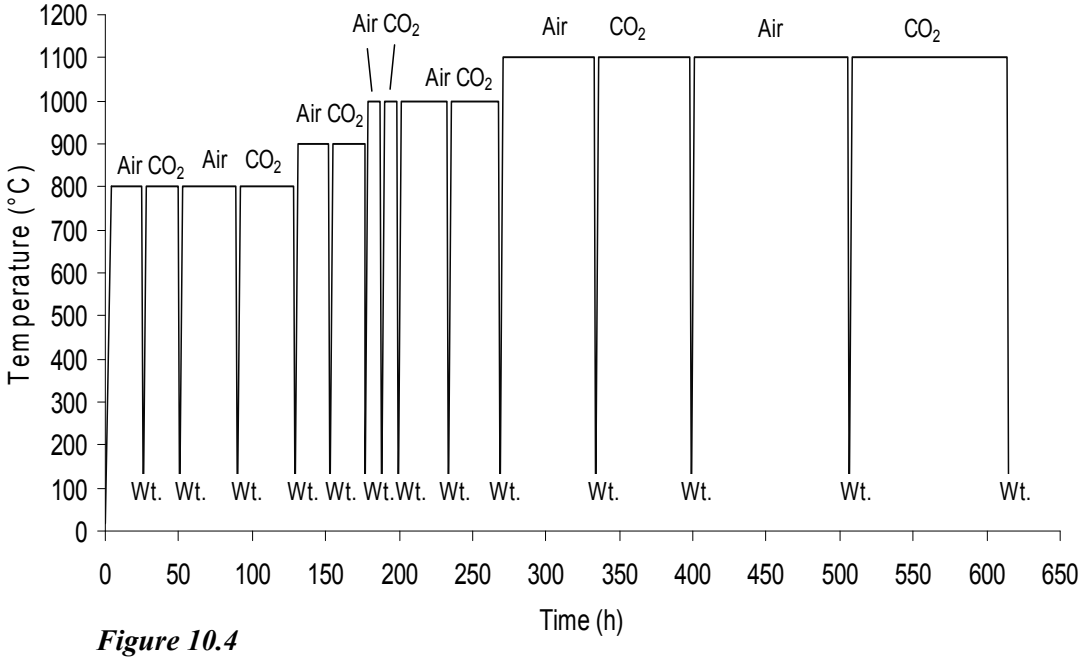

Figure 10.4
Experimental performance of gas exposure test of glassy BLS and CAM10b samples in humid atmosphere of CO_2/air

10.3 Results

10.3.1 CAM10 glass exposed to dry CO_2 and dry air

The glassy CAM10 exposed to dry CO_2 at 792 °C for 72 h increased in weight by 3.05 % while the crystalline sample showed a weight gain of only 0.29 %. By reheating the glassy sample in dry air at 1000 °C a weight loss of 2.48 % was measured corresponding to the weight gain of 3.05 %. X-ray diffraction of the samples after each cycle showed (Figure 10.5) that the weight gain of the glassy sample was due to $CaCO_3$ (calcite) formation and the weight loss was due to decomposition of the calcite according to equations 10.1 and 10.2. From these results it can be concluded that the glassy CAM10 reacts with CO_2 from the atmosphere at 792 °C forming $CaCO_3$ but at 1000 °C in air the calcite decomposes to CaO(s) and CO_2 (g). The XRD analysis of the crystalline CAM10 showed no calcite formation at 792 °C.

$$792\ °C:\ CaO(s) + CO_2(g) = CaCO_3(s) \qquad 10.1$$

$$1000\ °C:\ CaCO_3 = CaO(s) + CO_2(g) \qquad 10.2$$

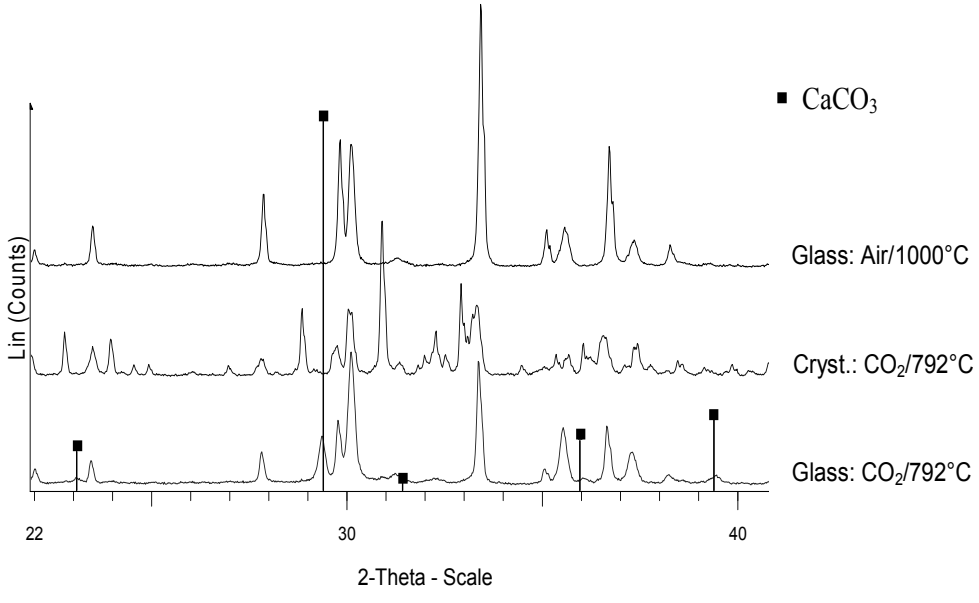

Figure 10.5
XRD pattern of glassy and crystalline CAM10 heated in CO_2 for 72 h at 792 °C and of the glassy sample reheated at 1000 °C, for 20 h in air. The calcite phase identification is based on PDF-file 1-072-1214 [135]

The reaction between glassy CAM10 and CO_2 was confirmed in the series where CAM10 glass with particle size < 45 μm was heated alternatively in dry CO_2 and dry air in the temperature range 800-1100 °C for 20 h at each temperature as shown in Figure 10.6. The weight gain in the first heating in CO_2 was lower than in the following heating cycles. The weight after heating in air is also lower than the start weight indicating that some strongly bound water (water that did not evaporate at 110 °C) has been present in the sample. The weight gain in CO_2 atmosphere is typically 0.7 % in all cycles following the first, and the weight gain/weight loss is reversible in the temperature range tested. Since the weight was not recorded continuously the results does not tell how fast the calcite formation proceeded.

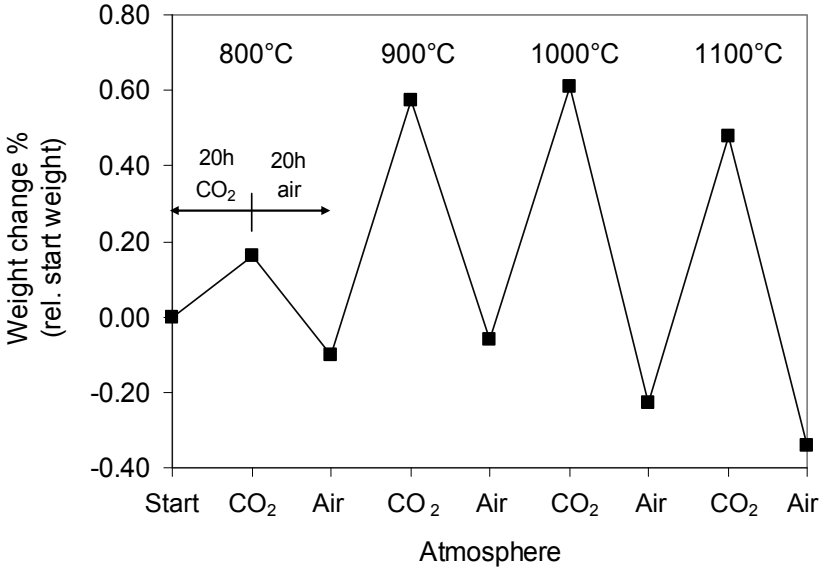

Figure 10.6
Weight change for CAM10 glass heated in alternating dry CO_2 and dry air for 20 h at temperatures between 800 and 1100 °C. Carbonate formation and decomposition is reversible in the temperature range 800-1100 °C

To get an idea of the kinetics of the calcite formation the effect of increasing exposure time to dry CO_2 and dry air at 1100 °C on the weight change of CAM10 glass is shown in Figure 10.7. In this case the sample was exposed 43 h in each atmosphere. The increased exposure time did not result in increased weight gain in CO_2 atmosphere demonstrating that the calcite formation is faster than 20 h, probably much faster. It is also found that even after 5 heating cycles representing a total time at 1100 °C of 215 h the CAM10 "glass" still reacts with CO_2 although it would be crystalline after the first cycle.

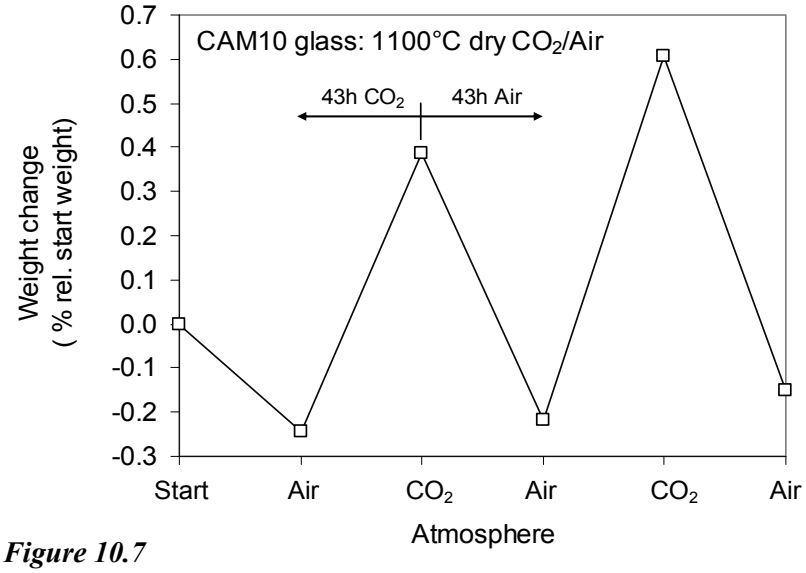

Figure 10.7
Weight change of CAM10 glass at 1100 °C in alternating dry air and dry CO_2 atmosphere with exposure time 43 h. The weight gain in CO_2 is typically 0.7 % as with exposure time 20 h

10.3.2 Crystallised CAM10 in humid CO_2/air atmosphere

The weight change of crystallised CAM10 in alternating humid CO_2/air atmosphere was much smaller than the weight change for CAM10 glass as given in Table 10.2 and shown in Figure 10.8. A small increase in weight in CO_2 atmosphere compared to air was observed, but for some of the measurements the weight change was within the experimental error. At 1100 °C in air, the weight was lower than the start weight.

Table 10.2
Weight change of crystallised CAM10 in alternating humid CO_2/air atmosphere in the temperature range 800-1100 °C. The water temperature was 41 °C

Temp (°C)	Weight change (g)	Weight change (%)	Atm.
20		0.00	Air
800	0.0011	0.06	CO_2
800	0.0000	0.00	Air
900	0.0004	0.02	CO_2
900	0.0009	0.05	Air
1000	0.0029	0.15	CO_2
1000	0.0001	0.01	Air
1100	0.0006	0.03	CO_2
1100	-0.0020	-0.11	Air

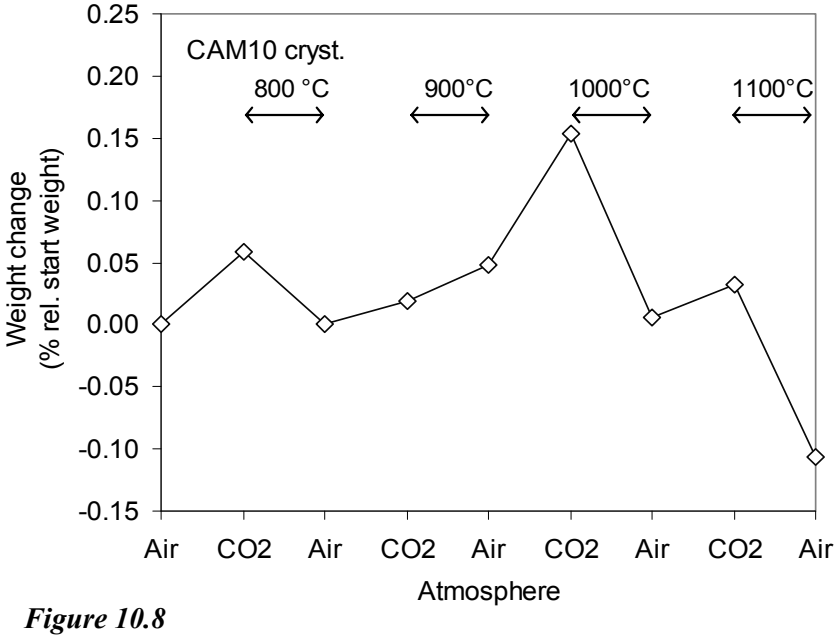

Figure 10.8
Weight change of crystallised CAM10 in alternating humid CO_2/air atmosphere in the temperature range 800-1100 °C

10.3.3 CAM10b and BLS in humid CO_2

The weight change of CAM10b in humid CO_2 was in the same order of magnitude as in dry CO_2 as demonstrated in Figure 10.9 and Table 10.3. The scatter in measurements at 800, 1000 and 1100 °C, where two measurements were performed, was probably due to experimental error.

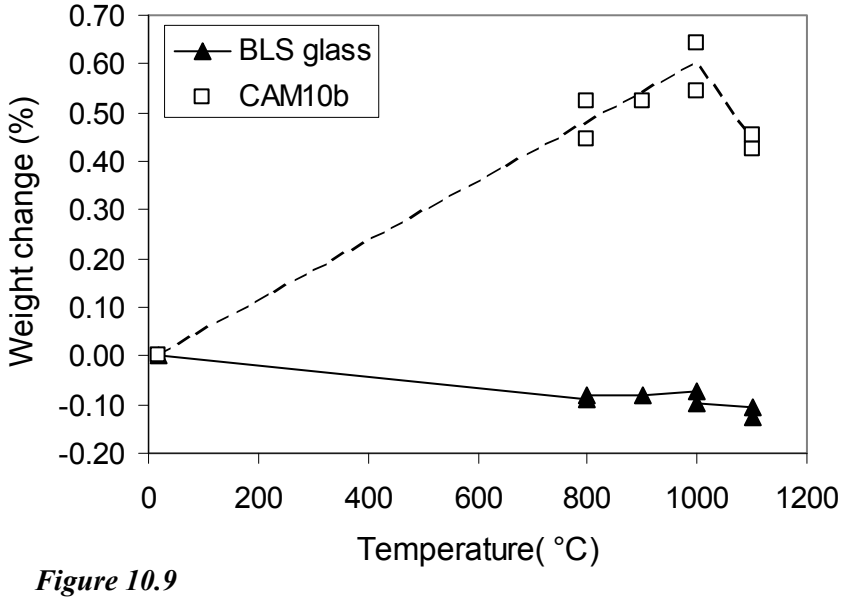

Figure 10.9
Weight change of CAM10b glass and BLS glass by heating in wet CO_2 in the temperature range 800-1100 °C

Table 10.3
Weight change of CAM10b glass and BLS glass by heating in wet CO_2 in the temperature range 800-1100 °C

Temp. (°C)	Exp. time (h)	Weight change %	
		BLS glass	CAM10b glass
20	0	0.00	0.00
800	25	-0.09	0.45
800	40	-0.08	0.52
900	64	-0.08	0.52
1000	76	-0.07	0.64
1000	115	-0.10	0.55
1100	183	-0.11	0.42
1100	231	-0.12	0.45

The weight gain for CAM10b passes a maximum of 0.50-0.60 % around 900-1000 °C. For the BLS glass the picture is different. BLS however, looses weight at all temperatures but the weight loss is almost negligible between 800 and 1100 °C. The weight loss between 20 and 800 °C is probably due to water that was not removed during drying of the powder at 110 °C prior to the test. The BLS glass is regarded as stable under the conditions in the present test.

10.4 Discussion

The weight gain when CAM10 glass is heated in CO_2 atmosphere is typically in the range 0.6-0.7 % when the CO_2 flow was kept at 3 Nl/h. However a larger weight gain of 3.05 % was observed during the first cycle where a high CO_2 flow was used. This shows that the CO_2 pressure is of importance and since high temperature reactor systems are likely to be pressurized (20-30 bar) the influence of CO_2 at high pressures should also be evaluated. Another issue is the difference between glassy and crystalline CAM10 regarding CO_2 affinity. The glassy CAM10 forms much more calcite in CO_2 atmosphere than the crystalline seal material. At repeated heating to 1100 °C, the "glassy" material continues to react with CO_2 even if the original glassy material had become crystalline. This can be explained by a surface effect where the surface must have another structure when glassy material is heated in CO_2 compared with the crystalline material and that this surface change is permanent. In a real system the sealing procedure will be performed in air or inert atmosphere. After the seal has been established it will be fully crystalline and therefore more stable when exposed to CO_2 compared to the corresponding glassy seal.

10.5 Conclusion

It has been demonstrated that crystallised CAM10 seal is stable in both dry and wet CO_2 atmospheres. The glassy CAM10 material reacts with CO_2 and forms calcite. The calcite decomposes when the material is reheated in air. The process "calcite formation/calcite decomposition" is reversible even at 1100 °C after the seal material has become crystalline. This shows that the seal should be fully crystalline before it is exposed to CO_2 atmosphere. The BLS seal glass was stable in humid CO_2 atmosphere at ambient pressure.

11 Discussion

11.1 General seal development procedure

When developing rigid solid glass ceramic seals for specific applications some general development steps should be followed (see Figure 11.1). To make the seal development as simple as possible, the membrane device should be designed to minimise the demand for seals and mechanical stresses on the seal joints. When the membrane assembly (membrane and electrolyte) and interconnect materials have been chosen, the seal composition can be designed. By consulting relevant phase diagrams the main seal composition(s) can be decided. The seal composition has to be prepared and designed with respect to thermal expansion, sintering properties and stability in reducing and oxidizing humid atmospheres at relevant temperatures.

The present work has revealed the importance of secondary phase formation during the sealing procedure. Even though there is a perfect thermal expansion match between the crystallised seal and the membrane/electrode assembly, secondary phases formed at the reaction interface between the seal and the joining materials can have completely different thermal expansion and give rise to fracture. The number of secondary phases is determined by the phase rule and the number of components in the system.

The seal glass systems usually consist of 3 to 4 oxides and the membranes usually consist of 2 or 3 oxides bringing the total up to 5-7 oxide components. The number of secondary phases will be in the same order demonstrating the complexity of glass ceramic seal development. Due to the chemical complexity it is in most cases necessary to identify the secondary phases that are formed and to characterize them at least with respect to thermal expansion. The best way to study the secondary phases is by sintering powder mixtures of the relevant materials (seal, membrane, support, electrode, interconnect) and fire at high temperatures (200-300 °C above the normal operational temperature). Normally the sintered mixtures have to be milled and fired again 2-4 times to reach the equilibrium state for the system. XRD, EMPA, SEM and optical microscopy are useful methods to identify the different crystalline phases and microstructure. The seal joint formation and the kinetics (diffusion rate) of the reactions taking place are best studied by making diffusion couples that should be heat treated at several temperatures and with different soak times. Diffusion couples will not only reveal the composition of the secondary phases and where they are formed, but flaws and microcracks give information about the TEC compatibility. If unwanted secondary phases are formed, suggestions for improvement have to be considered. Improvements can be obtained by modifying the design, sealing procedure, seal thickness, chemical

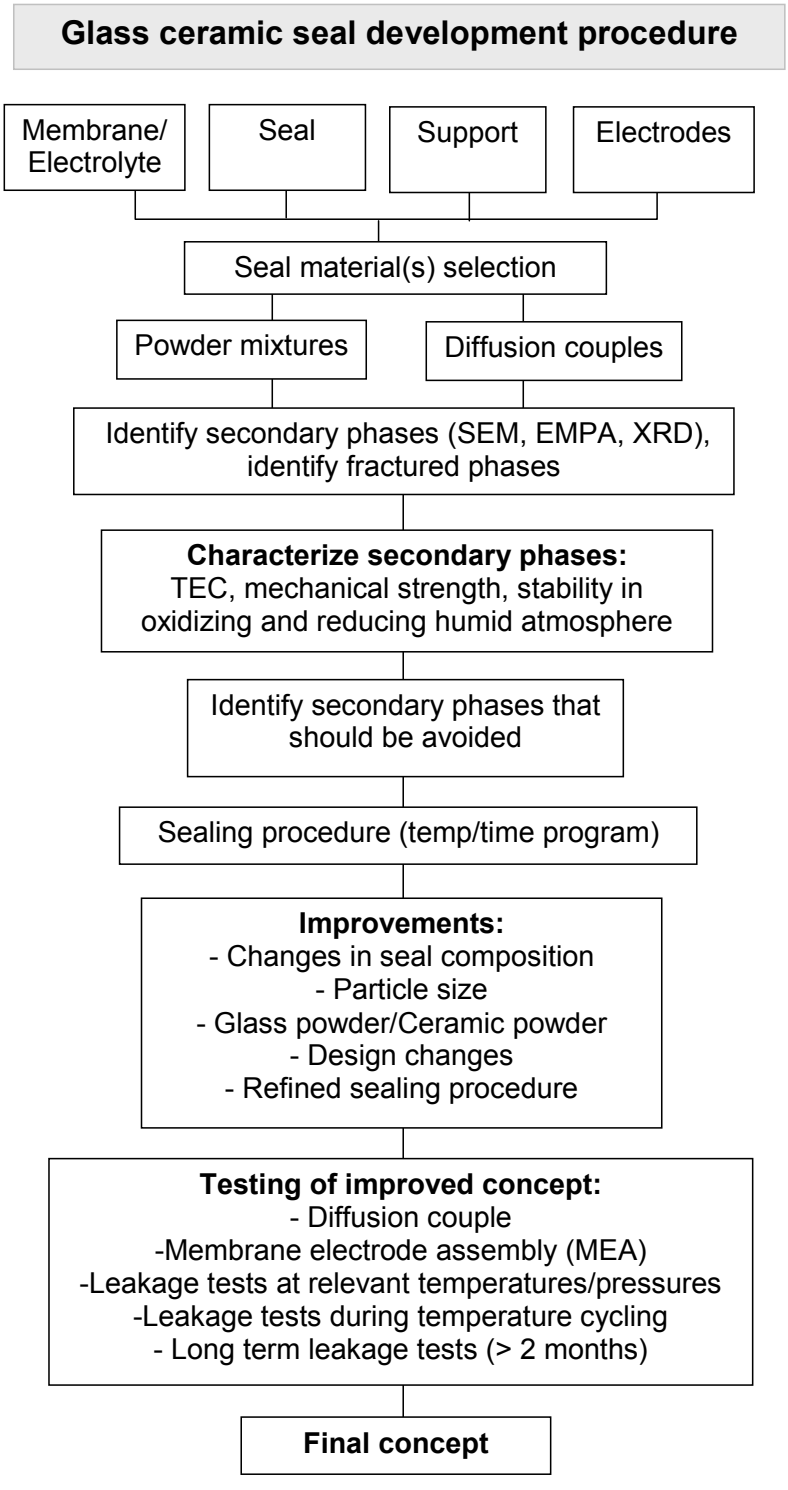

Figure 11.1
General procedure for development of rigid bonded seals for high temperature applications based on glass or ceramic powders

composition, particle size of the seal powder and if the seal powder should be glassy or ceramic. When changes have been made the improved seal concept has to be tested again until a dense seal without flaws can be prepared. The final functional test should be a leakage test of a complete assembly under realistic conditions regarding temperature, temperature cycling and atmosphere.

11.2 Glassy or crystalline seal material?

In the present work the seals have been prepared as glassy material that is being crystallised during the sealing procedure. It is obvious that the best would be to have a seal with a few % glassy phase, making the seal resilient and capable to eliminate mechanical stresses by plastic flow. This could be achieved by designing a glass ceramic seal with T_g below the operating temperature for the device and T_s above the operating temperature. Unfortunately this is difficult to obtain in a real system. All glasses will tend to crystallise given the right temperature and enough time. Depending on the glass composition most glassy systems will be completely crystalline after a few hours, days or weeks [152] if they are kept at typical operational temperatures for SOFC and HT membrane reactors (800-1000 °C). So why not start with a fully crystalline seal material and avoid the extra step of preparing a glass?

Melting the raw material batch to a glass followed by milling is a convenient way to obtain a homogeneous sealing powder. Glass can be readily sintered by heating the assembly to be sealed fast up to the proper temperature for the specific seal glass composition. After a short time, just long enough for the seal to become dense, the temperature is lowered to optimum temperature for crystallization to occur. The linear shrinkage, $\Delta L/L_{0,}$ of glassy material (viscous flow sintering) with initial particle diameter d is given by the Frenkel equation as [149]:

$$\frac{\Delta L}{L_0} = \frac{1.5\gamma_s t}{\eta d} \qquad 11.1$$

Where η is the viscosity and γ_s is the surface tension and t is the time. Equation 11.1 shows that by reducing the particle size from 10μm to 0.1 μm the sintering time can be reduced by a factor of 100. One challenge by using glassy powder is to avoid large gas bubbles caused by entrapped air when the pores between the glass particles are closing. Due to plastic flow of the viscous glass melt big bubbles that can weaken the seal substantially can be formed. Bubbles can be avoided by performing the sealing cycle in vacuum.

Gas bubbles can also be formed because of chemical reactions that change the gas solubility in the glass.

A ceramic seal material can be more difficult to sinter if no intermediate liquid phases are formed and might need more time at higher temperature than a glassy material to obtain a fully dense seal. In this case the sintering is ruled by the laws of solid state sintering where different diffusion mechanisms are dominating the densification process. Generally the linear shrinkage for solid state sintering can be expressed as [149]:

$$\frac{\Delta L}{L_0} = \left[\frac{K D_v \gamma_s V_v t}{k_B T d^n} \right]^m \qquad 11.2$$

Here D_v is the apparent diffusivity of vacancies of volume V_v, d is the grain diameter, K is a constant dependent on the geometry, T the temperature, t is the time and m and n are constants. Commonly n is observed to be approximately 3, which implies that lattice diffusion is the dominant densification mechanism, and m is commonly in the range 0.3-0.5 [149]. The time at the sintering temperature (usually higher than the operating temperature for the system) should be as short as possible in order to avoid too extensive reaction between the seal and the sealed materials. The sintering time for a ceramic powder can be shortened effectively by reducing the particle size. Since the densification time during solid state sintering of a ceramic powder with particle diameter d is approximately proportional to d^3 (equation 11.2), a reduction of the particle size from 10μm to 1 μm will reduce the sintering time by an order of 10^3. This shows that short sintering times can be achieved also with ceramic seal materials. By using a submicron powder eventually closed pores will have a size smaller than the particles and will not have any negative effect on the strength of the sintered seal. An efficient method to reduce the sintering temperature is to bring the sintering from a solid state sintering regime to a liquid state sintering regime by small additions of a material that forms low melting compounds.

A complete submicron ceramic powder included the sintering aids can be prepared by several methods such as sol gel, spray drying or spray pyrolysis, which all are well established methods for powder synthesis. By starting with a submicron ceramic powder, a dense and gas tight seal can be established just as fast as with glassy powder but the extension of the reaction between the seal and the sealed materials will probably be less compared to glass resulting in a better and more durable seal.

11.3 Suggestions for further work

The focus in the present work has been on reactions between the seal materials and the membrane/support materials. The seal performance in realistic environments and optimisation of the sealing cycle, have not been sufficiently evaluated. Suggestions for the further work are:

a) Testing of seal stability in reducing dry and wet atmospheres ($P_{O2} < 10^{-12}$ atm.) at normal pressure and high pressure (20 bar).

b) Optimizing sealing procedure for BLS seal to reduce the extent of $Ba_2La_8Si_6O_{26}$ formation. Compare glassy powder and ceramic powder sealing.

c) Evaluate means of increasing the TEC of aluminate glass system by enhancing crystalline phases with high thermal expansion.

The leakage test revealed weaknesses with the flux test equipment. The apparatus should be modified so that leakage through the gold seal can be controlled. The gas analysis should also be improved so that reliable analysis of relevant gases can be performed in the low concentration region < 0.001 mol %.

12 Conclusions

12.1 Aluminate glass properties

In the present work a series of aluminate glasses denoted CAMx with the general composition (molar basis): 52.7-XCaO·XMgO·37.3Al_2O_3 (0<x<18) has been evaluated with respect to HT sealing applications for SOFSs and HT membrane reactors. By quenching aluminate glass melts from 1550 °C on a copper plate, batches of 40-60 g of glass could be made. DSC analysis showed that the aluminate glasses had glass transition temperatures T_g, in the range 841-794 °C as the MgO content increased from 0 to 18 mol %. The corresponding crystallization temperature T_x was in the range 940-915 °C. The dilatometric softening point measured by dilatometry was in the range 859-820 °C. The thermal expansion coefficients for the glasses in the temperature range 20-700 °C varied from 5.8-8.1·10^{-6} $°C^{-1}$. The maximum TEC for the glassy material was observed for compositions with 10-13 mol % MgO. The TEC of crystallised glass with 8.9 mol % MgO was 7.6·10^{-6} $°C^{-1}$ in the range 20-1000 °C. Exposure of the aluminate glasses to water at room temperature showed that the glasses reacted with water. Exposure of the glass with ~9 mol % MgO to humid and dry CO_2 at elevated temperatures (800-1100 °C) showed that the glass formed $CaCO_3$, while the

crystallised material showed no signs of calcite formation. This demonstrates that the crystalline material should perform well as a high temperature seal exposed to CO_2.

12.2 Aluminate glass as seal for $LaNbO_4$

The TEC of the aluminate glass CAM10 is compatible to the TEC of $LaNbO_4$ and the glass is a candidate as sealing material for $LaNbO_4$ PCFCs. One challenge of sealing $LaNbO_4$ is the phase transition of $LaNbO_4$ at ~ 530 °C where there is an abrupt decrease in the thermal expansion coefficient from $13.3 \cdot 10^{-6}$ $°C^{-1}$ to $6.7 \cdot 10^{-6}$ $°C^{-1}$.

Diffusion couples of aluminate glass and $LaNbO_4$ showed that a solid and dense bond was formed between the two materials, which is crucial in order to make a good seal. Leakage testing of the seal in a "seal-membrane-support assembly" consisting of $LaNbO_4$ membrane, aluminate glass seal and alumina substrate showed no significant leaks during testing at 1060-900 °C confirming that the aluminate seal is a promising candidate as seal for $LaNbO_4$ PCFCs. The seal remained gas tight after one thermal cycle down to room temperature.

12.3 Ba-La-silicate (BLS) seal for La_2NiO_4

The Ba-La-silicate glass (BLS) with the molar composition $31.3BaO \cdot 6.5La_2O_3 \cdot 2.1SiO_2$, evaluated as seal material for La_2NiO_4 membranes, had a glass transition temperature T_g at 760 °C (DSC-analysis) and crystallization onset at 924 °C. The dilatometric softening point was 856 °C and the thermal expansion coefficient of the crystallised BLS glass was measured to $12.8 \cdot 10^{-6}$ $°C^{-1}$ between 20 and 1000 °C. The DSC analysis showed that this seal material will become completely crystalline after short time at the expected operational temperature of 900-1000 °C. Exposure of the BLS seal glass to CO_2 and H_2O at elevated temperatures (800-1100 °C) showed good stability.

Diffusion couples of BLS glass and La_2NiO_4 showed good bonding performance and that BLS is a seal material candidate for La_2NiO_4. One challenge with the tested BLS composition is that the secondary phase $Ba_2La_8Si_6O_{26}$ that is formed in the reaction zone close to the membrane has a much lower TEC ($8.5 \cdot 10^{-6}$ $°C^{-1}$ in the range 20-1200 °C) than the membrane and the other related silicate crystalline phases. The TEC mismatch resulted in crack formation parallel to the membrane surface caused by high compressive stress. This problem can probably be solved either by refining the temperature cycle for the sealing process or by making small changes in the chemical composition of the seal material. Secondary

phases with a strong mismatch in TEC compared to the rest of the phases in the seal/membrane system should be avoided. Leakage test showed that the present system had a small leakage due to the fractures along the seal.

13 References

1 N. Q. Minh
Ceramic Fuel Cells
J. Am. Ceram Soc. 76(1993) 563-588

2 S. M. Haile
Fuel Cell materials and components
Acta Materialia 51 (2003) 5981-6000

3 A. B. Stambouli, E. Traversa
Solid Oxide Fuel Cells (SOFCs): A review of an environmentally clean and efficient source of energy
Renewable and sustainable Energy Reviews 6 (2002) 433-455

4 R.M. Ormerod
Solid oxide fuel cells
Chem. Soc. Rev. 32 (2003) 17-28

5 P. Singh, N. Q. Minh
Solid Oxide Fuel Cells: Technology Status
Applied Ceramic Technology 1 (2004) 5-15

6 S.C. Singhal
Advances in solid oxide fuel cell technology
Solid State Ionics 135 (2000)305-313

7 N. Q. Minh
Solid oxide fuel cell technology - features and applications
Solid State Ionics 174(2004)271-277

8 S.P.S. Badwal, K. Foger
Solid Oxide Fuel Cell Review
Ceramic International22 (1996) 257-265

9 R. Bredesen, K. Jordal, O. Bolland.
High-temperature membranes in power generation with CO_2 capture.
Chemical engineering and processing 43 (2004) 1129-1158

10 J. B. Smith
Mixed oxygen ion/electron conductors for oxygen separation processes: Surface kinetics and cation diffusion
PhD-thesis UiO (2005)

11 T. Mokkelbost, Ø. Andersen, R.A. Strøm et al.
High-Temperature Proton-Conducting $LaNbO_4$-Based materials: Powder Synthesis by Spray Pyrolysis
J. Am. Ceram. Soc.90 (2007)3395-3400

12 W.Z. Zhu, S.C. Deevi
A review on the status of anode materials for solid oxide fuel cells
Mat. Science and Engineering A362 (2003) 228-239

13 S. P .Jiang, S. H. Chan
A review of anode materials development in solid oxide fuel cells
J. of Material Science 39 (2004) 4405-4439

14 A.F. Sammels, M.V. Mundschau
Nanoporous Inorganic Membranes for chemical processing
Wiley -VCH Verlag GmbH & Co. KGaA (2006)
15 I. Hiroyasu, Y. Asakura, K. KatahiraProspect for hydrogen technology using proton-conducting ceramics
Solid State Ionics 168 (2004) 299-310
16 B.C.H. Steele
Ceramic ion conducting membranes
Current Opinion in Solid State and Materials Science 1 (1996) 684-691
17 J. Vente, W.G. Haije, Z.S. Rak
Performance of functional perovskite membranes for oxygen production
J. of Membrane Science 276 (2006) 178-184
18 K.Wiik, S. Aasland, H.L. Hansen et al.
Oxygen permeation in the system $SrFeO_{3-x}$-$SrCoO_{3-y}$
Solid State Ionics 152-153 (2002) 675-680
19 V.V. Kharton, F.M.B. Marques, A. Atkinson
Transport properties of solid oxide electrolyte ceramics: a brief review
Solid State Ionics 174 (2004) 135-149
20 K. Sundmacher, L.K. Rihko-Struckmann, V. Galvita
Solid Electrolyte reactors: Status and trends
Catalysis Today 104 (2005) 185-199
21 S. Gopalan
Using mixed ionic and electronic conductors for gas separation
JOM May (2002) 26-29
22 L.-W. Tai, M.M. Nasrallah, H.U. Anderson et al.
Structure and electrical properties of $La_{1-x}Sr_xCo_{1-y}Fe_yO_3$ Part 1
The system $La_{0.8}Sr_{0.2}Co_{1-y}Fe_yO_3$
Solid State Ionics 76 (1995) 259-271
23 L.-W. Tai, M.M. Nasrallah, H.U. Anderson et al.
Structure and electrical properties of $La_{1-x}Sr_xCo_{1-y}Fe_yO_3$ Part 2
The system $La_{1-x}Sr_xCo_{0.2}Fe_{0.8}O_3$
Solid State Ionics 76 (1995) 273-283
24 A. Amov, S.J. Skinner
Recent developments in Ruddlesden-Popper nickelate systems for solid oxide fuel cell cathodes
J. of Solid State Electrochemistry 10 (2006) 538-546
25 A.V. Kovalevsky, Y.V. Pivak, A.A. Markov et al.
Oxygen permeability, stability and electrochemical behaviour of $Pr_2NiO_{4+\delta}$-based materials
J. of Electroceramics 18 (2007) 205-218

26 M. Grennblatt
Ruddlesden-Popper $L_{n+1}Ni_nO_{3n+1}$
Current Opinion in Solid State and Mat. Sci. 2 (1997) 174-183
27 V.V. Vashook, I.I. Yushkevich, L.V. Kokhanovsky et al.
Composition and conductivity of some nickelates
Solid State Ionics 119 (1999) 23-30
28 F.M. Figueiredo, M.R. Soares, V.V. Kharton et al.
Properties of $CaTi_{1-x}Fe_xO_{3-\delta}$ Ceramic Membranes
J. of Electroceramics 13 (2004) 627-636
29 S. Marion, A.I. Becerro, T. Norby
Ionic and electronic Conductivity in $CaTi_{1-x}Fe_xO_{3-\delta}$
Ionics 5(1999)385-392
30 J.W. Phair, S.P.S. Badwal
Review of proton conductors for hydrogen separation
Ionics 12 (2006) 103-115
31 U. Blachandran, B. Ma, J. Guan et al.
Mixed-conducting Dense Ceramics for Gas Separation applications
Proc. of Symp. on Solid State Ionic Devices 195th Meeting of The electrochemical Society, May 1999
32 S.J. Skinner
Recent advances in perovskite-type materials for SOFC cathodes
Fuel Cells Bulletin 4 (2001) 6-12
33 Planar design SOFC with cross flow
http://www.doitpoms.ac.uk/tlplib/fuel-cells/high_temp_sofc.php
34 E. Konysheva, H. Penkalla, E. Wessel et al.
Chromium Poisoning of Perovskite Cathodes by the ODS Alloy Cr5Fe1Y_2O_3 and the high Chromium Ferritic Steel Crofer22APU
J. of the Electrochemical Society 153 (2006) A765-A773
35 Siemens Power Generation-SFC System Fabrication
http://www.powergeneration.siemens.com
36 P.A. Lessing
A review of sealing technologies applicable to solid oxide electrolysis cells
J. of the Electrochemical Society 42 (2007) 3465-3476
37 K.S. Weil
The State-of-the-art in Sealing Technology for Solid Oxide Fuel Cells
JOM August (2006) 37-44
38 P.H. Larsen, P.F. James
Chemical stability of MgO/CaO/Cr_2O_3-Al_2O_3-B_2O_3-phosphate glasses in solid oxide fuel cell environment
J. of Materials Science 33 (1998) 2499-2507

39 P.H. Larsen, F.W. Poulsen, R.W Berg
The influence of SiO_2 addition to $MgO\text{-}Al_2O_3\text{-}3.3P_2O_5$ glass
Journal of Non-Crystalline Solids 244 (1999) 16-24

40 S. Faaland, M-A Einarsrud, T. Grande
Reactions between Calcium- and Strontium-Substituted Lanthanum Cobaltite Ceramic membranes and Calcium Silicate sealing
Materials Chemistry of Materials 13 (2001) 423-732

41 I. Kaus, K. Wiik, M. Dahle et al.
Stability of $SrFeO_3$ based materials in presence of SiO_x species in humid atmosphere at high temperatures and pressures
J. of Eur. Ceram. Soc. 27 (2007) 4509-4514

42 M.-C. Cheng, I. B. Cutler
Vaporization of Silica in Steam Atmosphere
J. Am. Ceram. Soc. 62 (1979) 593-596

43 H.E. Eaton, G.D. Linsey
Accelerated oxidation of SiC CMC's by water vapour and protection via environmental barrier coating approach
J. of European Ceramic Society 22 (2002) 2741-2747

44 E. Opila, D. S. Fox, N. S. Jacobson
Mass spectrometric identification of Si-O-H(g) species from the reaction of silica with water vapour at atmospheric pressure
Am. Ceram. Soc. 80 (1997)1009-1012

45 I. Kaus, K. Wiik, B. Krogh, et al.
Stability of $SrFeO_3$-based materials in H_2O/CO_2-containg atmospheres at high temperatures and pressures
J. Am. Ceram. Soc. 90 (2007) 2226-2230

46 B De Jong, J.W. Adams, B.G. Aitken, G.J. Fine
Glass Ceramics
Ullmann's encyclopaedia of industrial chemistry 6th ed., Wiley 2003
6 (15) (2003) 627-643

47 J. E. Shelby
Introduction to glass science and technology
Royal Society of Chemistry (RSC)- Paperbacks (1997)

48 E. S. Shepard and G. A. Rankin
The binary system with Alumina and Silica, Lime and Magnesia
American J. of Science 28 (1909) 293-333

49 D.R. Uhlmann
Glass formation, a contemporary view.
J. Am. Ceram Soc. 66 (1983)95-100

50 M. Budd
Barium Lanthanum Silicate Glass Ceramics
US patent no. 2005/130823 A1 (2005)

51 L.Blum, H.-P. Buchkremer, S. Gross et al
Solid Oxide Fuel Cell Development at Forschungszentrum Jülich
Fuel Cells 7 (2007) 204-210
52 F. Tietz
Thermal expansion of SOFC Materials
Ionics 5 (1999) 129-139
53 Y.S. Touloukian, R.K. Kirby, R.E.Taylor et al.
Thermal expansion nonmetallic solids
Thermophysical properties of matter 13 (1970) -79
54 Thermal expansion Crofer 22APU
Data sheet No 4046 December 2006
ThyssenKrupp VDM
55 Thermal expansion of Avesta 253MA high temperature resistant alloy
Valbruna Nordic, UNS S30815-253MA
56 W. D. Kingery, H. K. Bowen, D. R. Uhlmann
Introduction to ceramics
John Wiley & Sons NY (1976)
57 A. Flügel, M.D. Dolan, A.K. Varshneya et al.
Development of an improved Devirtifiable Fuel Cell Sealing Glass I. Bulk properties
J. of the Electrochemical Society 154 (2007) B601-B608
58 C.W. Parmelee, C. G. Harman
Ceramic Glazes, third edition
Chaners Books (1973)
59 K.L. Ley, M. Krumpelt, R. Kumar et al.
Glass-ceramic sealants for solid oxide fuel cells: Part 1. Physical properties.
J. Mater. Res. 11 (1996) 1489-1493
60 K. Eichler, G. Solow, P. Otschik et al.
BAS ($BaO{\cdot}Al_2O_3{\cdot}SiO_2$)-glasses for High Temperature Applications.
J. of Eur. Ceram. Soc.19 (1999) 1101-1104
61 S. Taniguchi, M. Kadowaki, T. Yasuo et al.
Improvement of thermal cycle characteristics of planar-type solid oxide fuel cell by using ceramic fibre as sealing material
J. of Power Sources 90(2000) 163-169
62 X. Qi, F.T. Akin, Y.S. Lin.
Ceramic-glass composite high temperature seals for dense ionic-conducting ceramic membranes.
J. of Membrane Sci. 193 (2001) 185-193
63 S.-B. Sohn, S.-Y. Choi, G.-H. Kim et al.
Stable sealing glass for planar solid oxide fuel cell
J. of Non-Crystalline Solids 297 (2002) 103-112

64 S.-B. Sohn, S.-Y. Choi, G.-H. Kim et al.
Suitable Glass-ceramic Sealant for Planar Solid-Oxide Fuel Cells
J. Am. Ceram. Soc. 87 (2004) 254-260

65 K. D. Meinhardt, J. D. Vienna, T. R. Armstrong et al.
Glass-ceramic joint and method of joining
US patent nr. 6532 769B1 (2003)

66 M. Brochu, B.D. Gauntt, R. Shah, et al.
Comparison between barium and strontium-glass composites for sealing SOFCs
J. Eur. Ceram. Soc. 26 (2006) 3307-3313

67 P. Jinhua, S. Kening, Z. Naiquing, et al.
Sealing Glass of Barium-Aluminiumsilicate system for Solid Oxide Fuel Cells
J. of Rare Earth 25 (2007) 434-438

68 N.P. Bansal, E. A. Gamble.
Crystallization Kinetics of a Solid Oxide Fuel Cell Seal Glass by Differential Thermal Analysis.
J. of. Power Sources 147 (2005) 107-115

69 Z. Yang, J.W. Stevenson, K.D. Meinhardt. Chemical interactions of barium-calcium-aluminosilicate based sealing glasses with oxidation resistant alloys.
Solid State Ionics 160 (2003) 213-225

70 Z.Yang, G. Xia, K.D. Meinhardt et al.
Chemical stability of glass seal interefaces in intermediate Solid Oxide Fuel Cells
J. of Mat. Eng. and Performance, 13 (2004) 327-334

71 K.D. Meinhardt, D.-S. Kim, Y.-S. Chaou et al.
Synthesis and properties of a barium aluminosilicate solid oxide fuel cell glass-ceramic sealant
J. of Power Sources 182 (2008) 188-198

72 R. Zheng, S.R. Wang, H.W. Nie et al.
SiO_2-CaO-B_2O_3-Al_2O_3 ceramic glaze as sealant for planar ITSOFC
J. of Power Sources 128 (2004) 165-172

73 Y-S Chou, J. W. Stevenson, R. N. Gow
Novel alkaline earth silicate sealing glass for SOFC. Part I. The effect of nickel oxide on the thermal and mechanical properties
J. of. Power Sources 168 (2007) 426-433

74 Y-S Chou, J.W. Stevenson, R.N. Gow
Novel alkaline earth silicate glass for SOFC Part II. Sealing and Interfacial microstructure
J. of. Power Sources 170 (2007) 395-400

75 V. Kumar, A. Arora, O.P. Pandey et al.
Studies on thermal and structural properties of glasses as sealants for solid oxide fuel cells
Int. J. of Hydr. Energy 33 (2008) 434-438

76 V.A.C Haanappel, V. Shemet, I.C. Vinke et al.
A novel method to evaluate the suitability of glass sealant-alloy combinations under SOFC stack conditions
J. of Power Sources 141 (2005) 102-107

77 S. M. Gross, T. Koppitz, J. Remmel et al.
Glass-Ceramic Materials of the system BaO-CaO-SiO_2 as sealants for SOFC applications.ACS:
Ceramic Engineering and Science Proceedings.
Advances in Solid Oxide Fuel Cells (2005) 239-245

78 K.A. Nielsen, M. Solvang, F.W. Poulsen et al.
Evaluation of sodium aluminosilicate glass composite seal with magnesia filler
Ceramic Engineering and Science Proceedings
Volume 25 issue 3, 2004. American Ceramic Society. 25 (2004)

79 C. Lara, M.J. Pascual, M.O. Prado et al.
Sintering of glasses in the system RO-Al_2O_3-BaO-SiO_2 (R=Ca, Mg, Zn) studied by hot stage microscopy
Solid State Ionics 170, (2004) 201-208

80 N.H. Mentzler, D. Sebold, M. Zahid et al.
Interaction of metallic SOFC interconnect materials with glass-ceramic sealant in various atmospheres
J. of. Power Sources 152 (2005) 156-167

81 X. Deng, J.Duquette, A. Petric
Silver-Glass Composite for High Temperature sealing
Int. J. Appl. Ceram. Technol.4 (2007) 145-151

82 C. Lara, M.J. Pascual, M.O Prado et al.
Electrical behaviour of glass-ceramics in the systems RO-BaO-SiO_2 (R=Mg, Zn) for sealing SOFCs.
J. of Power Sources 157 (2006) 377-384

83 I.W. Donald, B.L.Metcalfe, L.A. Gerrard
Interfacial Reactions in Glass-Ceramic-to-Metal Seals
J. Am. Ceram. Soc. 91 (2008) 715-720

84 C. Lara, M.J. Pascual, A. Durán
Glass-forming ability, sinterability and thermal properties in the System RO-BaO-SiO_2 (R=Mg,Zn)
J. of Non-Crystalline Solids 348 (2004) 149-155

85 N.H. Menzler, M. B. Ram, H.P. Buchkremer et al.
Development of gastight sealing material for ceramic components
J. of Eur. Ceram. Soc. 23 (2003) 445-454

86 T. Barry, G.S. Schajer, F. M. Stackpool
Glass seals for sealing beta-alumina in electro-chemical cells or other energy conversion devices, glasses for use in such seals and cells or other energy conversion devices with such seals.
US Patent 4291107 (1981)
87 K. D. Meinhardt, J. D. Vienna, T. R. Armstrong et al
Glass-ceramic material and method of making
US patent nr. 6430 966B1 (2002)
88 M. Budd
Method of Forming a Glass Ceramic Material
US patent no.6475938 B1 (2002)
89 J. G. Larsen et al. (Denmark)
High temperature sealing material
US patent no. 6 828 263 B2 (2004)
90 G. M. Crosbie
Glass compositions for ceramic electrolyte electrochemical conversion devices
US patent no. 6878651 B2.(2005)
91 Z. Yang, C. A. Coyle, S. Baskaran et al.
Gas-Tight Metal/Ceramic or Metal/Metal seals for applications in high temperature electrochemical devices and method of Making
US patent 6843406 B2 (2005)
92 C. Thompson, A. Wood, S. Pyke
Glass ceramic coatings and sealing arrangements and their use in fuel cells US patent no. 6656625 B1 (2003)
93 K.S. Weil, J.E. Deibler, J.S. Hardy et al.
Rupture testing as a tool for developing Planar Solid Oxide Fuel Cells Seals
J. of Mat. Eng. and Perf. 13 (2004) 316-326
94 R. N. Singh
High-Temperature Seals for Solid Oxide Fuel Cells (SOFC)
J. of Mat. Eng. and Perf. (2006) 422-426
95 R.E. Loehman, E. Corral, M. Chavez
Reliable Seals for Solid Oxide Fuel Cells
FY 2007 Annual Report IV.A.18(2007) 113-117
96 Y-S. Chou, J.W. Stevenson
Advanced mica based seal and methods for making and using
US patent US2004/0048137A1 (2004)
97 W. Vogel
Chemistry of Glass
The American Ceramic Society (1985)
98 H. G. Pfaender
Schott guide to glass
Chapman & Hall (1996)

99 C. T. Moynihan
Correlation between the Width of the Glass Transition Region and the temperature dependence of the viscosity of high-Tg glasses
J. Am. Ceram. Soc. 76 (1993) 1081-1087
100 H. Swift
Effect of magnesia and alumina on rate of crystal growth in some soda-lime-silica glasses
J. Am. Ceram. soc. 30 (1947) 170-174
101 W. Höland, G. Beall
Glass ceramic technology American Ceramic Society
(2002)
102 M.J. Pascual, A. Guillet, A. Durán
Optimazation of glass-ceramic sealant compositions in the system $MgO-BaO-SiO_2$ for solid oxide fuel cells (SOFC)
J. of. Power Sources 169 (2007) 40-46
103 N. Lahl, D. Bahadur, K. Singh et al.
Chemical interactions between aluminosilicate base sealants and the components on the anode side of solid oxide fuel cells.
J. of the Electrochemical Society 149 (2002) A607-A614
104 F. Smeacetto, M. Salvo, M. Ferraris et al.
Characterisation and performance of glass-ceramic sealant to join metallic interconnects to YSZ and anode-supported-electrolyte in planar SOFCs
J. Eur. Ceram. Soc. 28 (2008) 2521-2527
105 F. Wiener, M. Brown, H.P. Buchkremer
Chemical interaction between Crofer 22APU and mica-based gaskets under simulated SOFC conditions
J. Mat. Sci. 42 (2007) 2643-2651
106 P. Batfalsky, V.A.C Haanappel, J. Malzbender et al.
Chemical interaction between glass-ceramic sealants and interconnect steel in SOFC stacks
J. of Power Sources 155 (2006) 128-137
107 F. Smeacetto, M. Salvo, M. Ferraris et al.
Glass-ceramic seal to join Crofer 22APU alloy to YSZ ceramic in planar SOFCs
J. of Eur. Ceram. Soc. 28 (2008) 61-68
108 F. Smeacetto, M. Salvo, M. Ferraris et al.
Glass and composite seals for the joining of YSZ to metallic interconnect in solid oxide fuel cells
J. of Eur. Ceram. Soc. 28 (2008) 611-616
109 J. Y. Kim, J.S. Hardy, K.S. Weil
Novel Metal-Ceramic Joining for Planar SOFCs
J. of Electrochemical Society 152 (2005) J52-J58

110 K. S. Weil, C.A. Coyle, J. S. Hardy et al.
Alternative planar SOFC sealing concepts
Fuel Cells Bulletin 2005 (2005) 11-16
111 K.S. Weil, J.S. Hardy, B.J. Koeppel
New sealing Concept for planar Solid Oxide Fuel Cells
J. of Mat. Eng. and Perf. 15 (2006) 427-432
112 J. Duquette, A. Petric
Silver wire seal design for planar solid oxide fuel cell stack
J. of Power Sources 137 (2004) 71-75
113 J.W. Fergus
Sealants for solid oxide fuel cells (rewiev)
J. of. Power Sources 147 (2005) 156-167
114 S. Simner, J. W. Stevenson
Compressive mica seals for SOFC applications.
J. of Power Sources 102 (2001) 310-316
115 Y-S Chou, J. W. Stevenson, L.A. Chick
Ultra-low leak rate of hybrid compressive mica seals for solid oxide fuel cells
J. of Power Sources 112 (2002) 130-136
116 Y-S Chou, J.W. Stevenson
Thermal cycling and degradation mechanisms of compressive mica-based seals for solid oxide fuel cells.
Journal of Power Sources 112 (2002) 376-383
117 Y-S Chou, J. W. Stevenson
Phlogopite mica-based compressive seals for solid oxide fuel cells: effect of mica thickness.
J. of Power Sources 124 (2003) 473-478
118 Y-S Chou, J. W. Stevenson, L. A. Chick
Novel compressive Mica Seals with Metallic Interlayers for Solid Oxide Fuel Cell Applications.
J. Am. Ceram. soc. (2003) 1003-1007
119 Y.-S. Chou, J. W. Stevenson
III.A.10 SOFC Compressive Seal Development at PNNL Pacific North West National Laboratory annual report 2004 (2004)
120 Y.-S. Chou, J. W. Stevenson, P. Singh
Combined ageing and Thermal cycling of compressive mica seals for solid oxide fuel cells
ACS: Ceramic Engineering and Science proceedings. 29th Int. Conf. On advanced ceramics and composites (2005) 265-272
121 Y-S Chou, J.W. Stevenson
Mid-term stability of novel mica-based compressive seals for solid oxide fuel cells
J. of Power Sources 115 (2003) 274-278

122 Y.-S. Chou, J. W. Stevenson, P. Singh
Thermal cycle stability of a novel glass-mica composite seal for solid oxide fuel cells: Effect of glass volume fraction and stresses
J. of Power Sources 152 (2005) 168-174
123 Y-S Chou, J. W. Stevenson
Novel infiltrated Phlogopite mica compressive seals for solid oxide fuel cells.
J. of Power Sources 135 (2004) 72-78
124 A.H. De Aza, P. Pena, S. De Aza
Ternary System Al_2O_3-MgO-CaO: I Primary Phase Field of Crystallization of Spinel in Subsystem $MgAl_2O_4$-$CaAl_4O_7$-CaO-MgO
J. Am. Ceram. Soc. 82 (1999) 2193-2203
125 A.H. De Aza, J.E. Iglesias, P.Pena et. al.
Ternary System Al_2O_3-MgO-CaO: Part II, Phase Relationships in the Subsystem Al_2O_3-$MgAl_2O_4$-$CaAl_4O_7$
J. Am. Ceram. Soc. 83 (2000) 919-927
126 J. M. Florence, F.W. Glaze, M.H. Black
Infrared transmittance of some Calcium Aluminate and Germanate glasses
J. Res. Natl. Bur. of Standards55 (1955) 231-237
127 L. David Pye
Aluminate glasses –A review
SPIE (Infrared optical Materials IV) 929 (1988) 149-156
128 R.J. Charles, P.J. Jorgensen
Ceramic-Metal bonding composition and composite article manufacture
US patent 3545639 (1970)
129 E.V. Uhlmann, Weinberg, Kreidl et al.
Glass-forming ability in calcium aluminate-based systems
J. Am. Ceram Soc. 76(1993) 449-453
130 J. E. Shelby
Formation and properties of calcium aluminosilicate glasses
J. Am. Ceram Soc. 68(1985) 155-158
131 J. E. Shelby, C. M. Shaw, M. S. Spess
Calcium fluoraluminate glasses
J. Appl. Phys. 66 (1989) 1149-1154
132 ACErs-NIST
Phase equilibria diagrams CD-Rom database version 3.1
American Ceramic Society (2000)
133 G. A. Rankin and H. E. Merwin
The ternary system CaO-Al_2O_3-MgO
J. Am. Ceram Soc. 38 (1916) 568-588

134 G. Urbain
Viscosités de liquides du système $CaO-Al_2O_3$
Rev. int. Hautes Tempêr Réfract. Fr. 20(1983)135-139
135 Bruker AXS
PDFMaint-Powder diffraction files database 12,0,0,0 1995-2006, Bruker (1995)
136 R.W. Nurse, J.H. Welch and A.J. Majumdar
The $CaO-Al_2O_3$ system in a Moisture-free atmosphere
Trans. Brit. Ceram. Soc. 64 (1965) 409-418
137 R.W. Nurse, J.H. Welch and A.J. Majumdar
The $12CaO \cdot 7Al_2O_3$ Phase in the $CaO-Al_2O_3$ system
Trans. Brit. Ceram. Soc. 64 (1965) 323-332
138 S. Tsunekawa, T. Kamiyama, K. Sasaki et al.
X-ray pattern of $La(NbO_4)$ (PDF-File 81-1973) [134]
ACACEQ 49 (1993) 595
139 T.A. Vanderah, W. Febo, J.Y. Chan et al.
Minor Phase equilibria and dielectric behaviour in the $CaO:Al_2O_3:Nb_2O_5$ system
J. of. Solid State Chemistry 155 (2000) 78-85
140 N. Ishisawa, F. Marumo, S. Iwai et al.
Compounds with Perovskite-Type Slabs. III. The Structure of a Monoclinic Modification of $CaNb_2O_7$
Acta Crystallographica B36 (1980) 763-766
141 J.T. Lewandowski, I.J. Pickering, A. Jacobson
Hydrothermal Synthesis of Calcium-Niobium and Tantalum Oxides with the Pyrochlore Structure
Material Research Bulletin 27 (1992) 981-988
142 I. Levin, A. Bendersky, J.P. Cline et al.
Octahedral Tilting and Cation Ordering in Perovskite-Like $Ca_4Nb_2O_9=3 \cdot Ca(Ca_{1/3}Nb_{1/3})O_3$ Polymorphs
J. of Solid State Chemistry 150 (1999) 43-61
143 A. Vincent, S.B. Savignat, F. Gervais
Elaboration and ionic conduction of apatite-type lanthanum silicates doped with Ba, $La_{10-x} \cdot Ba_x(SiO_4)_6O_{3-x/2}$ with x=0.25-2
J. of Eur. Ceram. Soc. 27 (2007) 1187-1192
144 Bruker AXS TOPAS V2.1: General Profile and Structure Analysis Software for Diffraction Data Bruker AXS, Karlsruhe, Germany (2003)
145 H. Takeda, M. Ohgaki, T. Kizuki et al.
Formation mechanism and synthesis of apatite-type structure $Ba_{2+x}La_{8-x}(SiO_4)_6O_{2-\delta}$
J. Am. Ceram Soc. 83 (2000) 2884-2886

146 M.E. Huntelaar, E.H.P Cordfunke
The ternary system $BaSiO_3$-$SrSiO_3$-SiO_2
J. of Nuclear Materials 201 (1993) 250-253
147 L.Li, Z. Tang, W. Sun, P. Wang
Phase Diagram Prediction of the Al_2O_3-SiO_2-La_2O_3 System
J. of Material Science Technology 15 (1999) 439-443
148 A. Auriol, G. Hauser, J.G. Wurm
System BaO-La_2O_3
Battelle Ohio 1961 (See [131] Fig. 00209)
149 J.S. Reed
Ceramics Processing -second edition
John Wiley & Sons NY (1995)
150 S. Faaland
Heterogeneous ceramic interfaces in solid oxide fuel cells and dense oxygen permeable membranes.
PhD-Thesis Department of Chemistry NTNU, Trondheim Norway (2000)
151 T. Mokkelbost
Synthesis and Characterization of CeO_2-and $LaNbO_4$- based ionic conductors.
PhD-thesis Department of Materials Science and Engineering, NTNU (2006)
152 S.T. Reis, R.K. Bow
Resilient sealing materials for solid oxide fuel cells
Final Technical report, DOE: DE-FG26-04NT42175, 2007
153 W.Z. Zhu, S.C. Deevi
Development of interconnect materials for solid oxide fuel cells Center for Materials Chemistry – University of Houston USA A348 (2003) 227-243
154 J.E. Hammer, S.J. Laney, R.W. Jackson et al.
The oxidation of Ferritic Stainless Steel in Simulated Solid-Oxide Fuel-Cell Atmospheres
Energy Research 67 (2007) 1-38

14 Appendix 1

14.1 Thermal expansion of $Ca_{0.9}Fe_{0.1}TiO_3$

Thermal expansion of dense $CaTiO_3$ sintered at 1350 °C for 2 h was measured in the dilatometer. The sample was heated 3 times up to 1300 °C with a heating rate of 2 °C /min. The results after the third cycle are shown in Figure A1.1. Figure A1.2 shows the thermal expansion and TEC during heating and cooling calculated from least squares linear regression polynomials of 3rd degree of the thermal expansion curves. The polynomial coefficients are shown in Table A1.1 and the calculated data in Table A1.2.

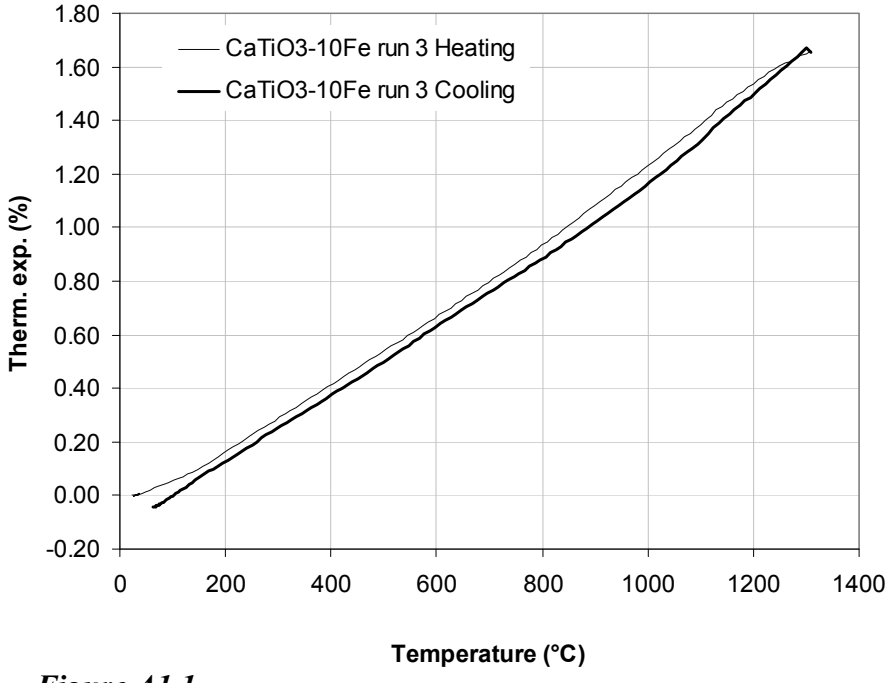

Figure A1.1
Thermal expansion during heating and cooling of dense $Ca_{0.9}Fe_{0.1}TiO_3$ sintered 2 hours at 1350 °C

Table A1.1
Polynomial coefficients for calculation of thermal expansion curves during heating and cooling of $Ca_{0.9}Fe_{0.1}TiO_3$

Coeff	Heating	Cooling
A0	-3.13E-02	-1.34E-01
A1	9.13E-04	1.37E-03
A2	5.09E-07	-3.35E-07
A3	-1.57E-10	2.68E-10
R^2	0.99977	0.9999

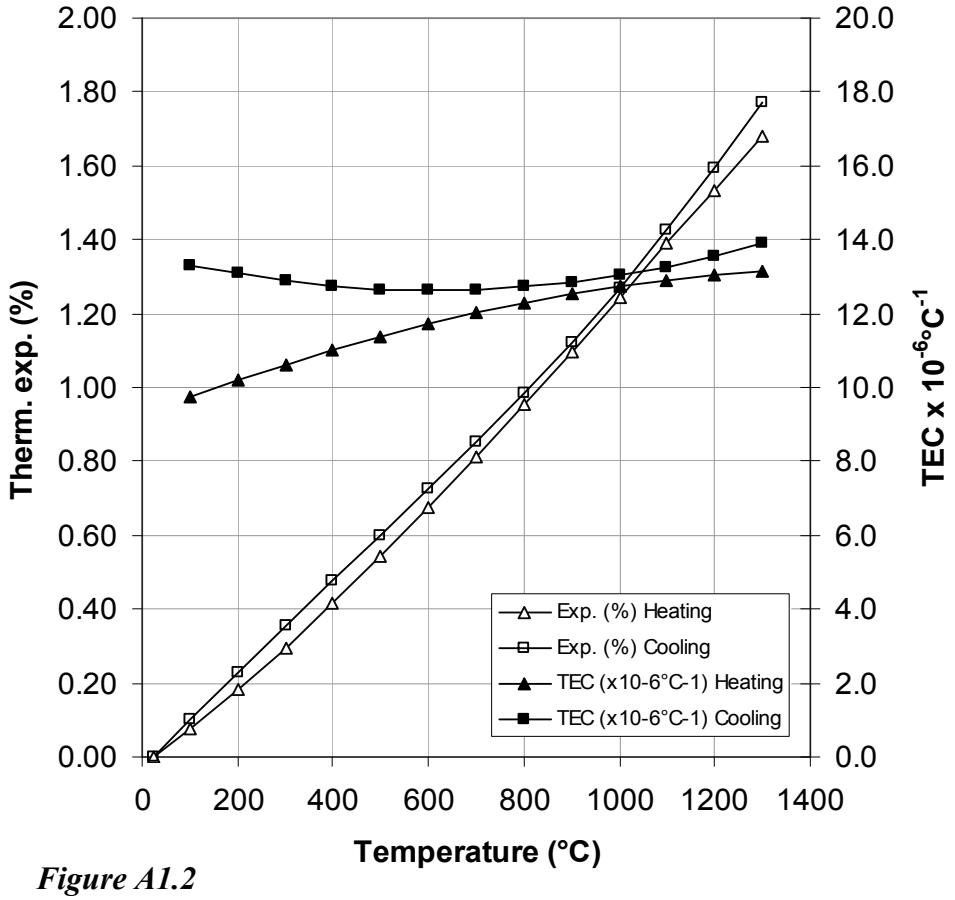

Figure A1.2
Calculated thermal expansion and TEC for $Ca_{0.9}Fe_{0.1}TiO_3$ from linear regression polynomials of 3rd order.

Table A1.2
Calculated thermal expansion and TEC for $Ca_{0.9}Fe_{0.1}TiO_3$ from linear regression polynomials of 3rd degree

Temp.	Thermal expansion (%)		TEC x10^{-6}°C^{-1}	
(°C)	Heating	Cooling	Heating	Cooling
25.0	0.00	0.00		
100.0	0.07	0.10	9.7	13.3
200.0	0.18	0.23	10.2	13.1
400.0	0.42	0.48	11.0	12.7
600.0	0.68	0.73	11.7	12.6
800.0	0.95	0.99	12.3	12.7
1000.0	1.24	1.27	12.7	13.0
1200.0	1.53	1.59	13.0	13.6
1400.0	1.82	1.96	13.2	14.3

15 Appendix 2

15.1 Flux test furnace

The equipment used for leakage test experiments consisted of the Flux-test furnace (Figure A2.1 and A2.2) the Micro GC and a gas-mixing system with several valves and mass-flow controllers (Figure A2.4). All gases passed a mixing column before entering the furnace. The flux test furnace (FTF) was a split-furnace that could be fully opened for easy access to the sample. A detailed drawing of the furnace is shown in Figure A2.3.

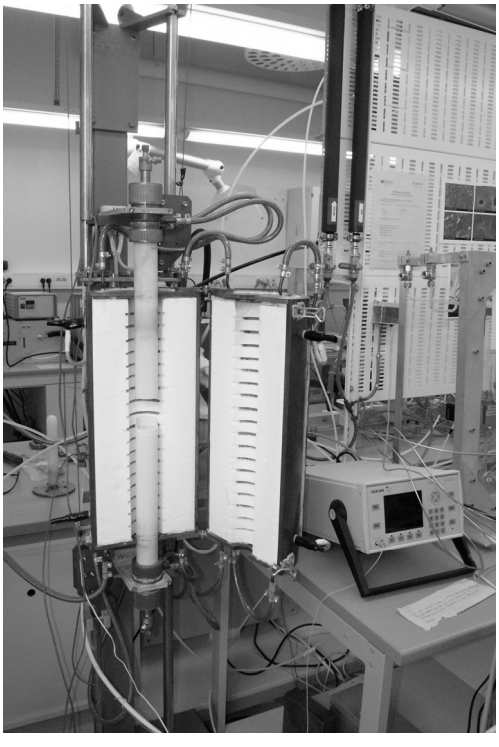

Figure A2.1
Flux furnace - opened showing the upper and lower tube assemblies with the support tubes (46x38 mm)

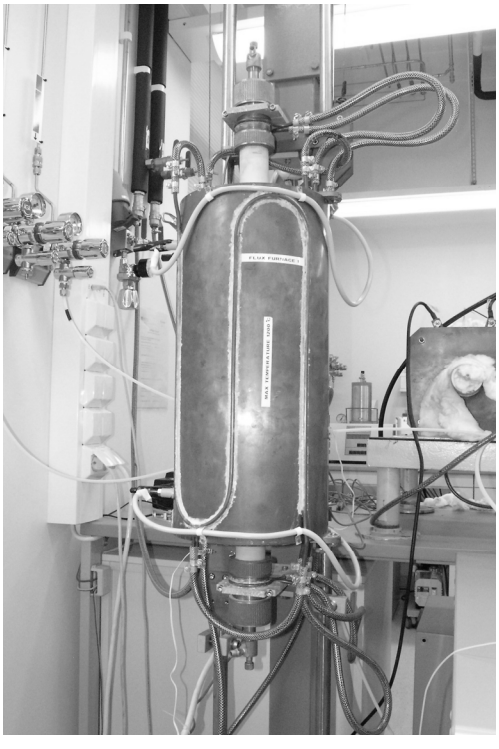

Figure A2.2
Flux furnace - closed

The furnace housing is fixed to the furnace stand. The top and bottom tube assemblies are fixed to slides (upper and lower slide) and are moveable in the vertical direction. The lower slide can be locked by a clamp ring. The upper slide is allowed to move freely. The tube assemblies are similar consisting of an outer support tube 46x38 mm in diameter, a sample support tube (Ø16x11 mm) that is in direct contact with the sample, and in the centre a gas supply tube (Ø 5-6 mm).

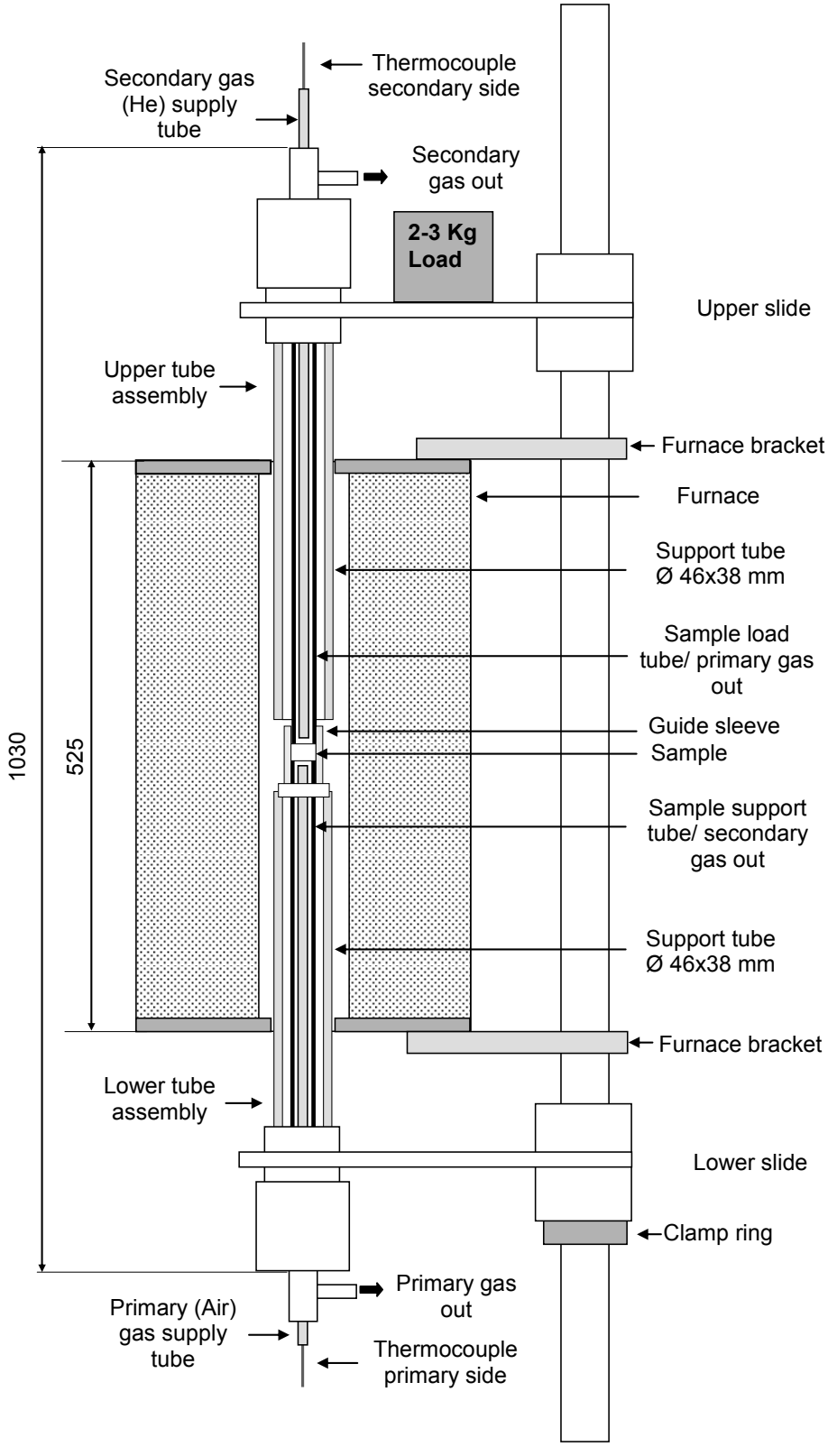

Figure A2.3
Simplified drawing of the Flux Test Furnace, showing the different tubes for gas supply, sample support and sample lining.

Inside the gas supply tubes, thermocouples (type S) were placed to measure the temperature close to the surfaces of the sample. The tubes in direct contact with the sample (sample support tube and sample load tube) were sealed by means of gold rings. The gold rings were held in place by a guide sleeve of alumina as illustrated in Figure 8.3. These tubes also serve as gas outlet tubes. The sweep gases (in the present case air at the primary side and He 99.999 at the secondary side) were lead through the central gas supply tube, which has the outlet 1-2 mm from the sample surface. The He gas at the secondary side was mixed with the gas permeating the membrane and gas from direct leakage. This gas mixture was lead through the upper sample load tube and to the Micro GC. A load is put on the upper tube assembly in order to obtain press on the gold rings. Typical load was 2-3 kg.

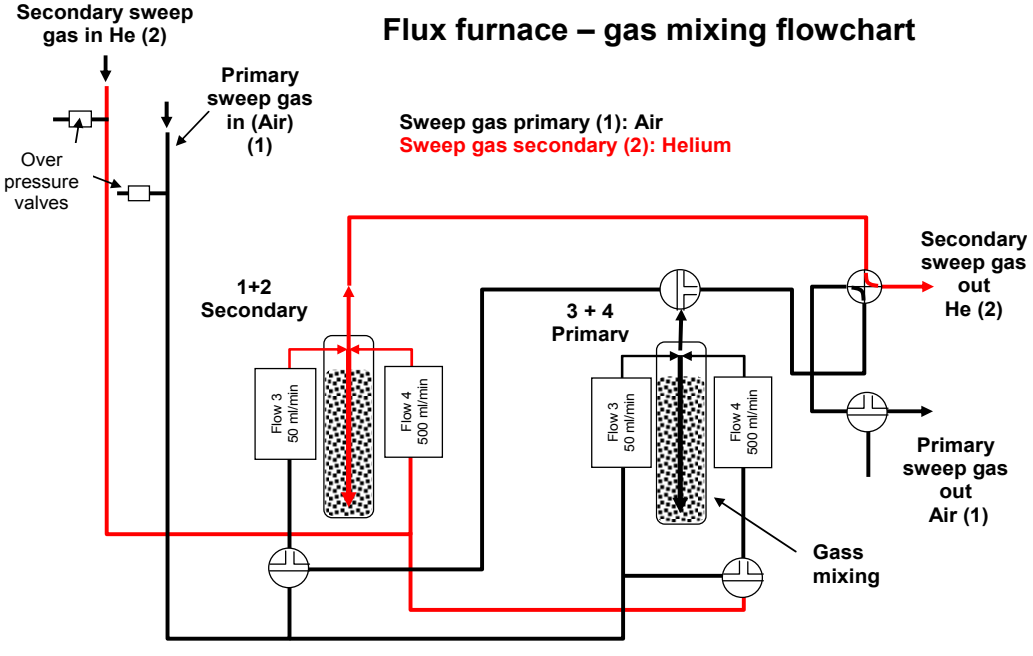

Figure A2.4 *Gas mixing system with gas mixing and Mass-Flow controllers*

The overall length of the furnace included tube assemblies was 1030 mm. The length of the furnace was 525 mm and the outer diameter was 230 mm. Maximum furnace temperature was 1200 °C. Typical temperature difference across the sample was < 1 °C. The temperature control was performed by using a Eurotherm 903P - controller.